Carnegie Mellon University

CARNEGIE INSTITUTE OF TECHNOLOGY

THESIS

SUBMITTED IN PARTIAL FULFILLMENT OF THE REQUIREMENTS

FOR THE DEGREE OF Doctor of Philosophy

TITLE Computational Multiscale Methods for Defects: 1. Line Defects in

Liquid Crystals; 2. Electron Scattering in Defected Crystals

PRESENTED BY Hossein Pourmatin

ACCEPTED BY THE DEPARTMENTS OF

Civil and Environmental Engineering

Kaushik Dayal   December 18, 2014
ADVISOR, MAJOR PROFESSOR   DATE

David A. Dzombak   December 19, 2014
DEPARTMENT HEAD   DATE

APPROVED BY THE COLLEGE COUNCIL

Vijayakumar Bhagavatula   January 12, 2015
DEAN   DATE

Computational Multiscale Methods for Defects: 1. Line Defects in Liquid Crystals; 2. Electron Scattering in Defected Crystals

Submitted in partial fulfillment of the requirements for

the degree of

Doctor of Philosophy

in

Civil and Environmental Engineering

Hossein Pourmatin

B.S., Civil Engineering, University of Tehran
M.S., Structural Engineering, Sharif Institute of Technology

Carnegie Mellon University
Pittsburgh, PA

December, 2014

Acknowledgements

I would like to express my sincere thanks and appreciation to all the people who have guided and inspired me through my PhD research at Carnegie Mellon University.

First and for most, I thank my advisor Dr. Kaushik Dayal for his constant support. If it was not for his help and dedication, I could not have conducted this research. I appreciate all his effort in investing his time and energy to answer my questions and sharing his wisdom, not only in my research but also in all of his fields of expertise. His patience in elaborating the details is truly exceptional.

Second, I want to express my thanks and gratitude to Professor Amit Acharya who co-advised me through my first two year of research on kinematics of liquid crystals. He is one of the most knowledgable faculty members that I have had the pleasure of their acquaintance. His attention to my work lead me through the research and his enthusiasm to the subject helped me to truly enjoy my work. The first part of this thesis (A fundamental improvement to Ericksen-Leslie kinematics) is mostly his genius work.

I would also like to thank the rest of my dissertation committee members for their time and guidance. Dr. Jacobo Bielak, gave me very valuable insight about non-reflecting boundary conditions at the beginning of my research on this subject. Dr. Michael Widom who was also my instructor for the Quantum Mechanics course dedicated his time on multiple occasions to help me though the concepts of tight-binding method for my research. Moreover, Dr. Alan Mcgaughey's course on Molecular Dynamics, was one of the most valuable and insightful courses that I had at Carnegie Mellon University. I deeply cherish all their help during these year.

Last but not least, I thank my friends and colleagues, Amin Aghaei, Jason Mar-

Abstract

In the first part of this thesis, we demonstrate theory and computations for finite-energy line defect solutions in an improvement of Ericksen-Leslie liquid crystal theory. Planar director fields are considered in two and three space dimensions, and we demonstrate straight as well as loop disclination solutions. The possibility of static balance of forces in the presence of a disclination and in the absence of flow and body forces is discussed. The work exploits an implicit conceptual connection between the Weingarten-Volterra characterization of possible jumps in certain potential fields and the Stokes-Helmholtz resolution of vector fields. The theoretical basis of our work is compared and contrasted with the theory of Volterra disclinations in elasticity. Physical reasoning precluding a gauge-invariant structure for the model is also presented.

In part II of the thesis, the time-harmonic Schrodinger equation with periodic potential is considered. We derive the asymptotic form of the scattering wave function in the periodic space and investigate the possibility of its application as a DtN non-reflecting boundary condition. Moreover, we study the perfectly matched layer method for this problem and show that it is a reliable method, which converges rapidly to the exact solution, as the thickness of the absorbing layer increases. Moreover, we use the tight-binding method to numerically solve the Schrodinger equation for Graphene sheets, symmetry-adapted Carbon nanotubes and DNA molecules to demonstrate their electronic behavior in the presence of local defects. The results for Y-junction Carbon nanotubes depict very interesting properties and confirms the predictions for their application as new transistors.

Table of Contents

List of Figures

Part

I

Line Defects in Liquid

1

Introduction

While liquid crystal theory, especially that of nematics, is by now a well-established branch of condensed matter physics [43], there is one aspect in which the classical theory may be considered deficient. Disclination line defects are an integral part of the physics of liquid crystals - however, there does not exist a classical theory, whether Oseen-Frank for statics or Ericksen-Leslie in dynamics (which naturally subsumes the static theory), that predicts bounded energy in a finite body containing a $\pm\frac{1}{2}$-strength disclination line. It is perhaps for this reason that it is commonplace amongst workers in liquid crystal theory to associate a defect only with a singularity, e.g. the 'escape' solution for a +1 strength line defect [22] is often not referred to as a defect solution.

Director fields with infinite energy are practically problematic from the point of view of finding solutions - e.g. in statics, energy cannot be minimized in a class of functions where all competing fields with defects have undefined (infinite) energies. Practical difficulties remain in dynamics, more so if the goal is to specify dynamics of defect lines. While for the purpose of static Oseen-Frank theory involving a few defects one overcomes such problems by excluding from analysis a core region of

2

small volume along the defect line where one assumes the theory does not hold and ascribing a finite energy to it from some unspecified-in-theory nonlinear effects, for situations where large numbers of defects may be involved, such an approach is untenable. To quote Ericksen [26] "I am interested in seeing the development of a mathematically sound theory of defects which might be at rest, or moving. ...serious difficulties are encountered with some observed kinds of disclinations (line defects). According to the aforementioned theories [Oseen-Frank, Ericksen-Leslie], these more violent singularities cause energy integrals, etc., to diverge. In dealing with rather specific situations, workers have patched up the theory by excluding a tube of small radius, assigning a finite "core energy" to it. I just do not believe that one can use such ideas as a basis for developing satisfactory mathematical theory, particularly for moving defects. Such phenomena are of interest for both nematic and cholesteric liquid crystals. In the latter, they are associated with the interesting "blue phases" ....."

In [5] a theory for the dynamics of non-singular line defects has been proposed as an extension of Ericksen-Leslie [47] theory. The model works with augmented kinematics involving the director field and an *incompatible* director distortion field as a replacement for the director gradient field. The main point of departure is that the director distortion is not *curl*-free, in general. The *curl* of the field has the kinematic meaning of an areal density of lines carrying a vectorial attribute and is referred to as the director incompatibility field. For the 1-constant Oseen-Frank energy approximation, it was shown in [5] that the developed formalism can indeed predict the outside-core, energy density distribution of Frank's *planar* director distributions for line defects with strength given by all integer multiples of $\frac{1}{2}$. Moreover, all such distributions have finite energy in the whole body (including core). The core is represented by precisely the region where the director incompatibility field is non-vanishing. However, it was not shown in that work how to extract a physically

realistic continuous director field resembling Frank's planar defect fields on the whole body, and neither was it shown as to what form the director distortion tensor might take within the theory to represent planar distortion fields of disclination line defects. In this paper we achieve that goal.

The modeling of bounded energy line defects in statics started with the pioneering work of [22] within classical Oseen-Frank theory. The same question served as motivation for the development of the variable degree of orientation extension of classical Ericksen Leslie theory in [26]. Within the De-Gennes Q tensor formalism it has been pursued in [64], [44], [10], [52]. In the dynamic case, representative studies are those of [35] and [70] within the Q-tensor approach and [49, 50] within the Ericksen-Leslie approach. In [49, 50] non-singular line-defect solutions appear due to relaxation of the unit-magnitude constraint on the director field. In contrast, in our work the demonstrated finite energy defect solutions satisfy the strict unit-vector constraint on the director field.

The defect solutions we develop here are finite energy analogs of classically accepted 'energy-minimizing' (infinite total energy) singular solutions of Oseen-Zocher-Frank theory. As is customary in the liquid crystal literature when discussing statics of defects solutions, we (almost) ignore balance of forces. What we are able to show in this regard (Section 4) is that static balance of linear momentum is satisfied outside the core(s) of disclination(s) in the absence of a body force within our model (assuming an incompressible fluid). Moreover, when there is a single disclination in the body, the natural boundary conditions for static force and moment balance representing no applied forces and couples on the boundary imply that the resultant force on any surface enveloping the disclination core vanishes. Within the core, we discuss possibilities afforded by the [5] theory in satisfying balance of linear momentum without external body forces or flow.

We consider this work to be primarily a characterization of the kinematic aug-

mentation of the Ericksen-Leslie theory achieved by the [5] model, since results are not presented regarding the connection of the presented solutions to (quasi)equilibria (cf. [18]) of the latter.

This paper is organized as follows: in Section 1.1 we provide notation. Section 2 describes the analytical basis of our work; Section 3 describes the finite-element based numerical scheme employed to compute non-singular defect solutions and the results. In Section 4 we discuss static balance of forces for the developed solutions, and Section 5 ends with some concluding remarks. Two appendices provide explicit solutions that are necessary for discussing our results.

1.1 Notation

A "·" represents the inner product of two vectors, while ":" represents the trace inner product of two second-order tensors, $\boldsymbol{A} : \boldsymbol{B} = A_{ij}B_{ij}$.

In rectangular Cartesian coordinates and corresponding bases and components, for a vector field $\boldsymbol{A}$ and a scalar field θ we write:

$$div\,\boldsymbol{A} = A_{i,i}$$

$$(curl\,\boldsymbol{A})_i = e_{ijk}A_{k,j}$$

$$(grad\,\theta)_i = \theta_{,i}$$

For a second-order tensor field $\boldsymbol{A}$, we define

$$(\mathrm{curl}\,\boldsymbol{A})_{im} = e_{mjk}A_{ik,j}.$$

The following list describes some of the mathematical symbols we use in this paper:

$\boldsymbol{n}$: director

$\boldsymbol{E}$: director distortion tensor

$\boldsymbol{E}^{\theta}$: director distortion vector

$\boldsymbol{\beta}$: director incompatibility tensor

$\boldsymbol{\beta}^{\theta}$: director incompatibility vector

K : defect strength

$\boldsymbol{\nu}$: normal vector

$\boldsymbol{T}$: Cauchy stress tensor

$\boldsymbol{\Lambda}$: couple stress tensor

ψ : free energy per unit mass

p : pressure

θ : angle of the director field

$\boldsymbol{\lambda}$: layer field

$\boldsymbol{\lambda}_{\perp}$: incompatible part of $\boldsymbol{\lambda}$

$grad\, z$: compatible part of $\boldsymbol{\lambda}$

Theory

We consider the static (i.e. director and positional inertia-less) governing equations of the framework introduced in [5] and demonstrate that there exists finite-energy states in the model that are solutions corresponding to line defects with planar director distributions within the Oseen-Frank constitutive assumption.

2.1 Governing equations

Static Balance of Angular Momentum is given by the statement

$$\Lambda_{ij,j} - e_{ijk}T_{jk} = 0.$$

Ericksen's identity for the theory (i.e. a necessary condition for frame-indifference of the energy function) is the statement

$$e_{ijk}\left(\frac{\partial \psi}{\partial n_i}n_j + \frac{\partial \psi}{\partial E_{ir}}E_{jr} - E_{ri}\frac{\partial \psi}{\partial E_{rj}}\right) = 0.$$

Static Balance of Linear Momentum is the statement

$$T_{ij,j} = 0.$$

For a free-energy density of the form $\psi\left(\boldsymbol{n}, \boldsymbol{E}\right)$, the constitutive statements for the stress and couple stress tensors for the theory [5] read as

$$\Lambda_{ij} = e_{irs}n_r\frac{\partial\psi}{\partial E_{sj}}$$

$$T_{ij} = -p\delta_{ij} - E_{ri}\frac{\partial\psi}{\partial E_{rj}},$$

where p is the pressure arising from the constraint of incomressibility. Using these statements along with the Ericksen identity in angular momentum balance with some manipulations yields the fundamental governing partial differential equation of our work:

$$e_{irs}\left[n_s\frac{\partial\psi}{\partial n_r} - (E_{rj} - n_{r,j})\frac{\partial\psi}{\partial E_{sj}} + n_r\left(\frac{\partial\psi}{\partial E_{sj}}\right)_{,j}\right] = 0. \tag{2.1}$$

Note the interesting fact that when $E_{rj} = n_{r,j}$, i.e. there is no director incompatibility and hence no defects, we have the classical statement of angular momentum balance in statics [65]. Inasmuch, this term in our theory may be interpreted as giving one explicit form to Ericksen's "internal body moments" [26], $\boldsymbol{g}^I$, arising from the presence of defects in the body.

We record the statement of balance of linear momentum,

$$- p_{,i} - \left(E_{ri}\frac{\partial\psi}{\partial E_{rj}}\right)_{,j} = 0, \tag{2.2}$$

to be used later in Section 4.

For the sake of this paper, we consider an *ansatz* consisting of director distributions parametrizable by a single angle field θ on the body and director distortion fields of the form

$$\boldsymbol{E} := \frac{\partial\boldsymbol{n}}{\partial\theta}\otimes\boldsymbol{E}^\theta, \tag{2.3}$$

8

where $\boldsymbol{E}^\theta$ *is a vector field* with possibly non-vanishing *curl*. When there are no line defects, we require $\boldsymbol{E}^\theta = grad\,\theta$ so that $\boldsymbol{E} = grad\,\boldsymbol{n}$.

Let the *core* region for a given $\boldsymbol{E}^\theta$ field on the body be the set of points on which

$$\boldsymbol{\beta}^\theta := curl\,\boldsymbol{E}^\theta \neq \boldsymbol{0}$$

and

$$\boldsymbol{\beta} := curl(\boldsymbol{E} - grad\,\boldsymbol{n}) \neq \boldsymbol{0}.$$

We refer to an $\boldsymbol{E}^\theta$ field as containing an isolated line defect if its $\boldsymbol{\beta}^\theta$ field is non zero only in a cylindrical region that forms a closed loop or extends from one boundary of the body to another.

The goal now is to construct pairs of $(\boldsymbol{E}, \boldsymbol{n})$ fields

1. that satisfy (2.1);

2. that produce Frank's isolated line defect-like energy density fields outside the core region, while producing bounded energy in finite bodies (including the core region), when no moments are applied on the boundary of the body;

3. that produce Frank's wedge disclination-like director distributions except the core and possibly another region of 'small', but non-zero, volume in the body;

4. for which the line integral of $\boldsymbol{E}^\theta$, along any closed contour surrounding the core of an isolated line defect of strength K, evaluates to $2\pi K$.

2.2 Construction of bounded energy distortion and director solutions

We work with a rectangular Cartesian coordinate system with unit vectors $\boldsymbol{e}_i, i = 1, 2, 3$. θ represents the angle of the director measured counter-clockwise from the x_1-axis in the $x_1 - x_2$ plane (looking down the x_3-axis). Thus

$$\boldsymbol{n} = \cos\theta\boldsymbol{e}_1 + \sin\theta\boldsymbol{e}_2. \tag{2.4}$$

9

For the sake of illustrating the essentials of our approach, we work with the 1-constant Oseen-Frank energy density approximation

$$\psi\left(\boldsymbol{n}, \boldsymbol{E}\right) = \frac{1}{2}\kappa\boldsymbol{E} : \boldsymbol{E} = \frac{1}{2}\kappa E_{ij}E_{ij} = \frac{1}{2}\kappa E_i^\theta E_i^\theta \tag{2.5}$$

and

$$\frac{\partial\psi}{\partial E_{sj}} = \kappa E_{sj} = \kappa\frac{\partial n_s}{\partial\theta}E_j^\theta. \tag{2.6}$$

Noting

$$E_{rj} - n_{r,j} = \frac{\partial n_r}{\partial\theta}\left(E_j^\theta - \theta_{,j}\right)$$

and (2.5)-(2.6), (2.1) reduces to

$$e_{irs}n_r\kappa\left[\frac{\partial n_s}{\partial\theta}E_j^\theta\right]_{,j} = 0.$$

Considering (2.4) and realizing that $e_{irs}n_r\frac{\partial^2 n_s}{\partial\theta^2}\theta_{,j} = 0$, static angular momentum balance reduces to

$$e_{irs}n_r\frac{\partial n_s}{\partial\theta}E_{j,j}^\theta = 0$$

which is satisfied if and only if

$$div\,\boldsymbol{E}^\theta = 0. \tag{2.7}$$

To fulfill the fourth requirement on the field $\boldsymbol{E}^\theta$, let us now consider a distribution of $\boldsymbol{\beta}^\theta := curl\boldsymbol{E}^\theta$ in a right-cylinder parallel to x_3 such that

$$\int_A \boldsymbol{\beta}^\theta \cdot \boldsymbol{e}_3 \; dx_1 dx_2 = 2\pi K, \tag{2.8}$$

where A is the set of points representing the cross section of the core cylinder. Thus, in addition to (2.7), we require

$$curl\boldsymbol{E}^\theta = \boldsymbol{\beta}^\theta. \tag{2.9}$$

10

Finally, to impose the fact that we seek non-trivial solutions for an unloaded body, we impose vanishing moments on the boundary of the body which, under the current ansatz is satisfied if

$$\boldsymbol{E}^\theta \cdot \boldsymbol{\nu} = 0 \tag{2.10}$$

on the boundary of the body with normal field $\boldsymbol{\nu}$.

It is straightforward to see that, for a specified field $\boldsymbol{\beta}^\theta$ on a simply-connected domain, (2.7)-(2.9)-(2.10) has a unique solution. In [5], these equations are solved explicitly for a radially symmetric $\boldsymbol{\beta}^\theta$ distribution (see Appendix B), and the outside-core result shown to be exactly the same as the gradient of the Frank angle field for straight wedge disclinations. In the general case, (i.e. not necessarily radially-symmetric $\boldsymbol{\beta}^\theta$ field, but still localized in core cylinder distributions) we would now like to extract the outside-core result into a gradient of a *continuous everywhere* scalar angle field θ which will serve to define the $\boldsymbol{n}$ field of the pair $(\boldsymbol{E}, \boldsymbol{n})$ describing an isolated defect. Of course, in the process we would like to have $\boldsymbol{E}^\theta$ still be the solution to (2.7)-(2.9)-(2.10) and $\boldsymbol{E}^\theta = grad\,\theta$ when $\boldsymbol{\beta}^\theta = \boldsymbol{0}$.

To perform this extraction, suppose for a moment it is possible to construct a square-integrable vector field $\boldsymbol{\lambda}$ such that

$$curl\,\boldsymbol{\lambda} = -\boldsymbol{\beta}^\theta \tag{2.11}$$

on the body, where the $\boldsymbol{\beta}^\theta$ field is identical to the one occurring in (2.9). Then a Stokes-Helmholtz resolution of the field $\boldsymbol{\lambda}$ can be written as

$$\boldsymbol{\lambda} = \boldsymbol{\lambda}_\perp + grad\,z$$

with

$$curl\,\boldsymbol{\lambda}_\perp = curl\,\boldsymbol{\lambda} = -\boldsymbol{\beta}^\theta \tag{2.12}$$

$$div\,\boldsymbol{\lambda}_\perp = 0$$

11
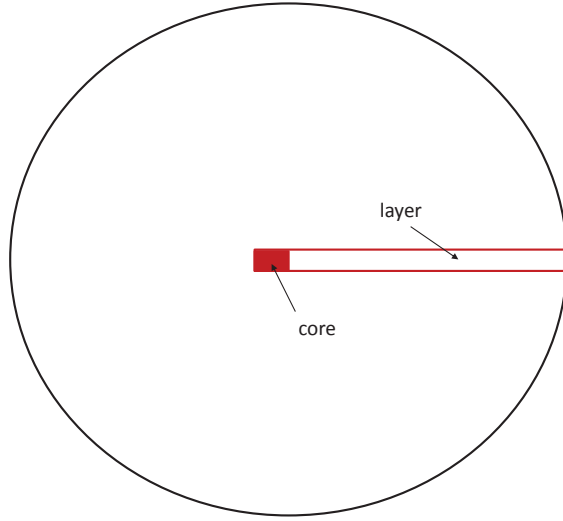
Figure 2.1: Schematic of cross-section of a 3-d body showing layer and core geometry

and

$$\boldsymbol{\lambda}_{\perp} \cdot \boldsymbol{\nu} = 0 \quad \text{on boundary of body,}$$

and because of the uniqueness of solutions to (2.7)-(2.9)-(2.10), $\boldsymbol{E}^{\theta} = -\boldsymbol{\lambda}_{\perp}$.

Suppose further now that the field $\boldsymbol{\lambda}$ *is non-vanishing only on a layer-like region of non-zero volume*[1] that may be visualized as a terminating fattened 2-d surface which, moreover, contains as a proper subset the core cylinder on which $\boldsymbol{\beta}^{\theta}$ has support (Figure 2.1).

Then, as an immediate consequence we have that

$$-grad\, z = \boldsymbol{\lambda}_{\perp} = -\boldsymbol{E}^{\theta} \quad \text{outside the layer.}$$

Thus, if we were to now declare the potential z as the required angle-field θ, *we would have completed the needed extraction.*

---

[1] Cf. [23]; DeWit considers a distributional layer field in the context of disclinations in solids related to defects in positional order.

In practice (Section 3), we implement the above idea by defining

$$\boldsymbol{E}^\theta := grad\,\theta - \boldsymbol{\lambda} \tag{2.13}$$

and requiring this combination to satisfy (2.7)-(2.9)-(2.10) so that

$$grad\,\theta - \boldsymbol{\lambda} = -\boldsymbol{\lambda}_\perp \tag{2.14}$$

is enforced by uniqueness implying $grad\,\theta = grad\,z$. When accompanied by the requirement that $\boldsymbol{\lambda} = \boldsymbol{0}$ if $\boldsymbol{\beta}^\theta = \boldsymbol{0}$, the strategy ensures that $\boldsymbol{E} = grad\,\theta$ in the abence of defects in the body. We note the important fact that the Stokes-Helmholtz decomposition of an L_2 vector field implies that $grad\,z$ is square-integrable and therefore $grad\,\theta$ cannot have a non-square-integrable singularity in the body. *The set of Definitions (2.3) and (2.13) constitutes a primary result of this paper.*

So, the only question that remains is whether such a layer-field $\boldsymbol{\lambda}$ satisfying (2.11) can in fact be constructed. As we show Section 3, it suffices to consider the layer region as in Figure 2.1, prescribe an appropriate constant vector field (representative of an interpolation of the required jump in the value of θ, i.e. $2\pi K$, in the direction transverse to the layer) for the values of $\boldsymbol{\lambda}$ outside the core in it, and tapering this interpolated jump to zero over the width of the core. Outside the layer, $\boldsymbol{\lambda}$ is assigned to vanish. Since $\boldsymbol{\lambda}$ represents a transverse 'gradient' in the layer whereas in the core this transverse variation has a gradient in an in-plane direction, it cannot have vanishing *curl* in the core. Thus we represent a non-singular, but localized, core of a line defect.

We now ask the question of the region where $\boldsymbol{\beta}$ is non-vanishing corresponding to an isolated wedge disclination. The existence of a differentiable extracted θ field (which can be arranged as can be seen from the construction in Appendix A) implies that the $\boldsymbol{\beta}$ field corresponding to an isolated defect would be non-vanishing at most

13

in the layer, since $grad\,\theta = \boldsymbol{E}^\theta$ outside the layer and

$$E_{rj,k} = \frac{\partial^2 n_r}{\partial \theta^2}\theta_{,k}E_j^\theta + \frac{\partial n_r}{\partial \theta}E_{j,k}^\theta. \tag{2.15}$$

Our use of a layer field may be interpreted as a regularized analog of the possible terminating discontinuity in the displacement field over a 'cut' surface in the Weingarten-Volterra (WV) process of elastic dislocation theory, adapted to a much simpler situation than elasticity; thus, the construction shows direct links between the Stokes-Helmholtz (SH) resolution of a vector field (in this instance, the layer field) and the Weingarten-Volterra process. In particular, how the '*curl*' part of SH encodes, through a smooth field, topological content that can only be represented by a nasty singularity in the gradient of a discontinuous potential field in the WV process. And, how the 'gradient' part of SH of an appropriately designed vector field (the layer field) can represent most of the characteristics of the discontinuous potential field of the WV process away from the discontinuity.

2.3 Does topological defect density determine the director distribution?

The construction above lays bare an interesting fact. Note that $\boldsymbol{E}^\theta$ is uniquely determined by the defect density field $\boldsymbol{\beta}^\theta$ (and balance of moments) but $grad\,\theta$, and hence the predicted director distribution, is defined by the compatible part $grad\,z$ of $\boldsymbol{\lambda}$. An alternative way of seeing this is to substitute

$$\boldsymbol{E}^\theta = grad\,\theta - \boldsymbol{\lambda}_\perp - grad\,z$$

into (2.7)-(2.9)-(2.10) (this idea is not restricted to the 1-constant energy in any way). Thus, while the energy density distribution, and therefore the couple stress, can be correctly predicted purely from the knowledge of the defect distribution (in this static setting), uniquely predicting the director distribution requires additional

14

physical input in the presence of defects. In particular, the layer-like $\boldsymbol{\lambda}$ field consistent with a specified isolated defect density field orients the nonsingular director distribution of the defect, as is shown in Section 3. To draw an association with classical potential theory, specifying the surface of discontinuity of a scalar potential field whose gradient is required to match, except on the discontinuity surface, a prescribed, smooth, irrotational vector field on a doubly-connected region containing a toroidal or through-hole eliminates the vast non-uniqueness associated with such definition of a potential otherwise. The argument also reveals why the classical theory with only the director field as a degree of freedom is necessarily limited in the context of modeling defects.

It is also interesting to observe that this situation is entirely analogous to the extension that was required for making a prediction of permanent deformation [1] in the elastic theory of continuously distributed dislocations [45], [69]. Comparing and contrasting with prevalent notions in gauge theories, θ and the total displacement field of plasticity theory are not inconsequential fields to be gauge-transformed away *even* when they have no energetic cost through the Lagrangian in the presence of gauge fields ($\boldsymbol{\lambda}$, in this context), but direct physical observables that participate in understanding energy dissipation, shape changes, and optical response of the body. Hence, their evolution requires additional physical specification beyond the topological defect density field.

2.4   Relationship with disclinations in elasticity theory

Our construction of the $\boldsymbol{\lambda}$ field draws direct motivation from a standard question of potential theory related to understanding the allowable jumps of a scalar potential across a 2-d surface in a multiply-connected domain described by a through-hole in a 3-d body. For example, consider Figure 2.1 with the layer shrunk to zero thickness and also the consequent core to a line of puncture through the plane of the paper;

the core-line represents the through-hole. The 2-d surface is such that a cut along it renders simply-connected the body with the hole. Additionally, the gradient of the potential field is required to match a prescribed irrotational vector field on the simply-connected domain obtained through the cut.

We note here that the question above is much simpler in its details than the question posed by Weingarten and Volterra related to understanding the jumps of a displacement (vector) field, when its symmetrized gradient is required to match a prescribed *symmetric* tensor field which satisfies the St.-Venant compatibility condition of linear elasticity theory in the simply-connected domain resulting from a planar cut of the multiply-connected domain with the hole. Indeed, in this latter case, a key construction is a skew-symmetric tensor field (infinitesimal rotation) from the prescribed symmetric tensor field, whose jump across the cut-surfaces (that serve as parts of the boundary of the simply-connected domain) relates directly to the disclinations of linear elasticity theory. It should be clear, then, that in the liquid crystal theory context, even if one chose to discuss the issue of allowable jumps in the director field context rather than the angle parametrization field, there is no natural way a relevant symmetric tensor field arises from the director gradient whose unique[2] infinitesimal rotation field in a simply-connected domain may then be used to define the notion of an isolated singular disclination in liquid crystal theory. Given that the Oseen-Frank and Ericksen-Leslie theories are geometrically exact, the situation is not very different if a link is attempted between liquid crystal disclinations and the singular defects that characterize the jumps in finite rotation associated with an elastic strain field that satisfies the finite strain compatibility conditions in a multiply-connected domain. Again, the issue crucially hinges on the question being posed in terms of the basic tensor field being a positive-definite symmetric second

---

[2] Up to a spatially uniform skew-symmetric tensor field.

order tensor field (the Right-Cauchy-Green tensor field) and there does not seem to be any natural way in which the director gradient may be considered to generate such a field. Such an observation is consistent with that made in [42] (Sec. I.E.1, p. 67): "This explains the interest in reconsidering the continuous theory of defects, although new concepts have to emerge. The case of mesomorphic phases requires an extension of the theory of continuous defects for solids to situations where there is locally only one physical direction (the director), i.e. no local trihedron of directions, as in the uniaxial nematic N, the $\mathrm{Sm}A$, and the columnar D cases." We believe that our work provides the natural extension of the theory of continuous defects in solids to the mesomorphic phases named above.

As a further example of such differences, we note, as mentioned in [42] Sec. IIA (p. 69, Remark), that the Volterra process is properly defined only for magnitude of rotation angles less than π. However, as far as wedge disclinations in liquid crystals are concerned the $+\frac{1}{2}$ and $+\frac{3}{2}$ strength defects are entirely different entities - as shown in Section 3, our theory is able to predict such differences.

3

Computation of bounded energy distortion and director solutions

We demonstrate and evaluate the ideas presented in Section 2.2 through explicit constructions for different kinds of defects. First, we present results for straight wedge and twist disclinations and compare our results with Frank's planar model [30]. Then we take the next step forward and simulate twist disinclination loops.

3.1 Straight disclination

We refer to disclinations with core cylinder along a straight line, as opposed to a general curve or a closed loop, as *straight disclinations*. A straight wedge disclination is one for which the defect line is along the axis of rotation of the director field. In the case of a twist disclination, the line is perpendicular to the axis of rotation.

3.1.1 Wedge disclination

Although it is uncommon find an isolated wedge disclination in nature due to its considerable energy cost, it is nevertheless a canonical problem for theoretical tools and we study such a 2-dimensional line defect [43].

Consider θ as a function of the coordinates x_1 and x_2, so that the director field would be planar. According to (2.8), (2.11) and Stokes' theorem

$$\int \beta_3^\theta dA = -\int \text{curl}\,\boldsymbol{\lambda} \cdot \boldsymbol{e}_3 dA = -\oint \boldsymbol{\lambda} \cdot dr = 2\pi K. \tag{3.1}$$

This criterion indicates that the line integral of the vector field $\boldsymbol{\lambda}$ over any closed curve bounding the core is non-vanishing. Inspired by the Weingarten-Volterra process in elastic dislocation theory and adapting it to the simpler situation at hand as indicated in Sections 2.2-2.4, we define $\boldsymbol{\lambda}$ as a vector field with support on a thin layer that originates from the defect core and extends all the way to the boundary:

$$\boldsymbol{\lambda} := -\frac{2\pi K}{2r_1}\boldsymbol{e}_1 \quad \text{for } \begin{cases} x_2 > 0 \\ |x_1| < r_1. \end{cases} \tag{3.2}$$

Here, r_1 defines the spatial width of the layer. The derivative of $\boldsymbol{\lambda}$ with respect to x_2 is zero everywhere, except at the layer boundary at $x_2 = 0$. Consequently, $\boldsymbol{\beta}^\theta$ will be a singular wall-like distribution of finite extent supported on this layer boundary. However, for reasons indicated in Section 2.2, the total energy of the disclination so defined would still necessarily be finite.

In agreement with Figure 2.1, we now endow this singular wall with a finite width[1]. Thus, the following definition for the layer field is used:

$$\lambda_1 := \begin{cases} \frac{2\pi K}{2r_1} & x_2 > \frac{r_0}{2} \\ \frac{2\pi K}{2r_1}\frac{r_0+2x_2}{2r_0} & |x_2| \leq \frac{r_0}{2} \end{cases} \quad |x_1| < r_1. \tag{3.3}$$

Figure 3.1 shows the norm of $\boldsymbol{\lambda}$ and the resulting $\boldsymbol{\beta}^\theta$ field from it, where both fields have been normalized by K:

$$\tilde{\boldsymbol{\lambda}} = \frac{1}{K}\boldsymbol{\lambda} \qquad \tilde{\boldsymbol{\beta}}^\theta = \frac{1}{K}\boldsymbol{\beta}^\theta.$$

---

[1] Of course, ideally one would seek such a width as an outcome of the full dynamical model. As a first step, we show here that isolated disclinations of specified strength with finite-size cores can be solutions to balance of moments in our model.

(a) $|\tilde{\boldsymbol{\lambda}}|$ (b) $|\tilde{\boldsymbol{\beta}}^{\theta}|$
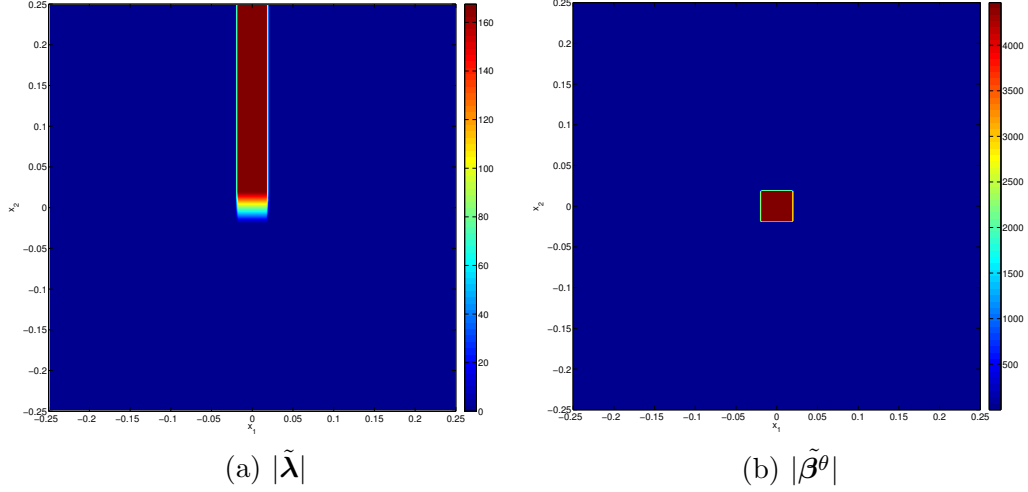
Figure 3.1: Normalized $\boldsymbol{\lambda}$ field, resulting from (3.3) and the corresponding $\boldsymbol{\beta}^{\theta}$ field.

Note that, as mentioned in section 2.2, the $\boldsymbol{\beta}$ field may not be as localized as $\boldsymbol{\beta}^{\theta}$ since

$$\boldsymbol{\beta} = \text{curl}(\boldsymbol{E})$$

$$\beta_{ij} = e_{jkl} E_{il,k}$$

$$= e_{jkl} \Big(\frac{\partial n_i}{\partial \theta} E_l^{\theta} \Big)_{,k}$$

$$= e_{jkl} \Big(\frac{\partial^2 n_i}{\partial \theta^2} \theta_{,k} E_l^{\theta} + \frac{\partial n_i}{\partial \theta} E_{l,k}^{\theta} \Big)$$

$$= e_{jkl} \Big(\frac{\partial^2 n_i}{\partial \theta^2} \theta_{,k} (\theta_{,l} - \lambda_l) + \frac{\partial n_i}{\partial \theta} E_{l,k}^{\theta} \Big),$$

and noting that $e_{jkl} E_{l,k}^{\theta} = \beta_j^{\theta}$ and $e_{jkl} \theta_k \theta_l = 0$,

$$\beta_{ij} = -e_{jkl} \Big(\frac{\partial^2 n_i}{\partial \theta^2} \theta_{,k} \lambda_l \Big) + \frac{\partial n_i}{\partial \theta} \beta_j^{\theta}. \tag{3.4}$$

One can easily see that while the second term is localized inside the defect core, the first term is not necessarily zero inside the layer. However, since $\theta_{,k}$ decays sharply from the defect core, the effect of this term vanishes rapidly away from the core. Figure 3.2 shows this deviation from being a perfectly localized field.

20

(a) $|\tilde{\boldsymbol{\beta}}|$ (b) $\log(|\tilde{\boldsymbol{\beta}}|)$
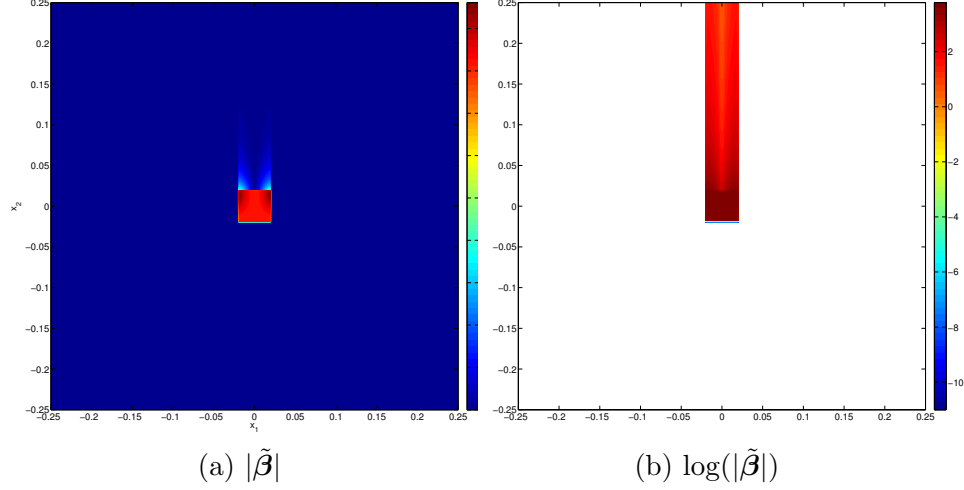
Figure 3.2: Normalized $\boldsymbol{\beta}$. The affects of the first term in (3.4) are more obvious in the logarithmic plot. The white area in part (b) represents zero for $\tilde{\boldsymbol{\beta}}$

Equations (2.7), (2.14), and (3.3) yield the director field from the following Poisson's equation

$$div\,(grad\,\theta) = div\,\boldsymbol{\lambda}. \tag{3.5}$$

As a close reference point for the numerically computed approximate director solutions that are generated subsequently, the closed-form solution of (3.5) in an infinite domain is derived in the Appendix A corresponding to smooth approximating sequences to the discontinuous layer fields, i.e. (3.2)-(3.3), we consider. We have used the Galerkin finite element method to solve (3.5).

In order to compare our energy and director field results with those available in the literature (e.g. [43]), we will consider *line wedge disclinations in an infinite space*. To compare the results with Frank's planar model, we consider the following equation with Neumann boundary condition:

$$\begin{cases} div\,grad\,\theta = div\,\boldsymbol{\lambda} & \text{on } V \\ grad\,\theta \cdot \boldsymbol{\nu} = grad\,\phi \cdot \boldsymbol{\nu} & \text{on } \Gamma, \end{cases}$$

where Γ is the exterior boundary of the finite domain V and ϕ is the angle of the director field with the x_1 axis in Frank's solution [30]:

21

$$\phi = K \tan^{-1}\left(\frac{x_2}{x_1}\right) + c \tag{3.6}$$

with c a constant. For the purpose of evaluating the boundary condition for the domains involved, it suffices to consider $grad\,\phi$ to be given by

$$\frac{K}{r^2}\left(-x_2 \boldsymbol{e}_1 + x_1 \boldsymbol{e}_2\right) \tag{3.7}$$

(to the neglect of a surface Dirac distribution related to the discontinuity in Frank's solution (3.6)). Moreover, one must assign the value of θ at one point in the domain for uniqueness of solutions. Note that this assignment is tantamount to fixing c in Frank's solution. We choose to assign a value θ_0 at one point on the right-hand-side boundary of the layer/strip on which $\boldsymbol{\lambda}$ has support.

Now, using this Neumann boundary condition, the weak form of (3.5) for use in the Galerkin finite element method is

$$\int_V \delta\theta_{,i}\left(\theta_{,i} - \lambda_i\right) dV - \int_\Gamma \delta\theta \phi_{,i} \nu_i dS = 0. \tag{3.8}$$

Here $\delta\theta$ is a continuous test function for θ. Bilinear, 4-node, quadrilateral elements are used for our simulations. Needless to say, the resulting θ will be a continuous field and we show converged results for the director field with mesh refinement in Figure 3.14b.

Figure 3.3 shows the result of solving (3.8) for θ, plotted as director fields using (2.4), for different disclination strengths. In all of these examples, $\theta_0 = \frac{\pi}{2}$, except in Figure 3.3d. These director fields are completely analogous to those from Frank's solution (3.6), outside the layer.

However, inside the strip, the continuous θ field has to compensate the jump between the two sides of the layer. As a result, one can see that inside the layer,

(a) $K = \frac{1}{2}$ (b) $K = -\frac{1}{2}$ (c) $K = 1$, $c = 0$

(d) $K = 1$, $c = \pi/4$ (e) $K = -1$ (f) $K = \frac{3}{2}$

(g) $K = -\frac{3}{2}$ (h) $K = 2$ (i) $K = -2$
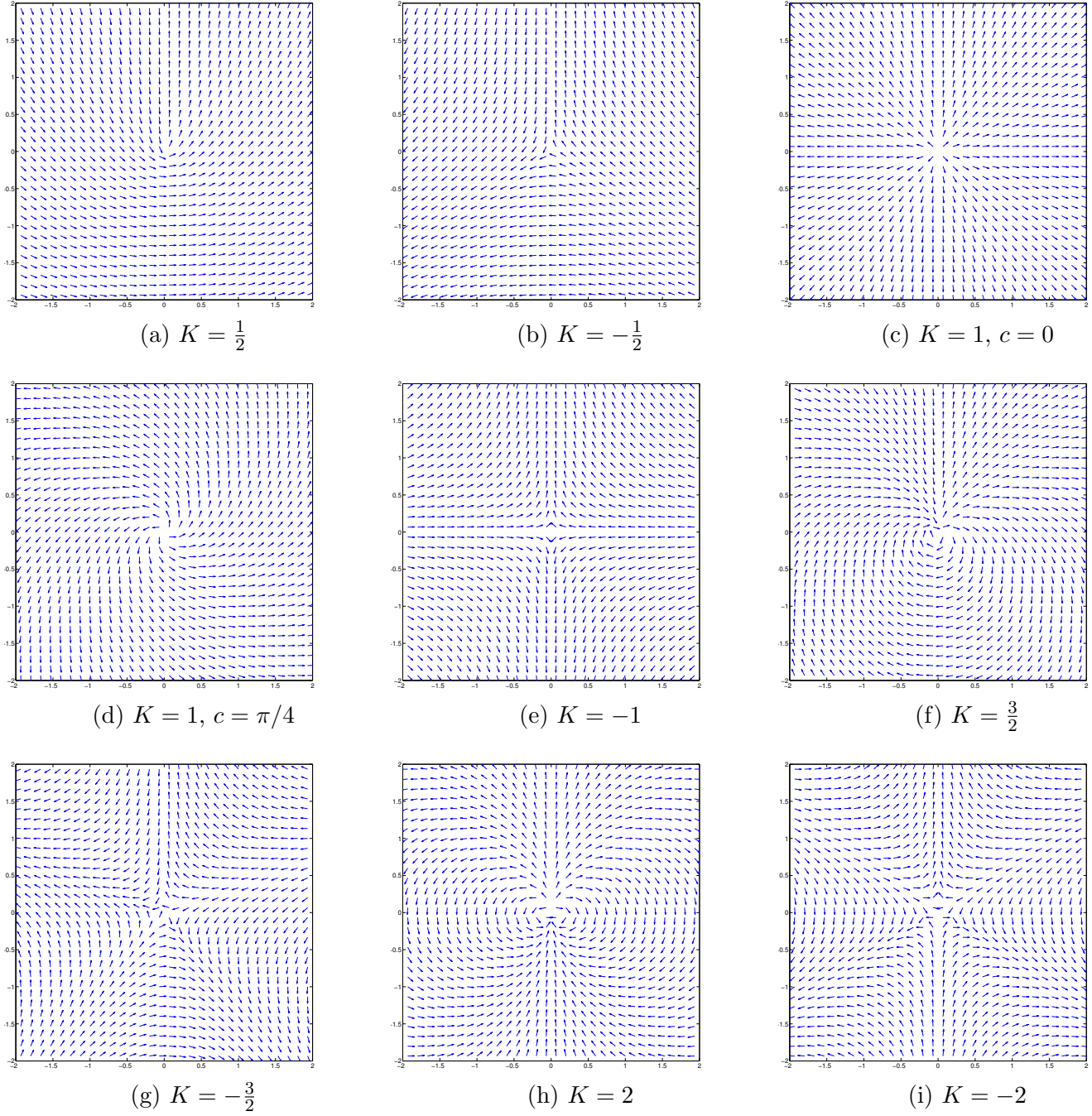
Figure 3.3: Computed director fields with wedge disclination at the center for different disclination strengths. Part (c) and (d) have the same disclination strength but different prescribed values (θ_0), which directly affect constant c in Frank's model (3.6)

directors rotate sharply from one side to the other *but at no extra energy cost in the layer beyond what is involved in the standard interpretation of the energy due to Frank's solution, i.e. the energy arising from considering the director gradient field to be (3.7)*. This is due to compensation by the $\boldsymbol{\lambda}$ field - more precisely, by the *grad z* part of the $\boldsymbol{\lambda}$ field. Moreover, the topological content of the standard interpretation, i.e. (3.7), of the singular gradient of Frank's solution (3.6) is preserved in the $\boldsymbol{E}^\theta$ field and approximately in the gradient of continuous θ field (up to the layer). Within this setting, even in the case of an integer defect, although there is no apparent discontinuity between the directors on the left and right side of the layer, there exists a 2π transition within the layer. In order to have a better understanding of this compensation, we take a closer look at the case $K = \frac{1}{2}$. Figure 3.4 shows the rotation of the director field, inside the layer. Note that the rotation of the director field inside the layer is opposite in sense to its rotation outside of the field.
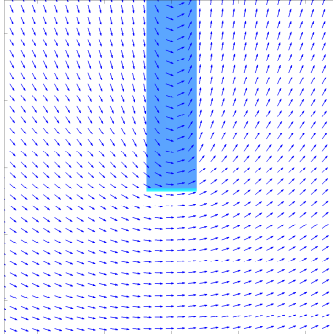
Figure 3.4: A closer look at the computed director field for $K = \frac{1}{2}$. The colored strip depicts the layer field, $\boldsymbol{\lambda}$. If one makes a clockwise circuit around the defect core, the rotation of the directors will be clockwise, outside of the layer, while it is anti-clockwise inside.

Next, we compare the energy density field of our theory to the corresponding one of Frank's model. Using (2.5), the energy term for Frank's planar model will be

$$\psi_F(\boldsymbol{n}, \boldsymbol{E}) = \frac{\kappa}{2} \frac{K^2}{r^2}$$

(using the standard interpretation of the gradient). Evidently, the total energy in a finite body for such an energy density field will not be finite. However, the energy density of the defects we model is non singular in most cases and definitely integrable in all cases, so that the total energy will be finite. The energy density of our model can be calculated from the following expression:

$$\psi(\boldsymbol{n}, \boldsymbol{E}) = \frac{1}{2}\kappa(\theta_{,i} - \lambda_i)(\theta_{,i} - \lambda_i).$$

Figure 3.5 shows energy contours normalized with respect to K and κ, outside the defect core:

$$\tilde{\psi}_F = \frac{1}{\kappa K^2}\psi_F = \frac{1}{2r^2} \qquad \tilde{\psi} = \frac{1}{\kappa K^2}\psi.$$

In this Figure, we have also compared the decay of the energy density as it moves away from the defect core. According to ψ_F, such decay must follow a $\frac{1}{r^2}$ trend. The results from our setting shows good agreement with the analytical results outside the core, while being nonsingular inside, Figure 3.5.

(a)   (b)
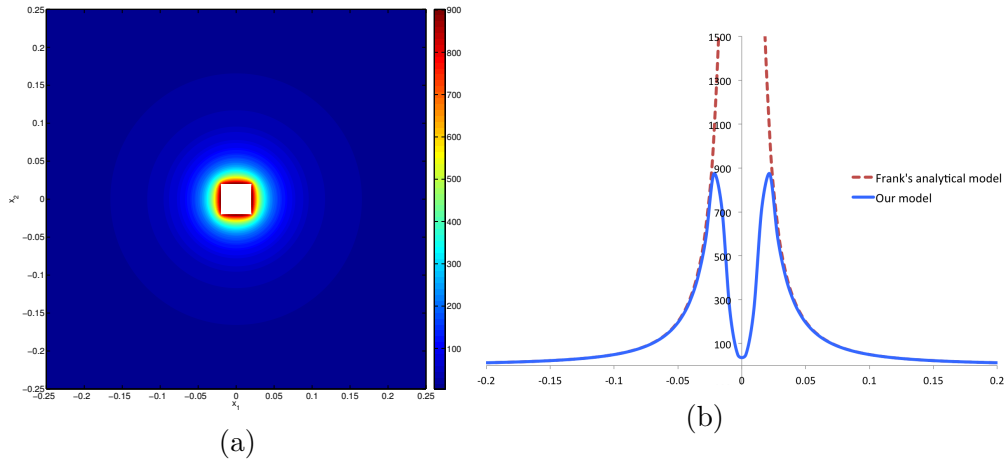
Figure 3.5: (a) Normalized energy density contour outside of the defect core and, (b) The decay of energy density when $x_2 = 0$.

Note that not only is the energy density in our model non-singular at the center, but Figure 3.5b shows that the energy density profile drops dramatically at the

25

center of the defect core. Later, in **??** we will show that the energy level at this point converges to zero. However, this is not a general rule. In fact the energy density profile inside the core depends on the distribution of the layer field, $\boldsymbol{\lambda}$, and consequently $\boldsymbol{\beta}^\theta$. For instance, if we cut off the layer field at the center of the defect core instead of letting it decay linearly, i.e. use (3.2) for the layer field definition, the energy density will be as in Figure 3.6. Figure 3.6b reveals the fact that although such sharp cut off in the layer field will cause unsymmetric energy density distribution inside the defect core, the energy density will still be radially symmetric outside the core.
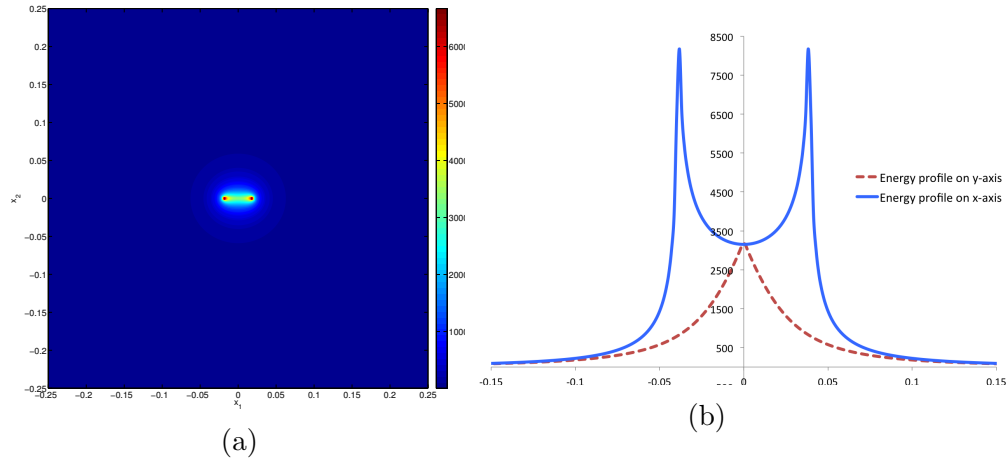
Figure 3.6: (a) Normalized energy density contour when $\boldsymbol{\lambda}$ sharply ends at the center, (b) The corresponding energy density profile in cases $x_2 = 0$ (blue, solid line) and $x_1 = 0$ (red, dashed line).

We also note that even though in this case we have a singular wall-like distribution of $\boldsymbol{\beta}^\theta$ at the core edge that can potentially cause singularities in the energy density at the sharp corners defining the layer, the total energy for a fixed width of layer will always converge as long as $r_1 > 0$, i.e. the layer has finite width. This is borne out in our computations where the total energy corresponding to Figure 3.6 appears to converge, as shown in Figure 3.7.
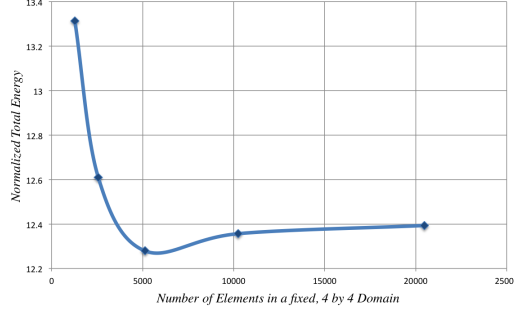
Figure 3.7: Convergence of the normalized total energy, corresponding to the energy density shown in Figure 3.6 with the increase of the number of elements used in a fixed domain.

3.1.2 Straight twist disclination

Twist disclinations have the axis of rotation of the director field perpendicular to the defect line. They are sometimes called *perpendicular* disclinations.

From the mathematical point of view, we use the same definition for the planar director field as in equation (2.4). While the $\boldsymbol{n}$ field lies in the $x_1 - x_2$ (horizontal) plane, θ is assumed to be a function of x_1 and x_3 and it is constant along the x_2 direction. The definition of the layer field undergoes similar, appropriate changes. We define $\boldsymbol{\lambda}$ as in (3.2), but now in the $\boldsymbol{e}_3$ direction instead of $\boldsymbol{e}_1$ (for direction of $\boldsymbol{\lambda}$ and the width of the layer) as shown in Figure 3.8a. We perform a 3-d finite element computation in this case. The computed energy density concentration is shown in Figure 3.8b. The distribution of the energy and its decay on the vertical plane is exactly the same as shown in Figure 3.5 for the straight wedge disclinations, which is consistent with expectation. Figure 3.8c and Figure 3.8d, respectively, show the computed and analytical director fields.

3.2 Twist Disclination loops

Disclination loops are more commonly found in nature than curves terminating at boundaries [39]. In this section we will simulate a twist disinclination loop, using

27
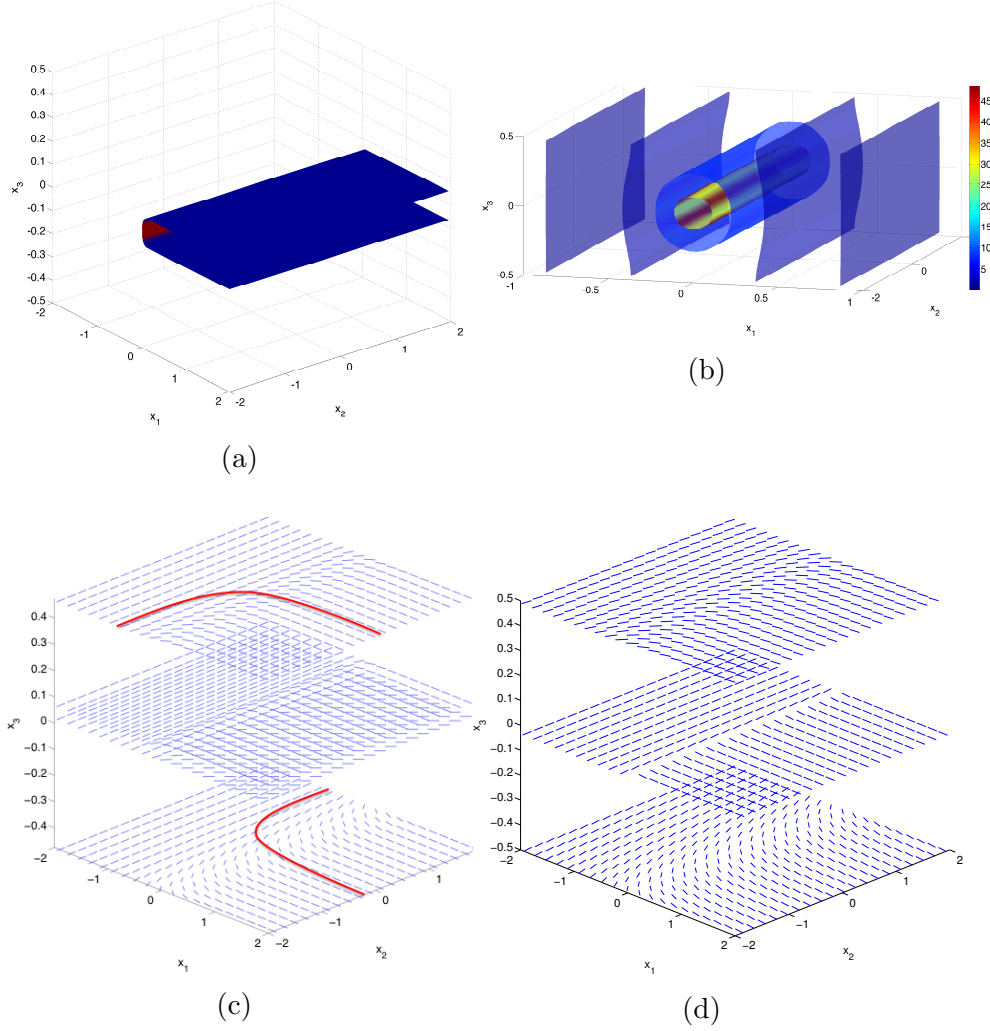
Figure 3.8: Straight twist disclination: (a) 3D plot of the layer field, $\boldsymbol{\lambda}$, (b) a 3D plot of different layers of the normalized energy density to illustrate the energy density distribution in the body, (c) is the computed director field, while (d) is the analytical one.

our framework.

The director field will be planar, but now the θ field will be a function of x_1, x_2 and x_3. The $\boldsymbol{\lambda}$ field for a planar twist disclination loop is taken to be a constant field in a bounded layer as can be seen in Figure 3.9. The bounding cylinder of the layer over which the constant field decays to zero then forms the disclination loop. Clearly, the closed loop can be of any shape, but restricted to be planar in this exercise.

28
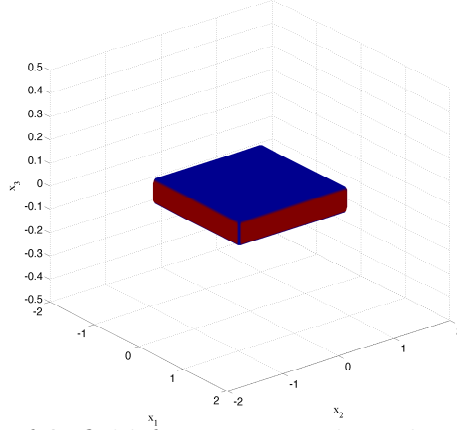
Figure 3.9: An example of $\boldsymbol{\lambda}$ field for a square-shaped twist disclination loop. The field vanishes in the white region.

In particular, we have chosen a square-shaped and a circular loop in the horizntal plane. $\boldsymbol{\beta}$ and $\boldsymbol{\beta}^\theta$ field for the rectangular loop are shown in Figure 3.10. Just like the 2-dimensional wedge disclination case, the $\boldsymbol{\beta}^\theta$ field is non-zero only at the defect core which appears as a square loop, and $\boldsymbol{\beta}$ is non-zero inside the loop, where the layer field is non-zero.

(a)   (b)
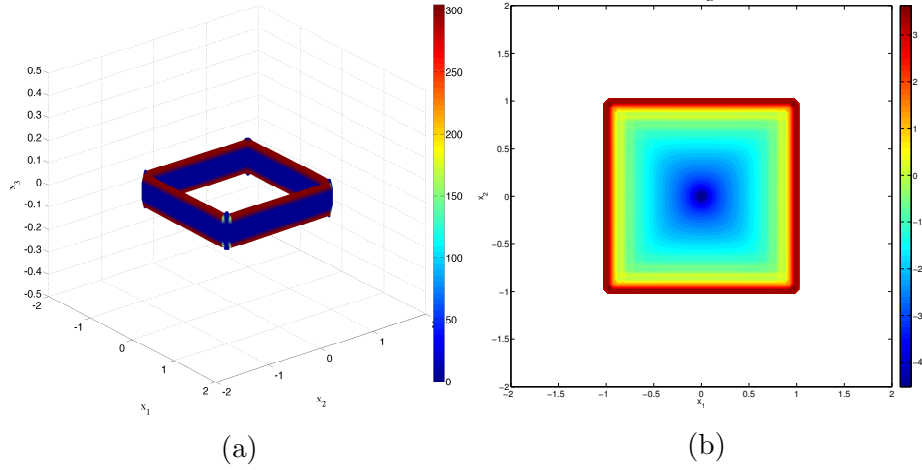
Figure 3.10: (a) Normalized $\boldsymbol{\beta}^\theta$ for the twist disclination loop and (b) Logarithmic contour plot of normalized $|\boldsymbol{\beta}|$. The white area in part (b) represents zero for $|\boldsymbol{\beta}|$.

The director field is a planar vector field with twist axis along the x_3 direction. As shown in Figure 3.11, in any given plane $x_3 = constant$ the effect of the loop

29

decays rapidly with distance from the loop. Figure 3.11 also clarifies the way in which the director vectors make a twist as one moves through a circuit enclosing the core. Note that the director vectors corresponding to the lower part of the $\boldsymbol{\lambda}$ field have the opposite direction of the ones on the top, since that is a half-integer disclination loop $(K = \frac{1}{2})$ and as a result the director field makes a π-radian twist. We emphasize that while this twist deficit is observable in the (continuous) director field only on circuits that are 'closed up to the thickness of the core', integrating $\boldsymbol{E}^\theta$ on an exactly closed circuit encircling an arm of the disclination loop core would yield a π-radian twist by design.

(a) Square-shaped loop   [Circular loop]
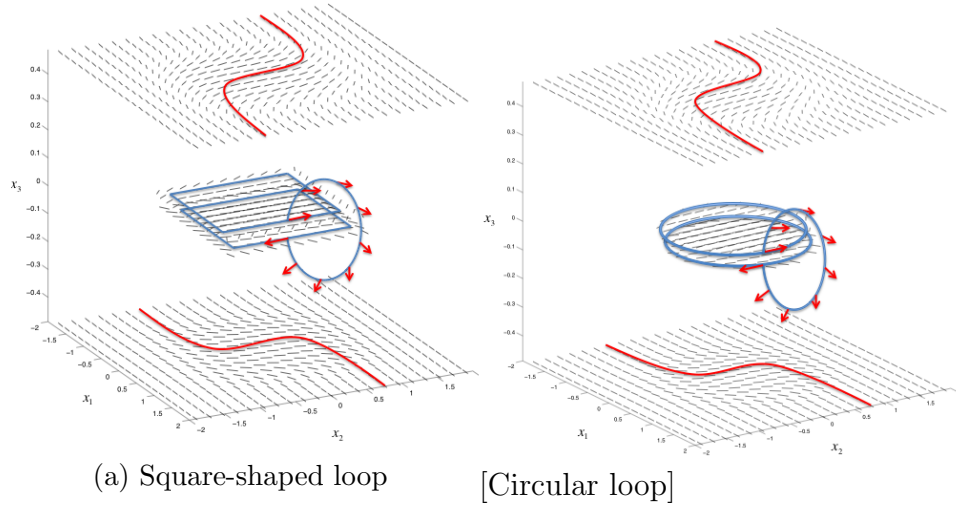
Figure 3.11: Computed director fields of twist disclination loops for $K = \frac{1}{2}$.

Figure 3.12 shows the energy plots of the two disclination loops from different points of view. Figure 3.12a and Figure 3.12b are the energy density contours at $x_3 = 0$, on the $x_1 - x_2$ plane for the square-shaped and circular loop, respectively. Note that the energy density of the rectangular loop has significantly higher magnitude at the corners, this being a consequence of the high curvature in the director field at the corners of the loop. Similar to what we saw in Figure 3.5b, these contour plots show a drop in magnitude inside the core. This plot also shows smoothness of the energy

density, even in the vicinity of the defect core. In order to better understand the pattern of the energy density on this plane, Figure 3.12c and (Figure 3.12d show the logarithmic scale of the plot. A closer look at these two plots reveals that even for the rectangular defect core the energy density adopts a radially symmetric patter away from the core. The observable deviation from this circular texture on the boundary is due to the zero Neumann boundary condition that we have used for these two examples. Figure 3.12e and Figure 3.12f show the logarithmic plot of the energy density on the $x_1 - x_3$ plane.

3.3   Convergence of numerical results

One of the main advantages of our model is the possibility of attaining non-singular results in energy density. In this section we have verified this claim by refining the mesh in our numerical model to demonstrate convergence even inside the defect core. Figure 3.13 shows this convergence for the straight wedge disclination. Since the results for different disclination strength are similar, we have normalized our energy plots with respect to K.

 The energy density results for our model and Frank's analytical model are the same, outside the core. Figure 3.14 shows a relative error of less than 1% everywhere for the energy density, and less than 0.6% for the director field (outside of the layer) for the half-integer defect. Results for all other disclination strengths show the same error distribution.

Finally, Figure 3.15 shows the convergence of the energy density in the square-shaped twist loop model. In this Figure, the energy density profile of the loop with two different element sizes has been compared on the x_1 axis, i.e. on the line $x_2 = 0, x_3 = 0$.

(a)

(b)

(c)

(d)

(e)

(f)
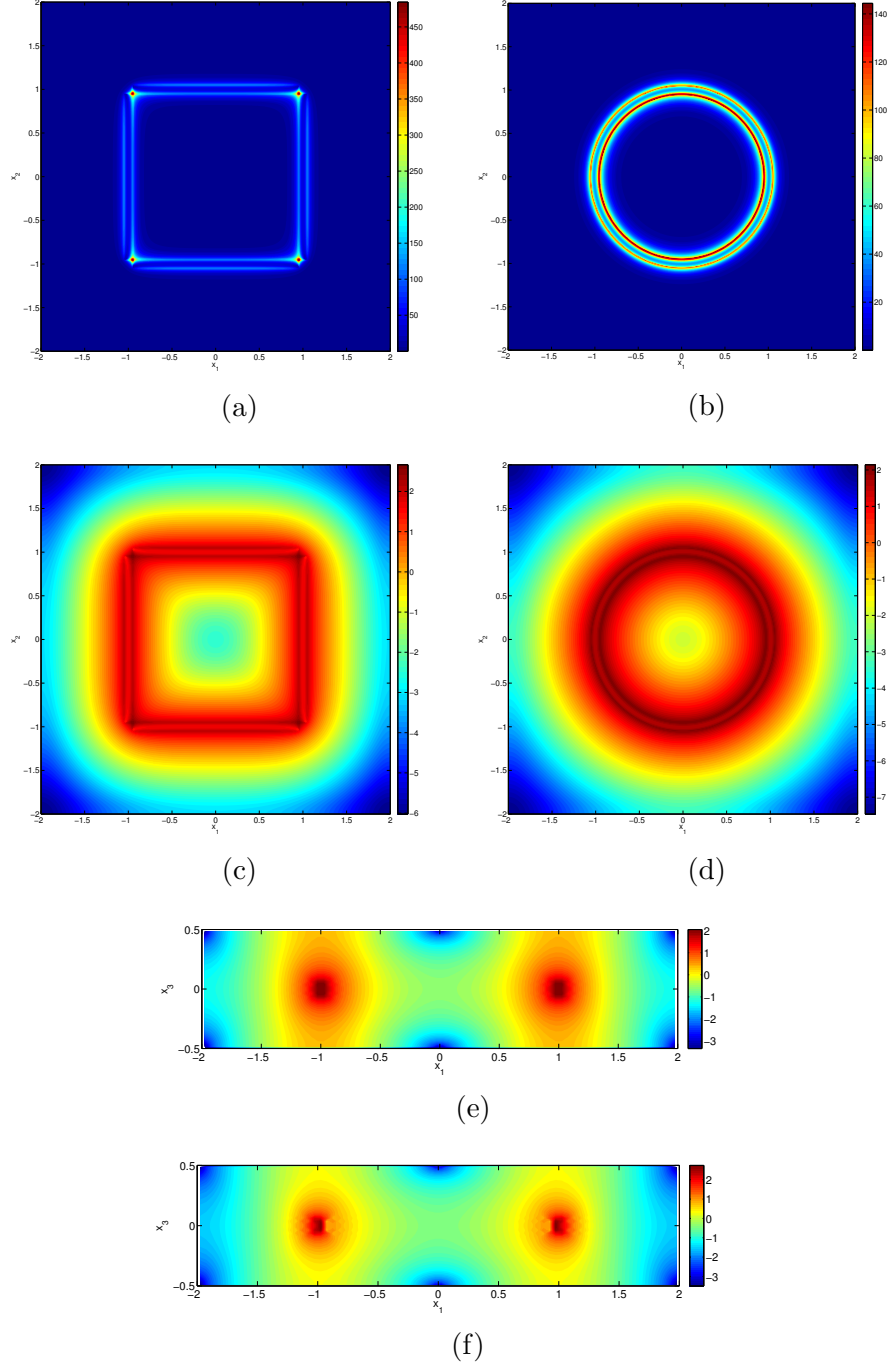
Figure 3.12: Energy plot of the twist disclination for square-shaped and circular loops: (a) and (b) are the contours of the normalized energy density, where $x_3 = 0$, (c) and (d) show the decay of the same contours, in a logarithmic scale. Also, (e) and (f) are the logarithmic contour plots of the energy density in $x_1 - x_3$ plane, where $x_2 = 0$.
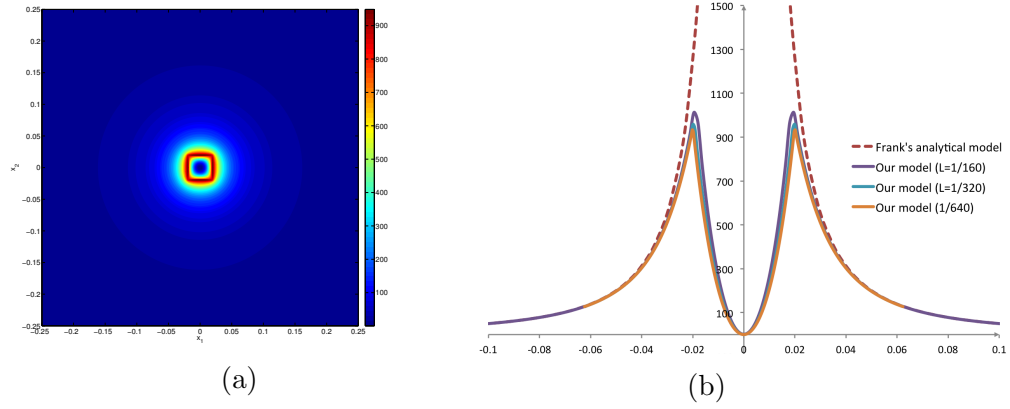
Figure 3.13: (a) Normalized energy density contour of wedge disclination including the defect core and (b) The decay of energy density when $x_2 = 0$, for different element sizes, L.
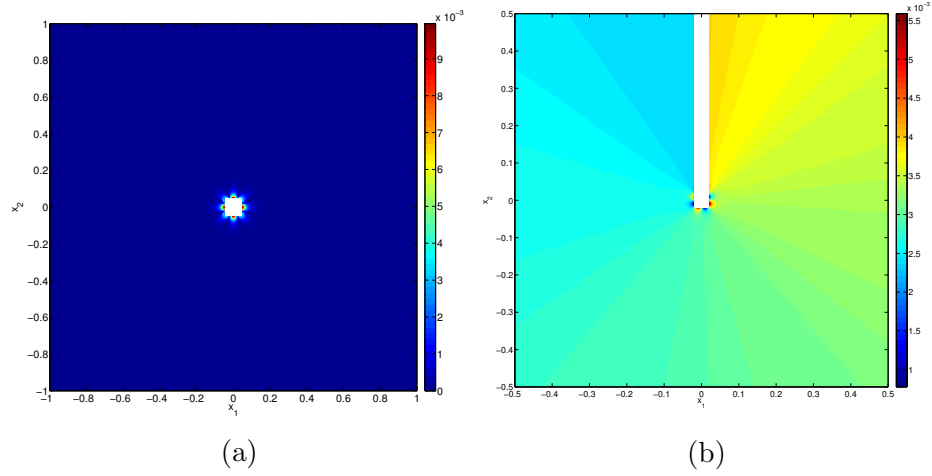
Figure 3.14: Comparison of the computed results from the model with Frank's model: (a) Relative error of energy for wedge disclination, (b) Relative error of director field for wedge disclination.
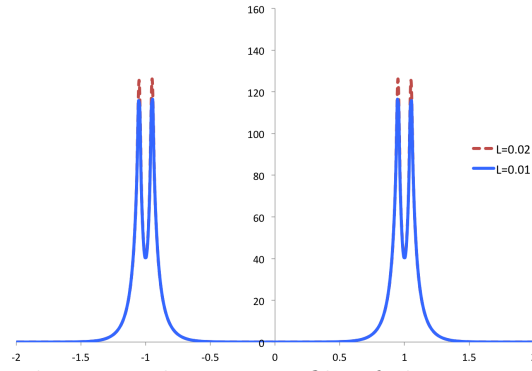
Figure 3.15: Normalized energy density profile of the twist disclination for the rectangular loop in Figure 3.12a, when $x_2 = 0$. The element sizes are $L = 0.02$ (red, dashed line) and $L = 0.01$ (blue, solid line).

4

Balance of forces

Assuming a single disclination in the body (loop or a core cylinder terminating at the boundaries of the body), static balance of linear momentum (2.2) is satisfied in the region of the body excluding the core. This is so since the stress tensor is given by

$$T_{ij} = -p\delta_{ij} - \kappa E_i^\theta E_j^\theta$$

and (2.7) and (2.9) imply, along with the core-support of $\boldsymbol{\beta}^\theta$, that

$$(E_i^\theta E_j^\theta)_{,j} = (E_j^\theta E_j^\theta)_{,i} = \frac{\psi_{,i}}{\kappa},$$

and one chooses the indeterminate constraint pressure field in the excluded-core region of the body as

$$p = -\psi,$$

to satisfy (2.2). On the external boundary of the body, recognizing (2.10) one chooses $p = 0$. Thus, the resultant force on the surface of the core cylinder (or any other surface enveloping it) must vanish.

An interesting possibility is afforded by the model [5] in satisfying static balance of linear momentum everywhere. Note that within the core $curl\boldsymbol{E}^\theta$ does not vanish

so that it is not *a priori* clear that $(E_i^\theta E_j^\theta)_{,j}$ can be expressed as the gradient of a scalar field. However, the vanishing of the *curl* of the field $(grad\boldsymbol{E}^\theta)\boldsymbol{E}^\theta$ along with the conditions (2.7-2.8-2.9) within the core region may be imposed as a design constraint on the $\boldsymbol{\beta}^\theta$ field. Were solutions to exist to this system for $\boldsymbol{\beta}^\theta$, then one could proceed to set up the field $\boldsymbol{\lambda}$ as before with the caveat that now the field $curl\boldsymbol{\lambda}$ within the core is not subject only to the mild constraint (2.8) but instead to the pointwise constraint defined by our calculated $\boldsymbol{\beta}^\theta$ field.

Alternatively, the theory also allows the ansatz

$$\boldsymbol{E} = \sum_{\alpha=1}^{2} \frac{\partial \boldsymbol{n}}{\partial \theta^\alpha} \otimes \left[grad\,\theta^\alpha - \boldsymbol{\lambda}^\alpha\right], \tag{4.1}$$

and choosing this affords four more degrees of field degrees of freedom to satisfy static balance of linear momentum without body forces simultaneously with balance of angular momentum - presumably even without necessarily requiring the constraint of incompressibility. Moreover, the solutions generated in this paper would seem to suggest that these extra degrees of freedom could be invoked only in the core cylinder, thus conferring an automatic multiple spatial length scale feature to the theory. Of course, with static balance of linear momentum satisfied everywhere (including cores), the resultant force of the Ericksen stress tensor (and hence the energy-momentum tensor of the classical nematic theory [29, 19]) on the bounding surface enveloping any segment of a core has to vanish without the requirement of any externally applied body forces or the onset of flow, while the [5] dissipative dynamical theory provides a driving force for disclination motion not related to the Ericksen stress or its resultant. This possibility has the potential of reconciling several different points of view and clarifying an often confusing debate in the liquid crystal literature (cf. [29, 46, 27]) revolving around the physically meaningful question of modeling the experimentally observed motion of disclination curves in the presence

of negligible or no flow.

5

Concluding Remarks

We have demonstrated the possibility of representing non-singular isolated disclination fields within a dynamic theory [5] of liquid crystalline media designed to account for disclination and dislocation defects. The solutions satisfy balance of moments everywhere in the body, including the core. Balance of forces is satisfied outside the cores and it appears possible, by going beyond the ansatz (2.3) assumed in this work, to satisfy force balance everywhere in the body. The fields constructed here may be considered to be equilibria for the theory when the defect lines are considered to be externally-pinned (i.e. the defect velocity field, a constitutive quantity, is assumed to vanish).

Our primary goal has been to demonstrate distinguished pairs of director and (incompatible) director distortion fields $(\boldsymbol{n}, \boldsymbol{E})$ satisfying (2.1) and (2.9) that generate classically familiar director and energy density fields of disclinations (but not exactly the same ones). In doing so, we use an intermediary 'layer' field which, thankfully, is not required in the subsequent dynamics of the [5] model once the director and the director distortion fields have been constructed. However, a fact that gives us pause is that the director incompatibility tensor field $\boldsymbol{\beta}$ of these isolated disclinations ap-

pear to contain some signature of the layer field used to construct them even outside the region that one would typically like to associate with the core of the disclination, and whether this is physically realistic or not remains to be seen. Also, the director fields that we construct have a rapid variation in the layer (without a corresponding energy cost), and the physical realism of such a distribution should also be testable in the modeling of situations involving interaction of the director field with flow. Of course, the analysis presented in Section 2.2 provides the logic to construct a director and director incompatibility field without the layer-related features discussed above. To wit, considering the example of the axial wedge disclination of Section 3.1 in an infinite domain, we define

$$\boldsymbol{\lambda}_s = grad\, z_s + \boldsymbol{E}_r^\theta$$

where

$$div(grad\, z_s) = div\, \boldsymbol{\lambda}_s$$

and $\boldsymbol{\lambda}_s$ is the distribution obtained in (3.2) by letting $r_1 \to 0$. This results in z_s being exactly Frank's solution (3.6). Additionally, we let $\boldsymbol{E}_r^\theta$ be the solution to

$$div\, \boldsymbol{E}_r^\theta \;=\; 0$$
$$curl\, \boldsymbol{E}_r^\theta \;=\; \boldsymbol{\beta}_r^\theta,$$

(with natural decay requirements at large distances) where $\boldsymbol{\beta}_r^\theta$ is a radially symmetric core function described in Appendix B with associated solution for $\boldsymbol{E}_r^\theta$. This formula shows that outside the core, $\boldsymbol{E}_r^\theta$ matches the standard interpretation (3.7) of the gradient of Frank's solution (3.6). Setting $\boldsymbol{E}^\theta := grad\,\theta - \boldsymbol{\lambda}_s$ and requiring it to satisfy the governing equations of our model, i.e. (2.7) and (2.9), a (discontinuous) solution is certainly $\theta = z_s$, with discontinuity supported on the half plane defined by $r_1 \to 0$ in the definition (3.2) of $\boldsymbol{\lambda}_s$. These results imply that outside the core and away from the half-plane $x_1 = 0, x_2 > 0$, $\boldsymbol{E}_r^\theta$ matches grad θ. Assuming the validity

39

of (2.15) on the half-plane and noting that the $grad\,\theta$ and $\boldsymbol{E}^\theta$ fields are parallel to $\boldsymbol{e}_1$ on it, it may be concluded that $\boldsymbol{\beta}$ is non-vanishing only inside the core. With $\boldsymbol{E}^\theta$ defined as in this paragraph, we note that even though $grad\,\theta$ is not a locally integrable field, this is exactly compensated by $grad\,z_s$ so that the energy density is formed from the field $\boldsymbol{E}^\theta_r$ alone. In this connection, we note the interesting fact that the classical defect theory works with a director-'gradient' field for forces, moments and energetics that is not strictly a generalized derivative of what it states as the director field (even outside the core)[1]. Thus, it would seem that considering the energy formed from a director distortion field distinct from the director gradient in the presence of line defects (as we do) is probably a reasonable logical device even for discussing the classical theory.

This paper has not made any statements about whether the chosen isolated defect-like director and director distortion fields can actually occur as equilibria of the overall dynamical model [5] for suitable constitutive assumptions for defect velocities (e.g., a linear kinetic assumption on disclination velocity as a function of its theoretical driving force). Based on our experience with related work on Field Dislocation Mechanics [2], [4], [3], we believe this should be possible with the use of non-convexity in OZF energy (possibly due to a limit on director elasticity), the system (as opposed to scalar) nature of the defect evolution equations, as well as from appropriate boundary conditions. In the presence of flow, there are, of course, other natural means to induce line defects.

There are many natural further steps to explore: solving for more-than-planar

---

[1] The analog of Weingarten's construction to be utilized here makes it entirely clear why this must be so - there, one begins with an irrotational field in a doubly-connected 3-d domain with a through-hole and what may be associated as the 'closest' potential field generating the irrotational field is not defined on the same domain but rather on a simply-connected domain obtained through a single cut of the doubly-connected domain that renders the latter simply-connected. Unfortunately, however, these are not procedures that lend themselves to practical nonlinear theory, especially of the type interpretable by the intelligence level of electronic computers that are essential to probe the complex dynamics of the theories we have in mind.

fields of isolated defects, defect solutions for the full 4-constant Oseen-Frank energy, solutions for disclinations coupled to dislocations in smectics and columnar phases and on to dynamics with and without flow (without flow and even without director inertia, the model has dynamics due to defect evolution). While each of these problems are significant in their own right, we take some satisfaction in the fact that all of these questions can at least be posed unambiguously within our modeling framework. Finally, an important future task is to make contact with the fine topological work of Kleman and Friedel [42] and Kamien and co-workers [20].

Part

II

Electron Scattering in Defected Crystals

6

Introduction

Wave propagation and scattering waves in an infinite or very large domains has many applications in both science and engineering. Traveling waves in elastodynamics [13, 9], photonics crystals [62], semiconductors [12] and electromagnetism [56, 21] are a few examples of the application of wave propagation in infinite space.

In quantum mechanics, this issue has been addressed in numerous studies. [61, 17, 60, 15, 68] used Green's function to solve the Schrodinger's equation in a perturbed medium. This method, although very accurate, is only limited to point defects and local perturbations. In an other method, [24, 8] truncated the unbounded domain and proposed a proper artificial boundary condition to not only keep the problem well-posed, but also avoid spurious reflecting waves, due to the truncation. In this method the artificial boundary conditions, ABC, may be represented as an exact but non-local [31] or a local approximate [32] of Dirichlet-to-Neumann (DtN) mapping. However, the proposed methods so far, are limited to compactly supported potentials or the bound state wavefunctions, where the wavefunction exponentially vanishes at infinity.

A very efficient and generic technique for scattering waves is using absorbing lay-

ers on the boundary of the truncated domain. [14] showed that such layer can be constructed for Maxwell's equation in a way that they absorb all incoming energy without creating any reflecting wave. Such a layer is called *Perfectly Matched Layer*. [21] then showed that these absorbing layers can be simply defined by complex coordinate stretching in three dimensions. From an engineering point of view, PML can be represented as a fictitious material, which absorbs the waves away from the region of interest, without any influence on the pattern of the scattering waves outside of the layer. However, PML was originally designed for continuous and homogeneous spaces and it looses its "Perfectly Matched" advantage, as soon as the domain is discretized or the environment is inhomogeneous [48].

Despite that fact that under such circumstances PML will cause reflecting waves, it can still be used as an absorbing layer. [59] showed that by choosing a smooth absorption function, one can control the amount of spurious waves with increasing the width of the layer. Although, there has been a great deal of attention on this subject in the past decades, there is yet to find a rigorous technique to solve elliptic equations with periodic coefficients in an infinite domain. In this thesis, we derive the asymptotic form of the wave functions in a periodic media and study the possibility of constructing a proper boundary condition for periodic Schrodinger equation with local perturbations in the potential function. We apply the perfectly matched layer method in inhomogeneous media and show that the results will converge as the thickness of the absorbing layer increases.

Moreover, we apply the Green's function technique to find the exact. Such boundary condition will be highly non-local and (compared to the PML method) too expensive for practical purposes. However, we show that by applying certain approximations, we can reduce the cost of this boundary condition significantly. Also, for multi-dimensional domains we propose a technique to reduce the number of boundary points, for which one needs to apply the non-reflecting boundary condition.

The outline of the rest of the thesis is as follows. First we will present the formulation of the Schrodinger equation for scattering wavefunction in Section 3. Also, we study the Perfectly Matched Layer method, as well as the exact non-reflecting boundary condition for the scattering wave in a periodic media. The tight-binding formulation and implementation of the boundary conditions are presented in section 4. After that, we have demonstrate our theory with numerous examples of Graphene sheet, single-walled Carbon nanotubes, Y-junction Carbon nanotubes and kinked DNA molecules in section 5. At the end we have concluded the thesis in section 6.

7

Non-reflecting boundary conditions

7.1   Formulation of the model

For a periodic media with local defect, we will consider the time-harmonic Schrodinger equation,

$$-\frac{1}{2}\nabla^2\phi(\boldsymbol{x}) + V(\boldsymbol{x})\phi(\boldsymbol{x}) = E\phi(\boldsymbol{x}) \tag{7.1}$$

Here, E is the energy of wavefunction $\phi(\boldsymbol{x})$. In such media, one can assume that the potential can be decomposed into a non-vanishing periodic potential, $V_p(\boldsymbol{x})$, and a localized potential, $V_d(\boldsymbol{x})$ with compact support, which represents the defect or impurity in crystal:

$$V(\boldsymbol{x}) = V_p(\boldsymbol{x}) + V_d(\boldsymbol{x}) \tag{7.2}$$

Further, knowing that far away from the perturbations the wavefunction converges to the solution of the periodic Schrodinger equation, one can also decompose the wavefunction

$$\phi(\boldsymbol{x}) = \phi_k(\boldsymbol{x}) + \psi(\boldsymbol{x}) \tag{7.3}$$

where $\psi(\boldsymbol{x})$ and $\phi_k(\boldsymbol{x})$ represent the scattering wave and the incident Bloch wave, respectively. Note that $\phi_k(\boldsymbol{x})$ is the solution to the Schrodinger equation in periodic media can can be retrieved from Bloch theorem:

$$-\frac{1}{2}\nabla^2\phi_k(\boldsymbol{x}) + V_p(\boldsymbol{x})\phi_k(\boldsymbol{x}) = E_k\phi_k(\boldsymbol{x}) \tag{7.4}$$

where E_K the the energy corresponds to the wave number $\boldsymbol{k}$. On the other hand, the scattering wave $\psi(\boldsymbol{x})$ is a decaying wave (in $d \geq 2$) that vanishes at infinity. As a result, one can rewrite Eq. (7.1):

$$-\frac{1}{2}\nabla^2\left(\phi_k(\boldsymbol{x}) + \psi(\boldsymbol{x})\right) + \left(V_p(\boldsymbol{x}) + V_d(\boldsymbol{x})\right)\left(\phi_k(\boldsymbol{x}) + \psi(\boldsymbol{x})\right) = E\left(\phi_k(\boldsymbol{x}) + \psi(\boldsymbol{x})\right) \tag{7.5}$$

Now, subtracting equation (7.4) from this equation, we get

$$-\frac{1}{2}\nabla^2\psi(\boldsymbol{x}) + \left(V_p(\boldsymbol{x}) + V_d(\boldsymbol{x})\right)\psi(\boldsymbol{x}) = E\psi(\boldsymbol{x}) - V_d(\boldsymbol{x})\phi_k(\boldsymbol{x}) + (E - E_k)\phi_k \tag{7.6}$$

It is noteworthy to mention that even though the scattering wavefunction $\psi(\boldsymbol{x})$ is the direct result of the defect potential $V_d(\boldsymbol{x})$, it is also influenced by the periodic potential $V_p(\boldsymbol{x})$. As a result, it is a scattering problem in an unbounded, inhomogeneous media and consequently truncating the domain requires especial absorbing boundary condition, which does not produce any significant reflecting wave.

Also, since both $V_d(\boldsymbol{x})$ and $\psi(\boldsymbol{x})$ vanish at infinity, it is easy to see that as $x \to \infty$ the only remaining term in equation (7.6) will be $(E - E_k)\phi_k$, consequently:

$$E = E_k \tag{7.7}$$

As a result, the elliptic equation corresponding to the scattering wave, $\psi(\boldsymbol{x})$ will be:

$$-\frac{1}{2}\nabla^2\psi(\boldsymbol{x}) + \left(V_p(\boldsymbol{x}) + V_d(\boldsymbol{x})\right)\psi(\boldsymbol{x}) = E_k\psi(\boldsymbol{x}) - V_d(\boldsymbol{x})\phi_k(\boldsymbol{x}) \tag{7.8}$$

47
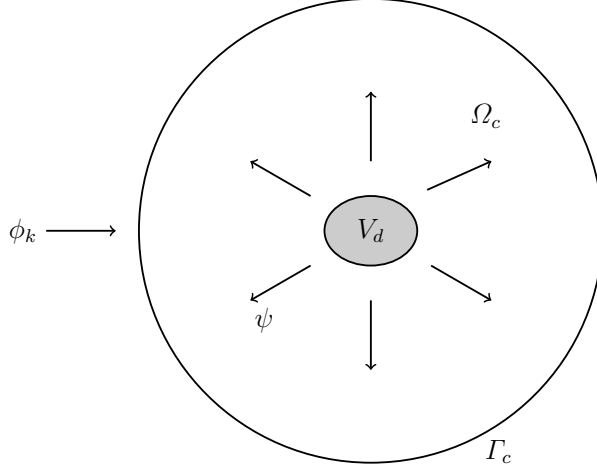
Figure 7.1: The incident wave, ϕ_k, and the scattering wave, ψ, in the truncated computational domain Ω_c

This means the energy of the scattering wave and the incident wave is the same, in all direction of propagation. Since for any direction, there exists a unique wave number, $\boldsymbol{k}$, corresponding to the energy E_k (except for the band-gaps), the knowledge of the scattering wave number will be a significant step forward to find an exact non-reflecting boundary condition, side we no longer need to sum over all possible wave lengths as in Engquist and Majda's well-known boundary condition [25].

Now considering a truncated domain Ω_c, which contains the support of potential $V_d(\boldsymbol{x})$ (as shown in Figure 7.1), one can write the weak-form of equation (7.8). We choose the test function as the complex conjugate of ψ, which vanishes at infinity:

$$\int_{\Omega_c} \nabla \psi^* \nabla \psi + \psi^*(\boldsymbol{x})\big(V_p(\boldsymbol{x}) + V_d(\boldsymbol{x}) - E_k\big)\psi(\boldsymbol{x})dv \tag{7.9}$$

$$-\int_{\Gamma_c} \psi^*(\boldsymbol{x})\nabla\psi(\boldsymbol{x}) \cdot \boldsymbol{n}ds = -\int_{\Omega_c} \psi^*(\boldsymbol{x})V_d(\boldsymbol{x})\phi_k(\boldsymbol{x})dv$$

Our goal is to find the proper boundary condition to replace with the surface integral in equation (7.9). In section 7.4 we derive the Perfectly Matched Layer approach for our problem. But before that, we need to find the radiation condition at infinity, which makes the solution of this problem, unique.

7.2 Asymptotic form of the scattering wavefucntion

Before getting into the implementation of absorbing boundary condition, we demonstrate the asymptotic form of the wavefunction, resulting from equation (7.8). In order to achieve uniqueness in any unbounded scattering problem, a radiation condition at infinity is required. For homogeneous spaces, Sommerfeld proposed his well-known radiation condition in $\mathbb{R}^d$:

$$\lim_{r \to \infty} r^{(d-1)/2} \Big(\frac{\partial u}{\partial r} - \imath k u(\boldsymbol{x})\Big) = 0 \tag{7.10}$$

here, $u(\boldsymbol{x})$ is the scattering wave with wave number $\boldsymbol{k}$ and $r = |\boldsymbol{x}|$. We will show that even though the scattering wave in a periodic media will have the same radial decay as the one in homogeneous space $(r^{\frac{1-d}{2}})$, it will not have the same radiation condition as Sommerfeld proposed [63].

Our first approach was using two-scale method in order to homogenize the periodic media. In C.1 we go through this approach in detail. However, as it is mentioned there the is currently no proof for the choice of our scaling for the periodic potential. Moreover, the expansion of Green's function does not help to find this scaling as it does for electrostatic energy in [53]. As a result, despite the efforts in ?? the homogenization of Schrodinger equation in periodic media is still an open subject for us.

So we start by writing equation (7.8) in the integral form, using the Green's function of the Helmholtz equation:

$$\psi(\boldsymbol{x}) = - \int_{\boldsymbol{y} \in \mathbb{R}^d} G(\boldsymbol{x}, \boldsymbol{y}) \Big(\big(V_d(\boldsymbol{y}) + V_p(\boldsymbol{y}) \big) \big(\psi(\boldsymbol{y}) + \phi(\boldsymbol{y}, \boldsymbol{k}) \big) \Big) dy \tag{7.11}$$

Note that, since the integration is over the entire $\mathbb{R}^d$, we can not use equation (7.11) to evaluate the form of the solution. However, if one uses the Green's function

corresponding to the time-harmonic Schrodinger equation in periodic media:

$$-\nabla^2 G(\boldsymbol{x}, \boldsymbol{y}; E_k) + \big(V_p(\boldsymbol{x}) - E_k\big)G(\boldsymbol{x}, \boldsymbol{y}; E_k) = \delta(\boldsymbol{x} - \boldsymbol{y}) \qquad (7.12)$$

Then the former integral form in (7.11) will change into:

$$\psi(\boldsymbol{x}) = -\int_{\boldsymbol{y}\in\Omega_c} G(\boldsymbol{x}, \boldsymbol{y}; E_k)V_d(\boldsymbol{y})\big(\psi(\boldsymbol{y}) + \phi_k(\boldsymbol{y})\big)dy \qquad (7.13)$$

Here, since the potential function $V_d(\boldsymbol{y})$ has compact support, we have limit the integration to the computational domain Ω_c. Although the explicit form of such kernel is not known, Murata derived its asymptotic form for general elliptic operators with periodic coefficients [57]. Based on their work, the kernel $G(\boldsymbol{x} - \boldsymbol{y}; E_k)$ for outgoing waves in periodic time-harmonic Schrodinger equation, when $|\boldsymbol{x} - \boldsymbol{y}| \to \infty$, will be:

$$G(\boldsymbol{x} - \boldsymbol{y}; E_k) = \frac{\phi_k^*(\boldsymbol{y})\phi_k(\boldsymbol{x})}{|\boldsymbol{x} - \boldsymbol{y}|^{(d-1)/2}}f(\boldsymbol{k})\Big(1 + \mathcal{O}\big(|\boldsymbol{x} - \boldsymbol{y}|^{-1}\big)\Big) \qquad (7.14)$$

where $\phi_k(\boldsymbol{x})$ is the eigenstate of the periodic Schrodinger for wavenumber $\boldsymbol{k}$ and superscript $*$ indicates complex conjugate. Note that since the energy of $\phi_k(\boldsymbol{x})$ is predetermined, this wavenumber can be uniquely calculated. Applying this asymptotic form to equation (7.13) and considering the fact that $\boldsymbol{y}$ is bounded to the limits of integral (Ω_c), we can decouple the $\boldsymbol{x}$ and $\boldsymbol{y}$ variables, and derive the asymptotic form of scattering wave in periodic media in $\mathbb{R}^d$ as:

$$\psi_\infty(\boldsymbol{x}) = \frac{\phi_k(\boldsymbol{x})}{|\boldsymbol{x}|^{(d-1)/2}}g(\boldsymbol{k})\Big(1 + \mathcal{O}\big(|\boldsymbol{x}|^{-1}\big)\Big) \qquad (7.15)$$

This can further be used to find the radiation condition analogous to Sommerfeld radiation condition in homogenous space. For this purpose, one can simply find the relationship between ψ_∞ and its gradient through expression (7.15). As a result, we can construct a Sommerfeld-like radiation condition for scattering wave in periodic

media:

$$\lim_{r\to\infty} r^{(d-1)/2}\Big(\phi_k(\boldsymbol{x})\frac{\partial\psi}{\partial r} - \frac{\partial\phi_k}{\partial r}\psi(\boldsymbol{x})\Big) = 0 \tag{7.16}$$

This radiation condition (7.16) as the first approximation to Dirichlet-to-Neumann non-reflecting boundary condition. Therefore in this paper, we denote it as radiation boundary condition:

$$\nabla\psi \cdot \boldsymbol{n} = \frac{\nabla\phi_k \cdot \boldsymbol{n}}{\phi_k(\boldsymbol{x})}\psi(\boldsymbol{x}) \tag{7.17}$$

However, due to the $\mathcal{O}\big(|\boldsymbol{x}|^{-1}\big)$ error, a very large domain would be needed to compensate for the spurious reflections caused by this boundary condition! We will compare such boundary condition with the other boundary conditions in section (9).

7.3   Exact non-reflecting boundary condition

In order to find the exact absorbing boundary condition, one needs to find either the exact solution on the boundary or the relation between $\psi(\boldsymbol{x})$ and its derivative normal to the boundary, $\nabla\psi \cdot \boldsymbol{n}$. This can be found through the integral form of the equation and the Green's function for periodic Schrodinger's equation, introduced in section (7.2). Unfortunately, there is no explicit expression for such function. However, one can calculate the Green's function, using the eigenstates of the periodic Schrodinger equation:

$$G\big(\boldsymbol{x}, \boldsymbol{y}; E(\boldsymbol{k}_0)\big) = \sum_n \int_{BZ} \frac{\phi_n^*(\boldsymbol{y}, \kappa)\phi_n(\boldsymbol{x}, \kappa)}{E_n(\kappa) - E_n(\boldsymbol{k}_0)} d\kappa \tag{7.18}$$

where $\boldsymbol{k}_0$ is the wave vector of the incident wave and the integration and sum are over the first Brillouin Zone and all of the atomic orbitals, respectively. Note that the integrant is singular around $E_n(\kappa) = E_n(\boldsymbol{k}_0)$. We can overcome this singularity and gain the Green's function for *outgoing* waves, by adding a small imaginary number

to E_κ:

$$G^+\big(\boldsymbol{x}, \boldsymbol{y}; E(\boldsymbol{k}_0)\big) = \lim_{\epsilon \to 0} G\big(\boldsymbol{x}, \boldsymbol{y}; E_k + \imath\epsilon\big) = \sum_n \int_{BZ} \frac{\phi_n^*(\boldsymbol{y}, \kappa)\phi_n(\boldsymbol{x}, \kappa)}{E_n(\kappa) - E_n(\boldsymbol{k}_0) - \imath\epsilon} d\kappa \quad (7.19)$$

As the result, the integral form (7.13) will be:

$$\psi(\boldsymbol{x}) = -\sum_n \int_{BZ} \int_{\boldsymbol{y} \in \Omega_c} \frac{\phi_n(\boldsymbol{x}, \kappa)\phi_n^*(\boldsymbol{y}, \kappa)}{E_n(\kappa) - E_n(\boldsymbol{k}_0) - \imath\epsilon} V_d(\boldsymbol{y})\big(\psi(\boldsymbol{y}) + \phi_k(\boldsymbol{y})\big) dV d\kappa \quad (7.20)$$

Consequently, we can use expression (7.20) to calculate the exact Neumann boundary condition, which is an absolutely non-reflecting boundary condition.

$$\nabla\psi(\boldsymbol{x}) \cdot \boldsymbol{n} = -\sum_n \int_{BZ} \int_{\boldsymbol{y} \in \Omega_c} \frac{\nabla\phi_n(\boldsymbol{x}, \kappa) \cdot \boldsymbol{n}}{E_n(\kappa) - E_n(\boldsymbol{k}_0) - \imath\epsilon} \phi_n^*(\boldsymbol{y}, \kappa) V_d(\boldsymbol{y})\big(\psi(\boldsymbol{y}) + \phi_k(\boldsymbol{y})\big) dy d\kappa$$

$$(7.21)$$

Note that, this expression is not explicit as it depends on the solution, $\psi(\boldsymbol{y})$. However, by implementing the LCAO method, introduced in section 8, the boundary condition converges through a couple of iterations. The main downside of this boundary condition is, the double integral in the expression (7.21), which makes it highly nonlocal and computationally expensive. Even if we consider just one atomic orbital! On the other hand, the singularity and the highly oscillating nature of the integrant, require a large number of quadrature points for calculating the integral over κ. The issues related to resolve this problem are addressed in section 8.

7.4 Perfectly Matched Layers for the Schrodinger's Equation

In this paper, we adopt the complex coordinate stretching approach, originally developed by [21]. For this method we introduce a narrow absorbing layer in the vicinity of the truncated computational boundary Γ_c, as shown in Figure 7.2. Γ_a is the interface between the propagating domain and the absorbing layer.
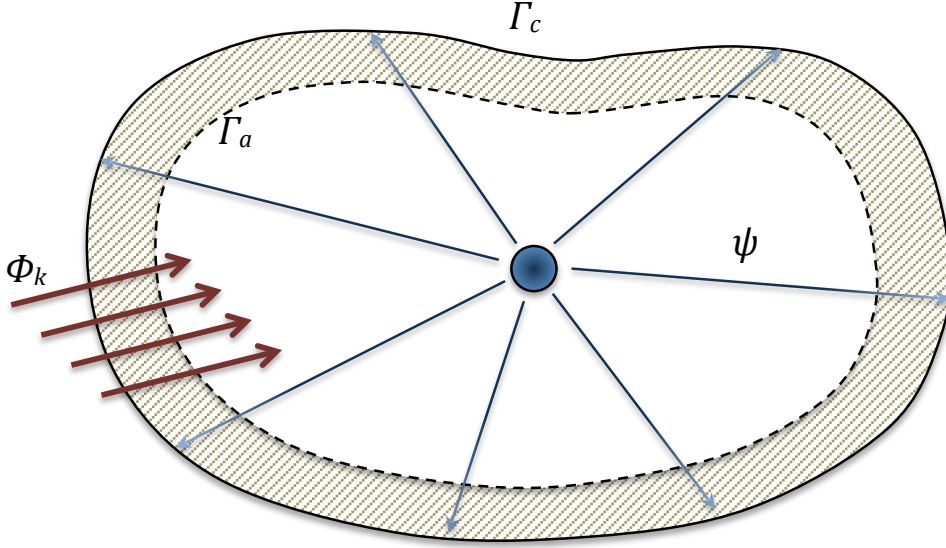
Figure 7.2: Schematic absorbing layer around the boundary Γ_c

The basic idea of PML is to absorb the energy of the traveling waves without causing any reflection, so that when the wave reaches the boundary of the truncated domain, its reflection, if any, will be insignificant. As a result, one can simply apply a zero Dirichlet or Neumann boundary condition on Γ. However, as Oskooi [59] and others pointed out, the Perfectly Matched Layer method fails to be reflectionless in inhomogenous media. Never the less, we will show that one can reduce the reflection, introduced by discretization and periodic media, by increasing the thickness of the absorbing layer.

This absorbing layer can be constructed by stretching the position vector into a complex plane [21]. This will cause the traveling wave to decay exponentially. However, since we are fictitiously changing the distance between the atoms, the potential energy will change as well. As a result, an unwanted reflection between domains is inevitable. All one can hope for, is to reduce this reflection to a negligible point, through a smooth stretching. we define this complex stretching in the following

way:

$$\tilde{x}_i = x_i + \imath\sigma(x) \tag{7.22}$$

where, σ is the *absorption vector function*, which acts like a damping coefficient in elasto-dynamics. We choose this function in such way that it will let the radial waves to attenuate exponentially, while it will have no effects on waves that travel parallel to the boundary. This feature is one of the main differences of the PML method, compared to adiabatic methods, that decay wave in any direction.

In order to maintain the original form of the equation inside the domain, and avoid significant spurious reflections, this absorption function must be zero on the propagation domain. It is conventional to define σ as a smooth function varying from 0 at some point $\boldsymbol{x}_0$ on Γ_a, to σ_0 at $\boldsymbol{x}_1$ on Γ_c [16, 41]. Oskooi et.al. showed that the smoother the absorption function the faster the solution converges as the thickness of the absorbing layer increases. We define the absorption as a real cubic function:

$$\sigma(x) = \sigma_0 \frac{\int_{\boldsymbol{x}_0}^{\boldsymbol{x}} |(\boldsymbol{t}-\boldsymbol{x}_0)|^2|(\boldsymbol{x}_1-\boldsymbol{t})|^2 dt}{\int_{\boldsymbol{x}_0}^{\boldsymbol{x}_1} |(\boldsymbol{t}-\boldsymbol{x}_0)|^2|(\boldsymbol{x}_1-\boldsymbol{t})|^2 dt} \qquad \text{for } \boldsymbol{x} \in \text{absobing layer} \tag{7.23}$$

Note that the increase of the width of absorbing layer makes the transition from the original domain to the absorbing layer smoother. Hence it causes less reflection. As mentioned earlier, the exponential attenuation, caused by the absorbing layer, makes the amplitude of the scattering wavefunction negligible. So one can now apply a zero Dirichlet or Neunamm boundary condition on boundary Γ_c, without causing any extra reflection. After applying zero Neumann boundary condition and mapping the complex stretching back into real coordinate system, the weak-form in equation (7.9) will be:

$$\int_{\Omega_c} \left(\psi^*_{,m} F_{mp}^{-1} \psi_{,n} F_{np}^{-1} + \psi^*(\boldsymbol{x})\big(V_p(\boldsymbol{x}) + V_d(\boldsymbol{x}) - E_k\big)\psi(\boldsymbol{x}) \right) J dv \tag{7.24}$$

$$= -\int_{\Omega_c} \psi^*(\boldsymbol{x})V_d(\boldsymbol{x})\phi_k(\boldsymbol{x}) J dv$$

54

where $F_{ij} = \tilde{x}_{i,j}$ and $J = \det(\boldsymbol{F})$. As we will show in the next section, because of the discretization and the presence of periodic potential, this so called, *Perfectly Matched Layer* will not be perfect anymore. Some, even argue that under such circumstances, PML is not so different from other adiabatic methods [59]. We will test this claim for the periodic Schrodinger equation in section 9.

One big difference between the *Perfectly Matched Layer* and the exact non-reflecting boundary condition is in the rate of the decay of $V_d(\boldsymbol{x})$. According to equation (7.24), the computational domain must contain the compact suport of the defect potential function, V_d. Otherwise, the scattering term, $V_d(\boldsymbol{x})\phi_k(\boldsymbol{x})$, on the right-hand-side of the equation will change and consequently the results will be different from the exact solution. Note that this is not about the reflection of the scattering wave from the boundary, but the correct representation of the scatterer. For the exact non-reflecting boundary condition, however, the defect potential, V_d does not need to be completely contained in the computational domain, as long as this potential decays fast enough. In other words, if the defect potential, V_d, asymptotically decays as $1/r^n$, then the integration of $\boldsymbol{y}$ in equation (7.21) is bounded, if $n \geq d + 1$.

Before closing this chapter, we would like to point out a critical difference between the *PML* method and a regular damping method, where one simply adds an imaginary potential to the Schrodinger equation [37]. As shown in equation (7.24), in *PML* we gradually transform the potential and kinetic terms to the complex plane together, where as in the mentioned damping methods only the potential term changes. This is the physics behind the non-reflecting absorbing layers in free space. Note that those damping methods would cause reflection, even in homogenous spaces.

8

Implementation

8.1   Tight-Binding method for Graphene sheet

8.1.1   Graphene

A single graphene sheet consists of Carbon atoms packed in a two-dimensional hexagonal lattice. Figure 8.1 shows that the graphene sheet is generated from the unit cell by the lattice vectors a_1 and a_2, which make an angle of $\frac{\pi}{3}$:

$$a_1 = \frac{\sqrt{3}a}{2}\hat{x}_1 + \frac{a}{2}\hat{x}_2 \tag{8.1}$$

$$a_2 = \frac{\sqrt{3}a}{2}\hat{x}_1 - \frac{a}{2}\hat{x}_2$$
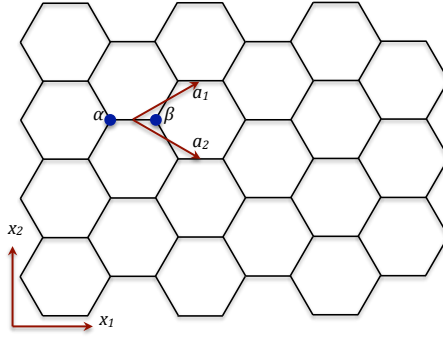
Figure 8.1: A single graphene sheet. The lattice vectors a_1 and a_2 are shown by arrows.

Knowing the lattice vectors a_1 and a_2 and the positions of the two carbon atoms labeled by 1 and 2, X_n, we can construct the whole $2D$ graphene layer as [71]:

$$\boldsymbol{X}_{n,(\zeta_1,\zeta_2)} = \zeta_1 a_1 + \zeta_2 s_2 + \boldsymbol{X}_n, \qquad \text{n=1,2} \tag{8.2}$$

In Tight-Binding method one assumes that the valence electrons are "tightly bound" to the atoms and the electronic orbitals are not strongly altered during the bonding process. TB is arguably the simplest method that we can devise while still claiming that we are doing quantum mechanics [66].

8.1.2   LCAO

In order to numerically implement the weak-form, presented in (7.9) and (7.24), we adopt the *Linear Combination of Atomic Orbitals* method or in short LCAO method to present the scatter wavefunction, $\psi(\boldsymbol{x})$ [15, 28]:

$$\psi(\boldsymbol{x}) = \sum_i \sum_\alpha a_{i\alpha} \Phi_\alpha(\boldsymbol{x} - \boldsymbol{X}_i) \tag{8.3}$$

This is the essential idea in Tight-Binding method. Here $\Phi_\alpha(\boldsymbol{x} - \boldsymbol{X}_i)$ is a set of localized bases to simulate the atomic orbitals, α at each atomic site, $\boldsymbol{X}_i$. In this thesis, we have used self-consistent molecular-orbitals for Carbon [67].

57

For a periodic system, however, the LCAO expression must satisfy the *Bloch theorem*, which states that the type of wavefunction for a particle in a periodically-repeating environment, like an electron in a crystal is of the following form [54]:

$$\phi(\boldsymbol{x}, \boldsymbol{k}) = e^{i\boldsymbol{k} \cdot \boldsymbol{x}} u(\boldsymbol{x}, \boldsymbol{k}) \tag{8.4}$$

where, $\boldsymbol{k}$ is the wave number and $u(\boldsymbol{x}, bf)$ is a periodic function. Such form can be conceived by LCAO, through the following summation over localized orbitals, which is known as Bloch Sum:

$$\Phi(\boldsymbol{x}, \boldsymbol{k}) = \sum_{i} \sum_{\alpha}^{2} c_{\alpha} e^{i\boldsymbol{k} \cdot \boldsymbol{X}_i} \Phi_{\alpha}(\boldsymbol{x} - \boldsymbol{X}_i) \tag{8.5}$$

The first sum is over cells, the ith of which is specified by the Bravais lattice vector $\boldsymbol{X}_i$, while the second sum is over the set of orbitals α which are assumed to be centered on each site and participating in the formation of the solid. In case of Graphene, where there are two atoms pre unit cell (8.5) we are required to introduce an additional index in (8.5) and an attendant sum over the atoms within the unit cell.
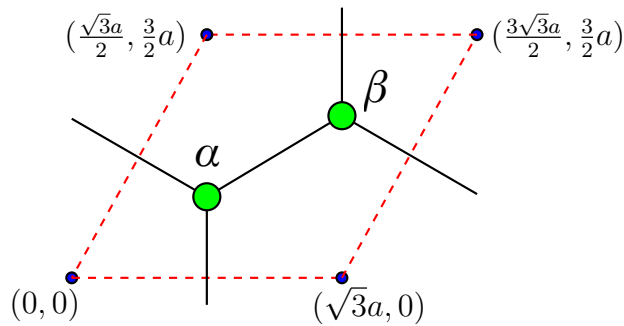

Figure 8.2: A unit cell of Graphene sheet with Lattice constant $\sqrt{3}a$, and $a = 1.42\text{Å}$. Each unit cell contains two atoms (The Green nodes are atoms.)

58

8.1.3 The Hamiltonian and overlap matrices

The goal of TB is to solve the single-particle Schrodinger equation approximately. Going back to the Schrodinger equation (7.4) and using (8.5) by taking into account only the contribution of the orbital π, we consider the LCAO representation

$$\phi(\boldsymbol{x}, \boldsymbol{k}) = c_\alpha \Phi_\alpha(\boldsymbol{x}, \boldsymbol{k}) + c_\beta \Phi_\beta(\boldsymbol{x}, \boldsymbol{k}) \tag{8.6}$$

Then the eigenvalue problem corresponding to each wave number $\boldsymbol{k}$ for a single electron is given by

$$\sum_i h^i_{\alpha\beta} e^{i\boldsymbol{k}\cdot\boldsymbol{X}_i} c_{k\beta} = E(\boldsymbol{k}) \sum_i s^i_{\alpha\beta} e^{i\boldsymbol{k}\cdot\boldsymbol{X}_i} c_{k\beta} \tag{8.7}$$

where $E(\boldsymbol{k})$ is the eigenvalue of the wavefunction and $h_{\alpha\beta}$, $s_{\alpha\beta}$ are the components of the Hamiltonian and Overlap matrices, respectively.

$$h^i_{\alpha\beta} = \int_\Omega -\frac{1}{2}\nabla^2 \Phi^*_\alpha(\boldsymbol{x}-\boldsymbol{X}_0)\Phi_\beta(\boldsymbol{x}-\boldsymbol{X}_i) + \Phi^*_\alpha(\boldsymbol{x}-\boldsymbol{X}_0)V_p(\boldsymbol{x})\Phi_\beta(\boldsymbol{x}-\boldsymbol{X}_i)dx \tag{8.8}$$

$$s^i_{\alpha\beta} = \int_\Omega \Phi^*_\alpha(\boldsymbol{x}-\boldsymbol{X}_0)\Phi_\beta(\boldsymbol{x}-\boldsymbol{X}_i)dx$$

If V_p was given as an analytic function, then Integrals above are called *two-center* integrals when $\alpha \neq \beta$ and *one-center* or *on-site* integrals if $\alpha = \beta$. However, another assumption that is made in TB is to write $V_p(\boldsymbol{x})$ as a sum of atom-centered potentials $V_\gamma(\boldsymbol{x}-\boldsymbol{X}_\gamma)$, each of which is independent of all the other atoms in the system:

$$V_p(\boldsymbol{x}) = \sum_\gamma V_\gamma(\boldsymbol{x}-\boldsymbol{X}_\gamma)$$

This assumption introduces the *three-center* integrals for the second term in $h^i_{\alpha\beta}$, where α, β and γ are different. As we saw, the two-center terms are straightforward because they only depend on the relative positions of the two atoms and independent of their environment. The three-center terms, however, present another problem,

since it will be difficult to devise a scheme to parameterize them in terms of atomic positions. Instead, it is usually assumed that all three-center integrals are zero [66]. In this thesis, the periodic potential, V_p is calculated based on [55].

On the other had, since $\Phi(\boldsymbol{x} - \boldsymbol{X}_i)$ are highly localized orbitals, usually only the nearest neighbors of an atom are to be considered. We have considered 12 nearest neighbors as show in Figure 8.3.
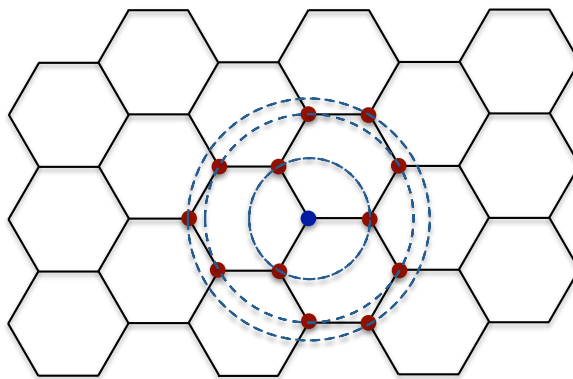
Figure 8.3: The 12 nearest neighbors for the blue atom in a Graphene sheet.

Although this seem to make the calculations very expensive, compared to the usual three nearest neighbor assumptions, note that one needs to calculate these integrations only once. That's the big advantage of TB method. Note that the number of considered neighboring atoms depend on the atomic orbitals that one uses in their TB method. For instance in case of Graphene sheet, the convergence of h_{11} is shown in Figure 8.4.
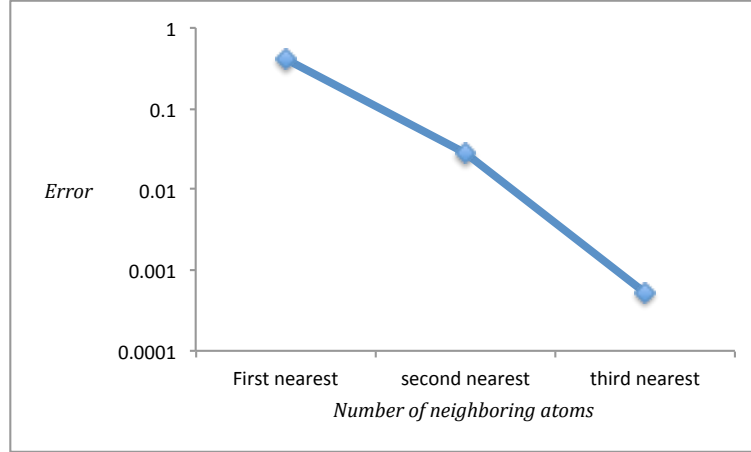
Figure 8.4: Convergence of h_{11} as the number of the ring of the neighboring atoms increases.

The dispersion relation between **k** and the energy of the wavefunction, E in Graphene sheet is plotted for the first Brillouin zone in figure (Figure 8.5).
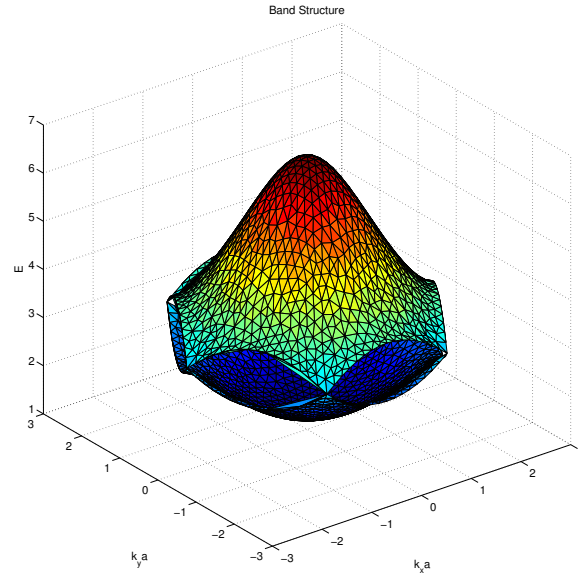
Figure 8.5: The band structure of a monolayer Graphene sheet for the first two bands.

8.2 Implementation of exact boundary condition for Graphene

As mentioned in the previous chapter, the exact boundary condition (7.21) is highly nonlocal. This expression for a 2-dimensional case like Graphene sheet requires an integration over a confined 2-dimensional area around the scatterer, an integration over the Brillouin zone, which is shown for the Graphene sheet in Figure 8.6 and a sum over the two sub lattices for every point $\boldsymbol{x}$ on the boundary of the computational domain.
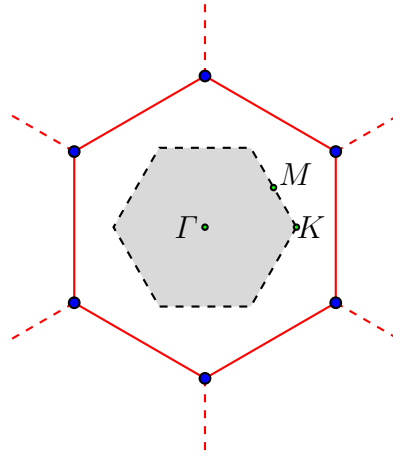
Figure 8.6: First Brillouin zone of graphene with atomic distance a

Moreover, the nature of the integrant in expression (7.18) is highly oscillating and it has a singularity at $E(\kappa) = E(\boldsymbol{k}_0)$ (note that $|\boldsymbol{x}|$ is usually large on the boundaries). Thus it requires a great deal of integration points to calculate the Green's functions accurately.

In order to overcome these computational problems we have gone through the following steps:

- The Green's function, proposed in (7.18) is a *separable kernel*. In other words, one can write the Green's function as

$$G(\boldsymbol{x}, \boldsymbol{y}) = \sum_{\kappa} f(\boldsymbol{x}) g(\boldsymbol{y})$$

62

This is a very helpful computational feature, which helps us to calculate and store the y-integral once for all $\boldsymbol{x}$ points.

- As shown in (7.19) we replace the original Green's function with $G^+\big(\boldsymbol{x}, \boldsymbol{y}; E(\boldsymbol{k}_0)\big)$ to avoid the singularity of the integrand. Not only this step does not affect the accuracy, but also is necessary to extract the Green's function corresponding to purely outgoing waves.

- An effective recipe for numerical integration of such highly oscillating function is Filon's method [38]. In this method, we simply use the following approximation:

$$\int f(x)e^{\iota\omega x}dx \approx \sum_j \int c_j x^j e^{\iota\omega x}dx$$

- The energy band(s) that include energy $E(\boldsymbol{k}_0)$ are dominant in the calculation of (7.19). For instance in Figure 8.5, if $E(\boldsymbol{k}_0)$ belongs to he lower band, we can neglect the higher band from the integration, unless the energy of the incident wave is very close to point K (where the two bands join).

After considering these steps, an efficient and close approximation of (7.21) is given by

$$\nabla\psi(\boldsymbol{x}) \cdot \boldsymbol{n} \approx \int_{BZ} \frac{\nabla\phi_{n0}(\boldsymbol{x}, \kappa) \cdot \boldsymbol{n}}{E_{n0}(\kappa) - E_{n0}(\boldsymbol{k}_0) - \iota\epsilon} \mathcal{G}(\kappa)d\kappa \qquad (8.9)$$

where $\mathcal{G}(\kappa) = \int_{\boldsymbol{y}\in\Omega_c} \phi_n^*(\boldsymbol{y}, \kappa)V_d(\boldsymbol{y})\big(\psi(\boldsymbol{y}) + \phi_k(\boldsymbol{y})\big)dy$ and $n0$ is the band that $E_{\boldsymbol{k}_0}$ belongs to. We will show the results of this approximation and its comparison with PML method in the next chapter.

Despite this the fact that this approximation saves a great deal of computation efforts, (8.9) is still a nonlocal expression and the two-dimensional nature of the problem, makes this approximation computationally expensive, compared to the

PML method. This non locality can be treated, using the Bloch sum introduced in (8.5).

$$\nabla\psi(\boldsymbol{x})\cdot\boldsymbol{n} \approx \sum_i \nabla\Phi(\boldsymbol{x}-\boldsymbol{X}_i)\cdot\boldsymbol{n} \int_{BZ} \frac{e^{i\boldsymbol{k}\cdot\boldsymbol{X}_i}\mathcal{G}(\kappa)}{E_{n0}(\kappa) - E_{n0}(\boldsymbol{k}_0) - \iota\epsilon} d\kappa = \sum_i \nabla\Phi(\boldsymbol{x}-\boldsymbol{X}_i)\cdot\boldsymbol{n}C_i$$

(8.10)

where the right hand-side of (8.10) is just a summation over nearest neighbors at each point $\boldsymbol{x}$. Vector C_i is as large as the number of atoms on the boundary and can be calculated once for all of the $\boldsymbol{x}$ point on the boundary. Moreover, one can significantly reduce the size of vector C_i, by converting the second order PDE (7.8) into a nonlinear, but first order PDE as follow:

$$\nabla \cdot \boldsymbol{f} + \boldsymbol{f} \cdot \boldsymbol{f} = V(\boldsymbol{x}) - E_k \tag{8.11}$$

$$\boldsymbol{f} = \frac{\nabla\psi}{\psi} \text{ over } \Gamma_{in}$$

where, $\boldsymbol{f}$ is a replacement for $\frac{\nabla\psi}{\psi}$. Note that, since (8.11) is a first-order PDE, it only needs essential boundary condition on Γ_{in} and no boundary condition on Γ_{out}! (Figure 8.7)
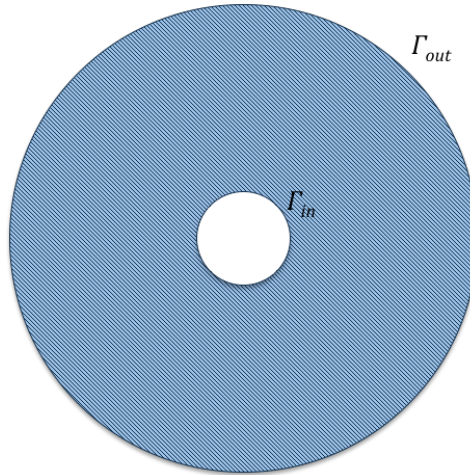
Figure 8.7: A schematic domain for $\boldsymbol{f}$

64

This phenomenon, helps to find the exact boundary condition on the outer boundary, Γ_{out}, just by applying the approximate non-local NRBC on a small region, Γ_{in}. Theoretically, the inner boundary can be any shape and any size, but the smaller it gets, the longer it take for equation (8.11) to converge.

8.3 Development of symmetry-adapted Tight-Binding method for Carbon nanotubes

8.3.1 Structure of single-walled Carbon nanotube

Single-walled Carbon nanotubes ($SWCNT$) consist of a Graphene sheet, folded on itself. Such structure provides a couple of important symmetries that we will explain in this section.

Translational Symmetry

The fundamental property of an infinitely long SWNT is its translational periodicity. When matching a SWCNT with the corresponding Graphene sheet, the circumference of SWCNT corresponds to the width of the Graphene. This width is known as the *chiral vector C_h*. When decomposed along the a_1 and a_2 vectors, the chiral vector is given by

$$C_h = ma_1 + na_2$$

where, (m, n) is a pair of integers, which conveniently label a SWCNT. For example Figure 8.8 shows a $(3, 3)$ SWCNT on its unfolded Graphene sheet. The length of chiral vector, which is π multiplied by the diameter of the SWCNT is easily related to the m and n:

$$|C_h| = a\sqrt{m^2 + n^2 + mn}$$
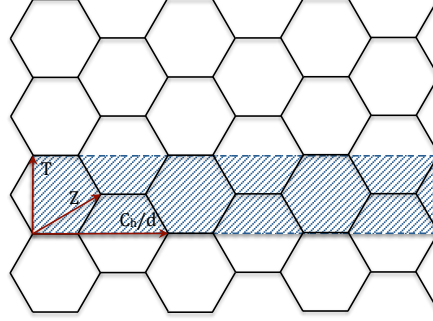
Figure 8.8: Unit cell of $(3,3)$ Carbon nanotube. T, Z, and C_h/d are translational, helical and chiral vectors, respectively. where $d = GCD(m, n)$

Moreover, one can define the translational vector as a vector starting from one hexagon and ending at another equivalent one in the direction perpendicular to the chiral vector, C_h, as shown in Figure 8.8 for the $(3, 3)$ SWCNT. Mathematically, it can be easily obtained that:

$$\boldsymbol{T} = t_1 a_1 + t_2 a_2$$

where

$$t_1 = \frac{2n + m}{GCD(2n + m, 2m + n)} \qquad t_2 = -\frac{2m + n}{GCD(2n + m, 2m + n)}$$

The function $GCD(i, j)$ denotes the greatest common divisor of the two integers i and j. The rectangle area confined by chiral vector Ch and the translational vector $\boldsymbol{T}$ corresponds the translational unit cell of the SWCNT (see Figure 8.8). The number of carbon atoms in the translational unit cell, N_0, is calculated by dividing this area by the area of unit cell of graphene.

$$N_0 = \frac{4(m^2 + n^2 + mn)}{GCD(2n + m, 2m + n)}$$

For instance, $(3, 3)$ SWCNT in Figure 8.8 has 12 atoms in its translational unit cell. Note that if $GCD(2n + m, 2m + n) = 1$ the number of atoms per unit cell could increase dramatically. For example, the translational unit cell of $(9, 5)$ SWCNT has 604 atoms.

Knowing the translational vector $\boldsymbol{T}$ and the position of the N_0 in the translational cell, X_n, the infinite nanotube structure can be described as:

$$\boldsymbol{X}_{n,\zeta} = \zeta\boldsymbol{T} + \boldsymbol{X}_n \quad n = 1, ..., N_0$$

where integer ζ labels the various replicas of the initial translational cell containing the N_0 atoms.

Helical Symmetry

The vectors Ch/d and $\boldsymbol{T}$ define the pure rotational and translational symmetries, respectively (Figure 8.8). Additionally, SWCNT has helical symmetry described by the helical vector comprised of both rotational and translational components. Exploiting this symmetry is central for the proposed work. To describe a SWCNT, the choice for the screw operation, the vector $\boldsymbol{Z}$ in Figure 8.8, is not unique. We choose $\boldsymbol{Z}$ in such a way that it has the smallest component in the axial direction of the SWNT:

$$\boldsymbol{Z} = v1a_1 + v_2a_2$$

where

$$l_2v_1 - l_1v_2 = GCD(l_1, l_2)$$

$$0 < t_1v_2 - t_2v_1 < N_0/GCD(l_1, l_2)$$

using this symmetry, one can now redefine the unit cell of SWCNT with only two atoms for any m and n as in [6]:

$$X_{\boldsymbol{i},k} = X_{(i_1,i_2),k} = \boldsymbol{Q_i}\boldsymbol{X_{0,k}} + \boldsymbol{c_i}$$

and we have that

$$\boldsymbol{Q_i} = \bar{\boldsymbol{Q}}_1^{i_1}\bar{\boldsymbol{Q}}_2^{i_2}, \quad \boldsymbol{c_i} = \sum_{p=0}^{p=i_1-1} \bar{\boldsymbol{Q}}_1^p\bar{\boldsymbol{c}}_1$$

That calculations regarding to the rotation matrices $\bar{\boldsymbol{Q}}_1$, $\bar{\boldsymbol{Q}}_2$ and $\bar{\boldsymbol{c}}_1$ can be found in the appendix of [6].

8.3.2 Formulation of Tight-Binding for SWCNT

The electronic band structure of carbon nanotubes is usually obtained by zone-folding of the tight-binding band structure of graphene. In that case the Bloch sum for nanotubes will be

$$\phi(\boldsymbol{x}, \boldsymbol{k}) = \sum_{\zeta} \sum_{\alpha} \sum_{\beta}^{N_0} c_{\alpha\beta} e^{i\boldsymbol{k}\cdot\boldsymbol{T}\zeta} \Phi_\alpha(\boldsymbol{x} - \boldsymbol{T}\zeta)$$

where $\boldsymbol{T}$ is the translation vector and N_0 is the number of atoms in one unit cell Figure 8.8.

The number of atoms in a unit cell can increase significantly, as the pain of integers (m, n) increase. However, by using *translational, chiral and helical* symmetries for nanotubes, one can reduce the number of atoms per unit cell to two, for any chirality [71]. The symmetry-adapted Bloch sum in symmetry-adapted nanotubes is given by

$$\phi_\ell(\boldsymbol{x}, k) = \sum_{\zeta_1=0}^{N_s-1} \sum_{\zeta_2=0}^{N_a-1} \sum_{\alpha} c_\alpha e^{i\ell(\theta_1\zeta_1+\theta_2\zeta_2)+ik\zeta_1} \Phi_\alpha(\boldsymbol{x}, \zeta_1, \zeta_2) \tag{8.12}$$

Here, $\ell = 0, 1, ..., N_0/2 - 1$ is the angular number and as before, α runs over all orbitals and sub-lattices. Using this representation for Bloch waves and considering only the π orbital, the eigenvalue problem corresponding to the electronic structure of Carbon nanotube is given by

$$\sum_{\zeta_1,\zeta_2} h_{ab}^{\zeta_1,\zeta_2} e^{i\ell(\theta_1\zeta_1+\theta_2\zeta_2)+ik\zeta_1} c_b = E(k\ell) \sum_{\zeta_1,\zeta_2} s_{ab}^{\zeta_1,\zeta_2} e^{i\ell(\theta_1\zeta_1+\theta_2\zeta_2)+ik\zeta_1} c_b \tag{8.13}$$

This set of eigenvalue problem will give us two set of eigenvalues and eigenstates for every ℓ. As a result, instead of solving an $N_0 \times N_0$ set of matrices, we solve $N_0/2$ set of 2×2 equations.

8.4 Implementation of exact boundary condition for Carbon nanotubes

The approximation of expression (**??**) for symmetry-adapted Carbon nanotube is the same as what we shown in section (8.2) for 2-dimensional Graphene sheet, except the fact that it is now a 1-dimensional integration over the k-space. So the approximation (8.10) will be

$$\nabla \psi(\boldsymbol{x}) \cdot \boldsymbol{n} \approx \sum_{\zeta_1,\zeta_2} \nabla \Phi(\boldsymbol{x},\zeta_1,\zeta_2) \cdot \boldsymbol{n} \sum_{\ell=0}^{N_0/2-1} \int_{-\pi/T}^{\pi/T} \frac{c_{\kappa\ell} e^{\imath\ell(\theta_1\zeta_1+\theta_2\zeta_2)+\imath\kappa\zeta_1} g(\boldsymbol{y},\kappa)}{E_{n0}(\kappa,\ell) - E_{n0}(\boldsymbol{k}_0,\ell_0) - \imath\epsilon} d\kappa \quad (8.14)$$

Since Nanotube is a quasi one-dimensional structure, calculation of this expression will not the computationally expensive. On the other hand, using a first order PDE, like (8.11) will not help to reduce the computation effort.

8.5 Development of Tight-Binding model for DNA

DNA is a macro-molecule that contains repeated stacks of bases formed by either Adenine-Thymine (AT) or Cytoine-Guanine (CG) pairs coupled via hydrogen bonds and held in the double-helix structure by a sugar-phosphate backbone.

We follow the fishbone model, shown in Figure 8.9, has one central conduction channel in which individual sites represent a basepair; these are interconnected and further linked to upper and lower sites, representing the backbone, but are not interconnected along the backbone. Every link between sites implies the presence of a hopping amplitude. The Hamiltonian for the fishbone model H_F is given by

$$H_F = \sum_i \sum_{q=\uparrow,\downarrow} h_{bb}^{i,i+1} + h_{bb}^{i,i} + h_{sb}^{i,q} + h_{ss}^{i,q} \quad (8.15)$$

where the subscript b represents base pairs and s represents sugar backbones. Also,the sum over i covers the atoms along the axis of the molecule, while the sum over q

belongs to the lower and upper backbones. The distance between each base pair is assumed to be $0.34nm$.
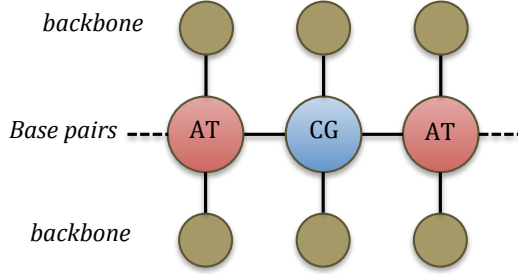
Figure 8.9: The fishbone model of DNA for equation (8.15)

Considering the model in Figure 8.9, the components of the Hamiltonian matrix in (8.15) are given by:

$$h_{bb}^{i,i+1} = \int_\Omega \frac{1}{2}\nabla\Phi_\alpha^*(\boldsymbol{x} - \boldsymbol{X}_i) \cdot \nabla\Phi_\beta(\boldsymbol{x} - \boldsymbol{X}_{i+1}) + \Phi_\alpha^*(\boldsymbol{x} - \boldsymbol{X}_i)V_{\alpha\beta}(\boldsymbol{x})\Phi_\beta(\boldsymbol{x} - \boldsymbol{X}_{i+1})dx$$

$$(8.16)$$

$$h_{bb}^{i,i} = \int_\Omega \frac{1}{2}\nabla\Phi_\alpha^*(\boldsymbol{x} - \boldsymbol{X}_i) \cdot \nabla\Phi_\alpha(\boldsymbol{x} - \boldsymbol{X}_i) + \Phi_\alpha^*(\boldsymbol{x} - \boldsymbol{X}_i)V_{\alpha\alpha}(\boldsymbol{x})\Phi_\alpha(\boldsymbol{x} - \boldsymbol{X}_i)dx$$

$$h_{sb}^{i,q} = \int_\Omega \frac{1}{2}\nabla\Phi_\alpha^*(\boldsymbol{x} - \boldsymbol{X}_i) \cdot \nabla\Phi_\gamma(\boldsymbol{x} - \boldsymbol{X}_i) + \Phi_\alpha^*(\boldsymbol{x} - \boldsymbol{X}_i)V_{\alpha\gamma}(\boldsymbol{x})\Phi_\gamma(\boldsymbol{x} - \boldsymbol{X}_i)dx$$

$$h_{ss}^{i,q} = \int_\Omega \frac{1}{2}\nabla\Phi_\gamma^*(\boldsymbol{x} - \boldsymbol{X}_i) \cdot \nabla\Phi_\gamma(\boldsymbol{x} - \boldsymbol{X}_i) + \Phi_\gamma^*(\boldsymbol{x} - \boldsymbol{X}_i)V_{\gamma\gamma}(\boldsymbol{x})\Phi_\gamma(\boldsymbol{x} - \boldsymbol{X}_i)dx$$

where α and β switch between AT and CG base pairs and γ represents the sugar backbone. For the parameterization of the Hamiltonian matrix we have followed [36].

9

Results

In this section we implement the PML and exact methods developed in the previous chapters and on a monolayer Graphene sheet and single-wall Carbon nano-tube. In these examples we add one or more local defects to the structure as vacancies to study the scattering waves and the influence of boundary condition on them. Moreover, we will study the electronic behavior of Y-junction Carbon nano-tubes with different chiralities.

9.1   Mono-layer Graphene with a single vacancy

For the first example, we consider a monolayer Graphene sheet that is missing one atom in the center, subjected to an incident Bloch wave $\phi(\boldsymbol{x}, \boldsymbol{k})$ with wavenumber $\boldsymbol{k} = 0.42e_x + 0.49e_y$. Figure 9.1 shows the density field $\rho(\boldsymbol{x}) = \Phi^*(\boldsymbol{x})\Phi(\boldsymbol{x})$, corresponding to the PML method. Note that the point defect at the center of the domain plays the role of an obstacle for the Bloch wave $\phi(\boldsymbol{x}, \boldsymbol{k})$. Note that the Graphene may not be at rest after considering the vacancy, however we just merely interested in studying the behavior of the boundary conditions at this point.

(a) Scattering wave

(b) Total wavefunction
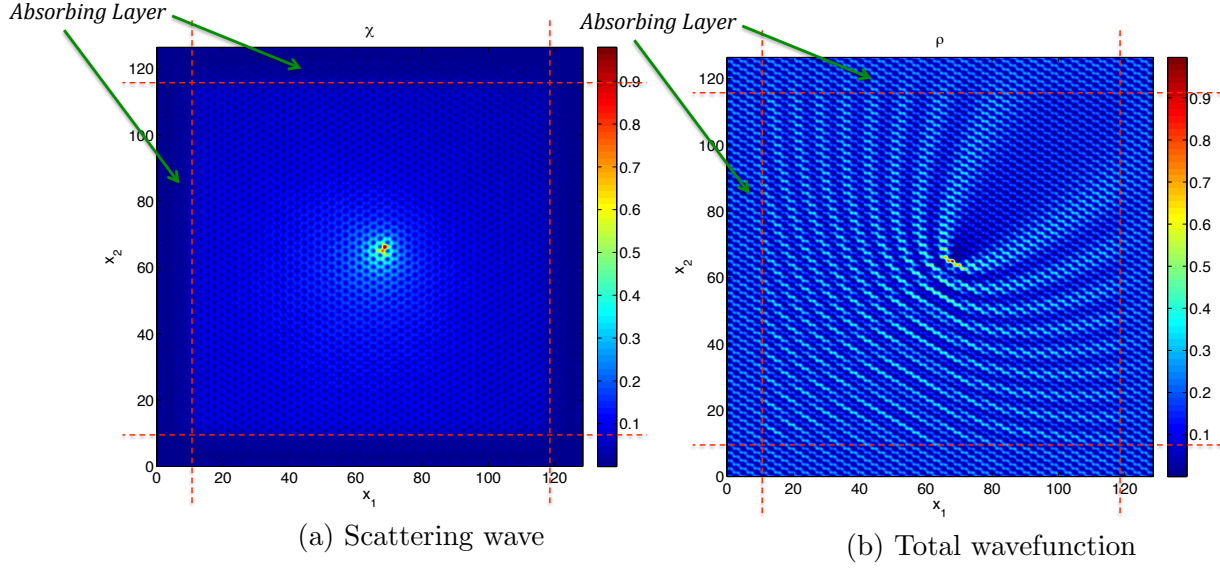
Figure 9.1: The density function of Graphene with a single defect, subjected to Bloch wave $\phi_k(\boldsymbol{x})$ with wavenumber $\boldsymbol{k} = 0.42e_x + 0.49e_y$.

As expected from equation (7.15), the norm of the scattering wave, $\psi(\boldsymbol{x})\psi(\boldsymbol{x})$, shown in Figure 9.2 decays as $1/r$ away from the defect, till it reaches the absorbing layer. From that point it decays exponentially and completely vanishes before reaching the boundary of the computational domain. As a result, we will not see the influence of the boundary condition on the scattering wave.
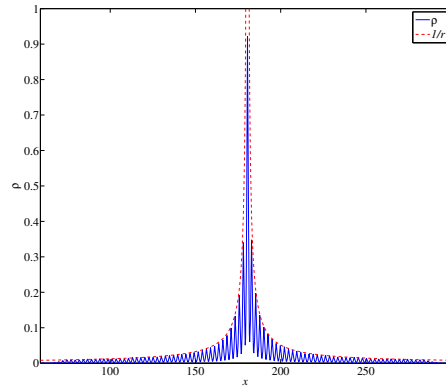
Figure 9.2: Profile of scattering wave density for a constant x_2, compared to $1/r$ profile. The effect of absorbing layer can be seen at the both ends.

In order to evaluate the convergence of the PML method for this example, we point out the important fact that, the sole purpose of absorbing boundary conditions like PML, is to be transparent for the outgoing waves. As a result, for an exact boundary condition, changing the computational domain does not change the results, as long as the domain contains the defect potential, $V_d(\boldsymbol{x})$. This fact inspires us to consider the convergence of the solution of the PML method when we move the domain, (or from another point of view, the defects inside the domain) as shown in Figure 9.3. We evaluate the error in the following way:

$$E = \frac{|\rho(\boldsymbol{x}) - \rho(\boldsymbol{x}')|^2}{\rho(\boldsymbol{x})^2}$$
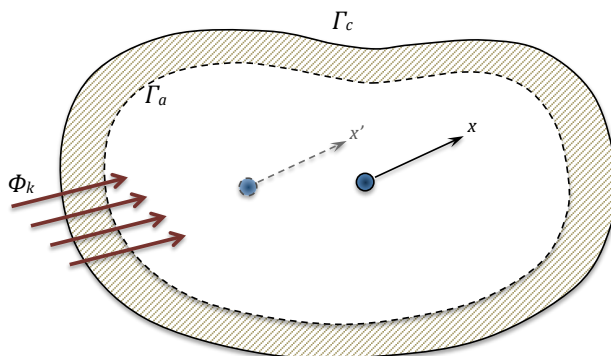
Figure 9.3: The density of wave function, ρ at point X must not change as the defect moves.

Running the set of simulations for different layer thicknesses, shows a satisfactory convergence for the PML method. Figure 9.4 shows this convergence for two difference incident waves. This investigation, shows that the accuracy of the PML method improves as the norm of the wavenumber increases. The fact that PML shows good convergence for higher wave numbers is very important, considering the fact that most existing non-reflecting boundary conditions rapidly lose their accuracy as the wavenumber increases, e.g. [25].
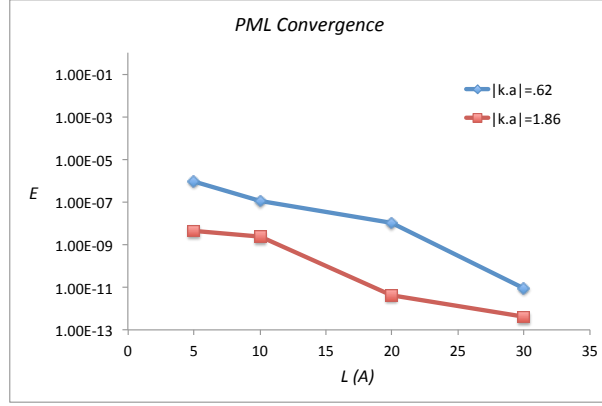
Figure 9.4: Convergence of the results of the PML method, as the thickness of the layer increases.

Now, we consider the same example and apply the exact DtN boundary condition we derived in (8.2). Figure 9.5 shows the density of the total wavefunction with the same incident wave. Note that the application of exact boundary condition was about 20 times slower than the PML method.
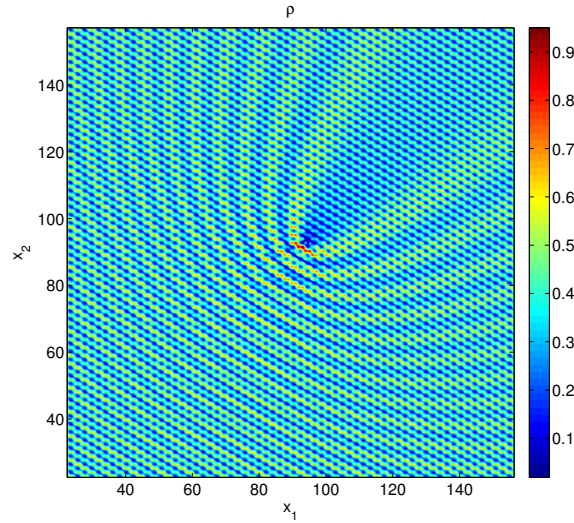
Figure 9.5: The exact DtN boundary condition applied to a Graphene sheet with a vacancy at the center of the domain. The incident wave has the wave vector of $\boldsymbol{k} = 0.42e_x + 0.49e_y$.

Figure 9.6 shows the comparison of the exact and PML method. A very close match between the results can be seen, which indicates that the PML method does indeed converge to the exact solution.
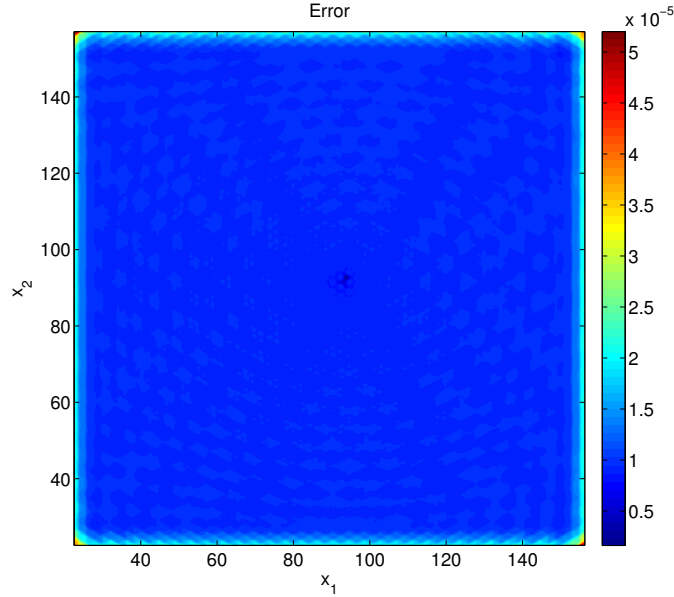
(a) Error for $\boldsymbol{k} = 0.42e_x + 0.49e_y$
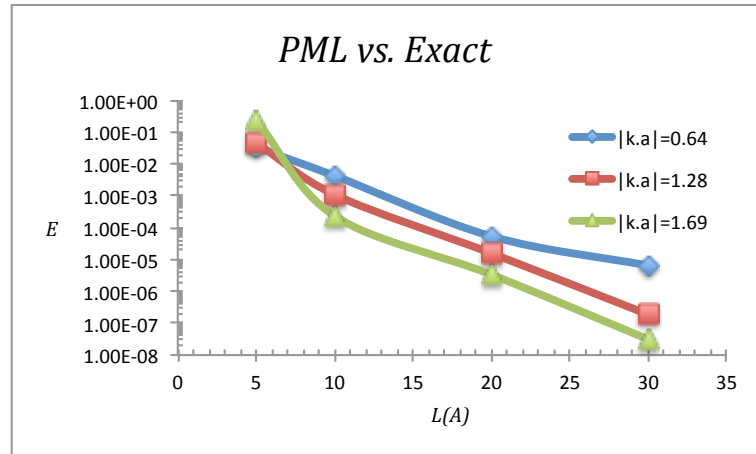
(b) Maximum error for various wavenumber

Figure 9.6: The error analysis for PML and exact methods. (a) shows the point-wise relative error for the wave vector $\boldsymbol{k} = 0.42e_x + 0.49e_y$, while (b) shows the maximum relative error for various wave vectors.

Before ending this section, we pay attention to a very special case, where the energy of the incident wave, is very close to *fermi level*. The electronic behavior of Graphene at such level is related to Klein paradox. This phenomenon usually refers to a counterintuitive relativistic process in which an incoming electron starts penetrating through a potential barrier. In this case, the transmission probability T depends only weakly on barrier height, approaching perfect transparency for very high barriers, which is in contrast with conventional, nonrelativistic tunneling [40].
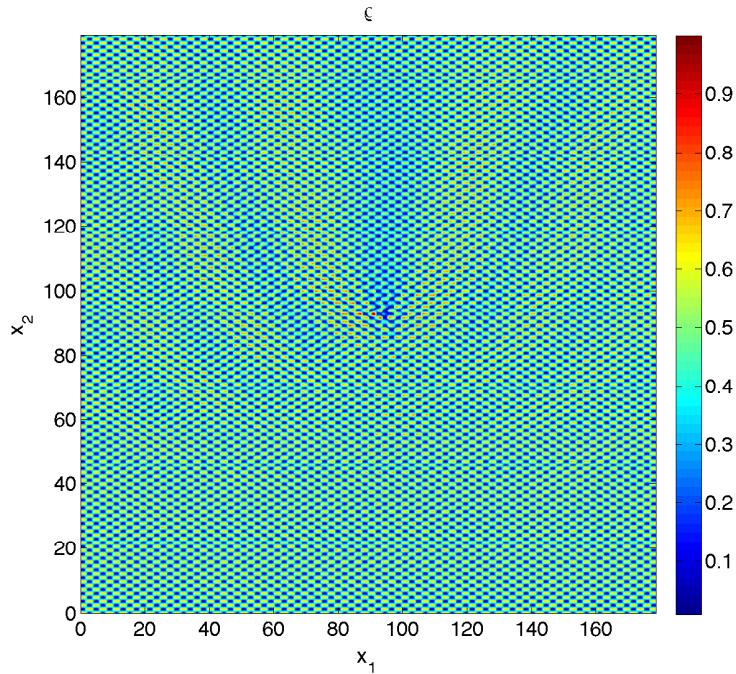
Figure 9.7: The density of the total wavefunction $\phi(\boldsymbol{x})$, for $\boldsymbol{k} = (0, 1.71)$.

In this example, the wavefunction is barely influenced by the defect. Figure 9.7 shows the contour, corresponding to the density of the total wavefunction. This behavior can be justified, by considering the band structure of Graphene, which is shown in Figure 8.5. As it can be seen in this figure, the wave can only scatter in six specific directions, while all the other directions correspond to band-gap. As a

result, the wavefuction *mainly* remains in the same direction of the incident wave.

9.2 Single-walled Carbon nanotube with a single vacancy

For the next series of examples, we consider single walled Carbon nanotubes. As shown the previous chapter, we use the summery groups of this structure to provide a unit cell with only two atoms. Using these symmetries, it is easy to see that nanotubes are quasi one-dimensional objects, since the wave vector $\boldsymbol{k}$ decomposes into a scalar κ that indicates the wavelength along the axis of nanotube, and an angular index, ℓ that differentiates the same wavelengths for different but discrete angles (equation (8.12)). Figure 9.8 shows the band structure, corresponding to an Armchair Carbon nanotube with the chirality of $(5, 5)$. Note that each pair of bands correspond to a specific angular index ℓ.
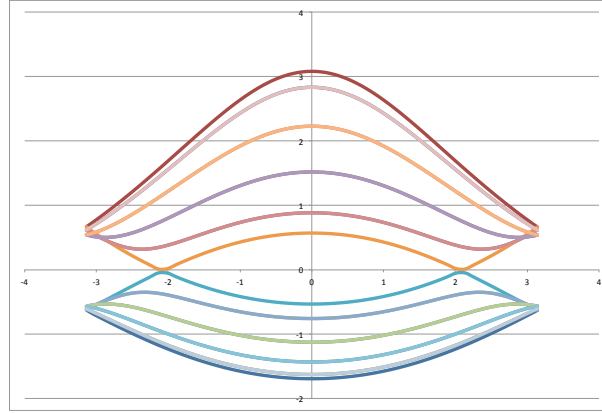
Figure 9.8: The band structure corresponding to $(5, 5)$ Armchair Carbon nanotube. Armchair nanotubes are considered Metallic, since the is no energy gap in their band structure.

Note that Zigzag nanotubes like this are called Metallic nanotubes, since there is no band gap in their band structure.

Now, we consider a vacancy in this nanotube and apply PML and exact methods. Figure 9.9 shows a perfect match for the contour of the scattering waves for these

two methods. Since the wave scatters in a quasi one-dimensional domain, unlike the example for the Graphene sheet, the amplitude of the wave does not decay outside of the defective region.

(a) PML (b) Exact
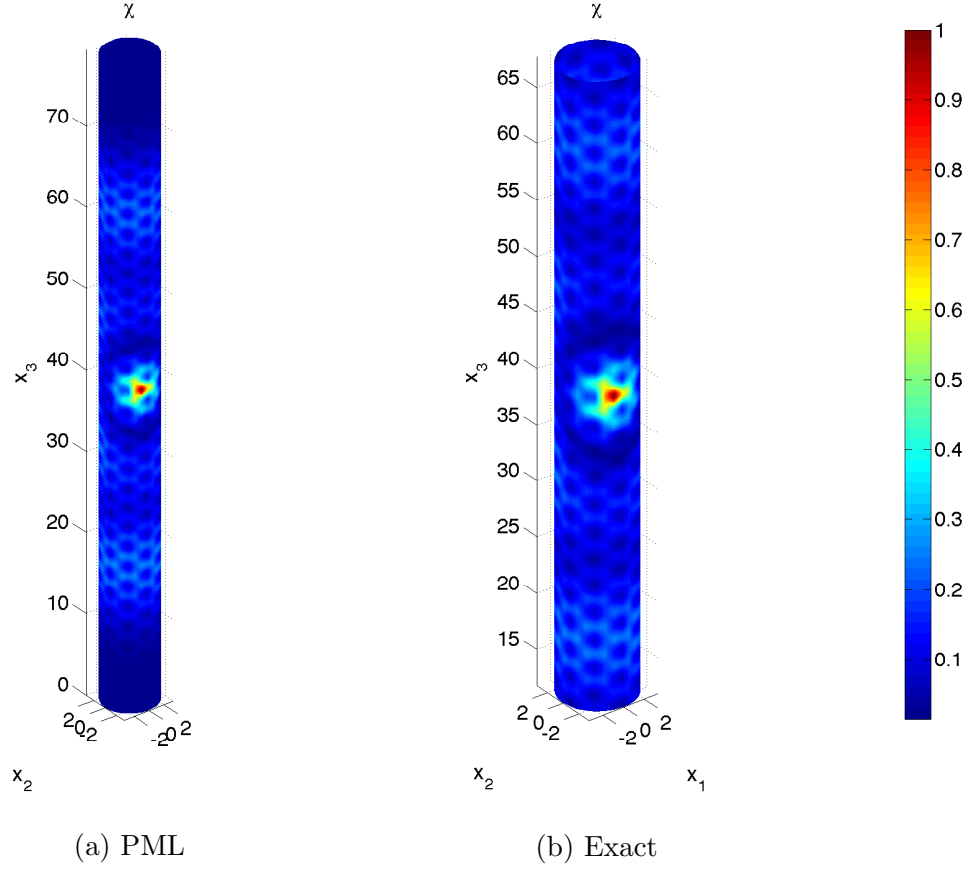
Figure 9.9: Contour of the scattering waves for $(5,5)$ Carbon nanotube with incident wavenumber $\kappa = 0.24$ and $\ell = 0$

The comparison between the exact boundary condition and the PML method is shown in Figure 9.10. The maximum relative error is plotted for different absorption layers for $(5,5)$ Carbon nanotube. One can see that by increasing the wavenumber, the rate of convergence increases.
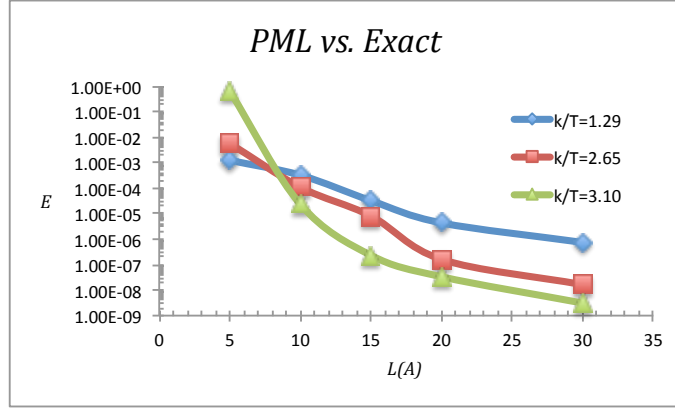
Figure 9.10: Maximum relative error for various wave vectors in a (5,5) single-walled carbon nanotube.

Now, let us consider a $(9, 5)$ Carbon nanotube. Without considering the Objective Structure, the unit cell of this nanotube would have 302 atoms, however, after adapting the symmetry of the structure, this number reduces to only 2. Figure 9.11 shows the density of scattering wave for $\kappa = 2.09$ after applying the PML method.
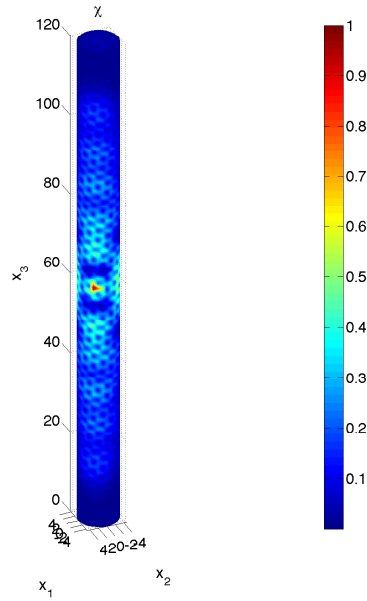
Figure 9.11: The density of the scattering wave for $\kappa = 2.09$ with PML method.

79

Moreover, this type of Carbon nanotube is considered as a semiconductor, since there exist a considerable energy gap in its band structure (Figure 9.12).
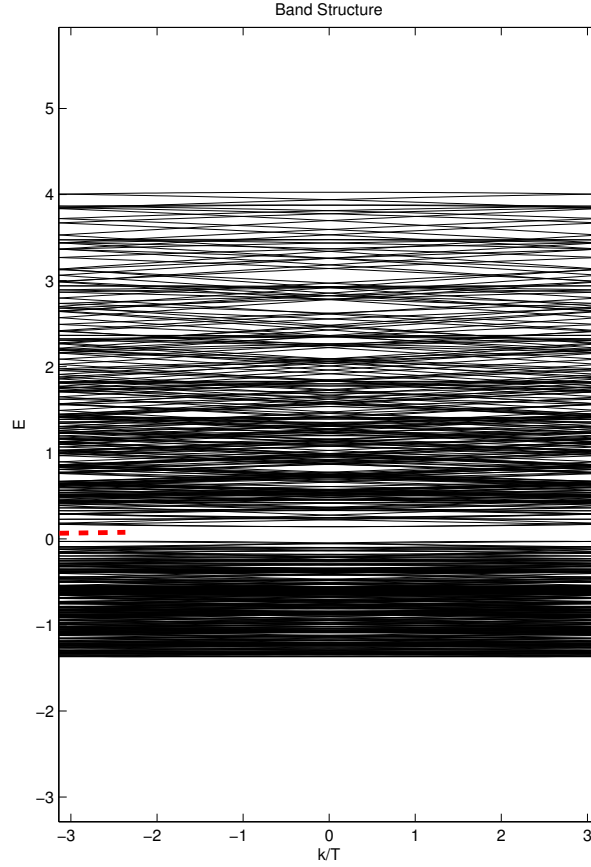
Figure 9.12: Band structure of $(9, 5)$ Carbon nanotube. The red dashed line indicates the energy of the defect mode shown in Figure 9.14

After applying a vacancy in the middle of the Carbon nanotube, the contour for the scattering and total wavefunction are shown in Figure 9.11.

9.3 Y-junction Carbon nanotube

The mutual interaction of the electron currents in a three branches of the Y-junction is shown to be the basis for a potentially new logic device [11]. In this section we investigate some electronic behavior of this type of nanotubes. Figure 9.13 shows a Y-junction, made out of three $(9, 5)$ Carbon nanotubes.
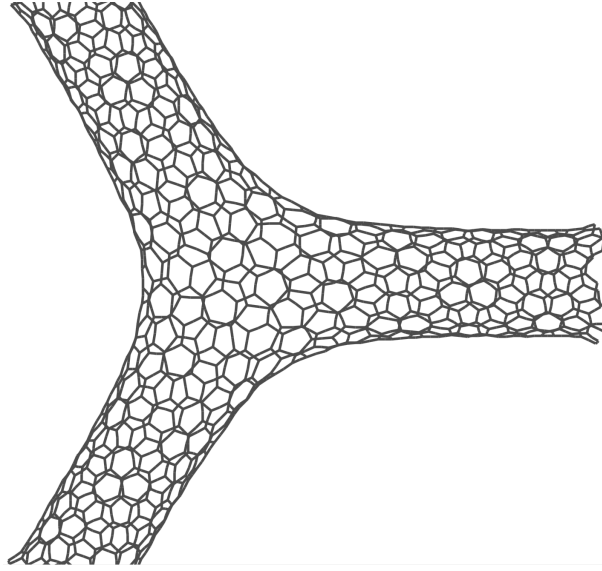
Figure 9.13: A schematic figure of Y-junction Carbon Nanotube with $(9, 5)$ chirality.

By applying PML method to the ends of this structure we can extract the band structure of this object, which of course looks almost exactly like that of a $(9, 5)$ single-walled carbon nanotube. The first contour in Figure 9.14 shows one of the eigenstates, corresponding to $\kappa = 1.43$. This eigenmode is similar to that of Bloch eigenmodes, which is scattering over the whole domain and never vanishes. Note that without applying the proper non-reflecting boundary condition (here PML), we would not be able to gain this result. However, the defect (junction) in this structure will create some extra modes that belong to the band gap. These modes are called defect modes (or D-modes). The second contour in Figure 9.14 shows the eigenstate

of one of these D-modes. Unlike the Bloch modes, the D-modes are localized around the defect. The energy corresponding to this mode is shown in Figure 9.12.

(a) $\kappa = 1.43$ (b) D-mode
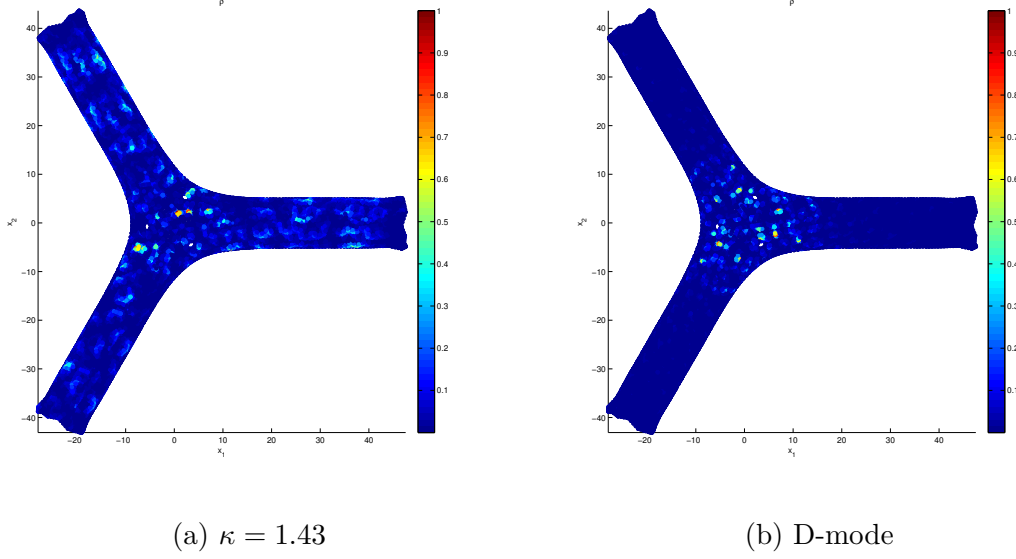
Figure 9.14: $(9, 5)$ Carbon nanotube eigenstates corresponding to $\kappa = 1.43$ and a defect mode in (a) and (b), respectively.

In both examples of single-walled and Y-junction Carbon nanotubes, we first investigated the proper thickness of the absorbing layer. Since we are certain about the general convergence of the results to that of exact non-reflecting boundary condition by now, we have considered the convergence of only one point. Figure 9.15 shows this convergence. As shown here, $10nm$ is a proper thickness for this example.
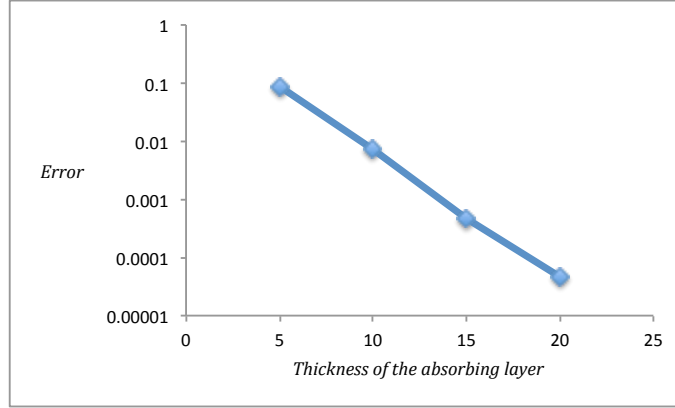
Figure 9.15: The convergence of the density of the wavefunction for one point in the Y-junction Carbon nanotube, as the thickness of the absorbing layer increases.

One of the interesting properties of Y-junction nanotubes appear after we destroy the symmetry of the structure. In order to do so, we simply remove one of the atoms in the lower branch in Figure 9.13. After causing this extra defect, we investigate the ratio of transmitted wave in the lower and upper branch, when the incident wave comes from the branch on the right side. Figure 9.16 shows the ratio of the average wave transmitted to the lower branch.
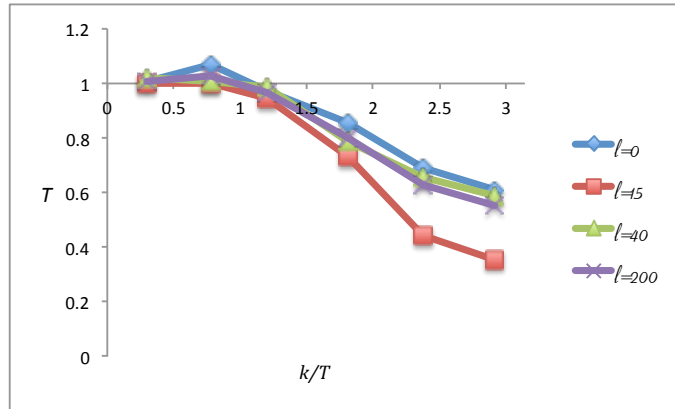
Figure 9.16: The ratio of transmitted wave to the lower branch, compared to the branch on the right-hand-side for a $(9, 5)$ Y-junction Carbon nanotube with a vacancy in the lower branch.

The plot shows that for lower wavenumbers, the electron wave almost slips in half. However, as the wavenumber increases the probability of finding the electron in the top branch gets higher than the lower branch. Moreover, this effect is more significant for some singular indices, compared to others. This difference is directly related to the position of vacancy and by changing the position, the angular index with the most effects will change. The eigenstates of this example, corresponding to $\kappa = 0.78$ and $\kappa = 2.38$ are shown in Figure 9.17

(a) $\kappa = 0.78$ (b) $\kappa = 2.38$
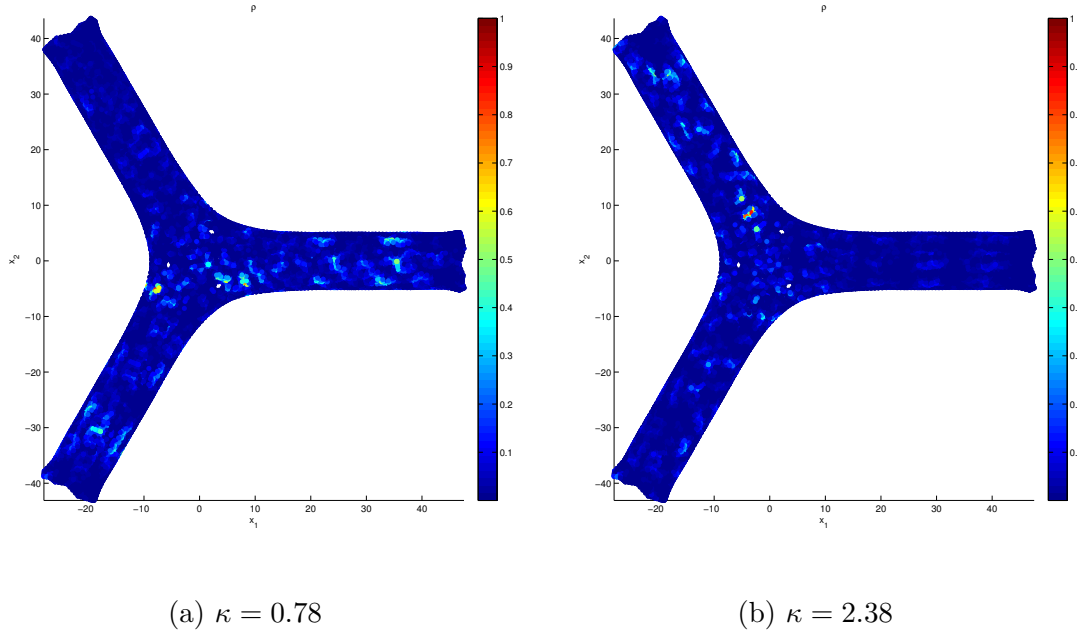
Figure 9.17: $(9, 5)$ Carbon nanotube eigenstates corresponding to $\kappa = 0.78$ and $\kappa = 2.38$ in the presence of a vacancy in the lower branch, respectively.

9.4 Kinked DNA

As the final example of this thesis we consider several different V-shaped DNA molecules. Followed by our TB development in the previous chapter, we now apply PML method to the ends of a kinked DNA molecule and study the electron scattering along the axis of the molecule for different kink angles. We consider various angles,
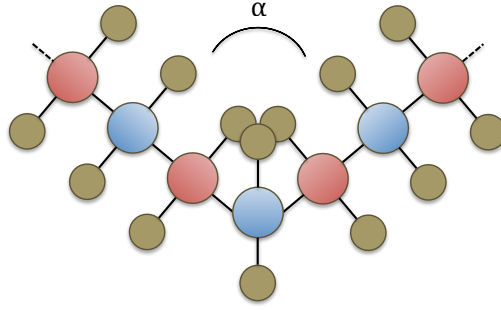
α, for Figure 9.18:

Figure 9.18: Fish-bone model for kinked DNA molecule.

Figure 9.19 shows this result for various angles. As expected, one can see the concentration of electron density around the defective area. Moreover, as the angle gets sharper and sharper, the intensity of the electron density in that area increases. All of these examples have been conducted for incident Bloch wave with $\kappa = 0.64$ and $E = -3.07eV$. Note that gaining these results would not have been possible without the application of absorbing boundary conditions.
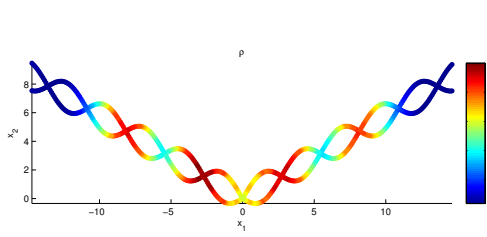
(a) $\alpha = \frac{2\pi}{3}$
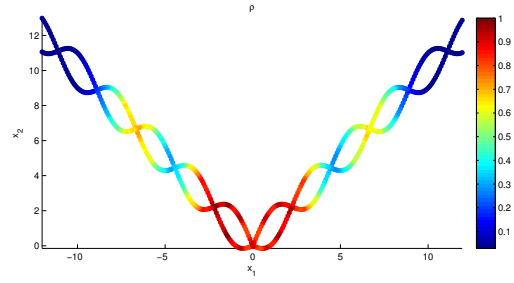
(b) $\alpha = \frac{\pi}{2}$
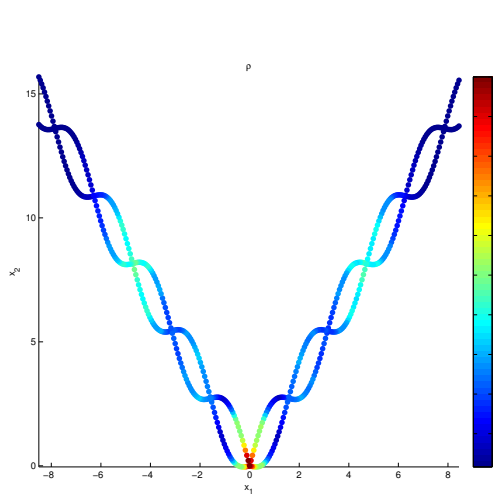
(c) $\alpha = \frac{\pi}{3}$
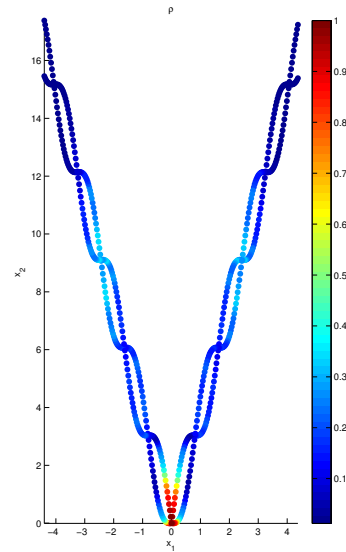
(d) $\alpha = \frac{\pi}{6}$

Figure 9.19: The electron density of V-shaped DNA molecule for $\kappa = 0.64$. The distances are in nanometers.

10

Conclusion

The time-harmonic Schrodinger equation for a periodic media with localized defects was considered. The well-known Sommerfeld radiation condition does not apply to this problem, since the periodic potential makes it an inhomogeneous space. We derived a Sommerfeld-like radiation condition for periodic problems. Also, The inhomogeneous media refrains us from using the non-reflecting boundary conditions, already known in literature. We derived the exact non-reflecting boundary condition, using the Green's function corresponding to the outgoing waves. The result is a highly non-local expression, which, although exact, is impractical to use. Moreover, calculation of the Green's function at each point requires an integration over the entire *k-space*. The integrant of this expression is rapidly oscillating and contains at lease on singularity in it. However, we showed that by using the proper integration schemes for oscillating functions and reducing the integration domains in the *k-space* to the energy bands that carry that specific energy, $E(k_0)$, one can use this NtD boundary condition.

On the other hand we considered the Perfectly Matched Layer method. Even though the absorbing layers cause some spurious reflections in an inhomogeneous

media, we showed that by considering a smooth absorption function, as the thickness of the absorbing layer increases, the PML method converges to the exact results with a promising rate. This convergence and error analysis proves that PML is not only reliable, but also the best option in hand for problems with local defects.

Moreover, we applied the PML method to Y-junction Carbon nanotubes and studied the ratio of transmission in the different branches. The results shows significant sensitivity to the wavenumber and angular index of the incident wave. Even though we did not simulate all of the possible incident waves, our results suggest that one may find a specific incident wave, for which the current only passes through one branch while the other waves pass through both of the branches. These results, may offer a chance to numerically explain the phenomenon observed in the experiments in [11].

Finally, we studied the kinked DNA molecules. even though the fishbone model that we implemented to develop the corresponding TB method is very simplified, nevertheless it shows the power of PML method to study the localized defects in such complicated molecules. The results for V-shapes DNA shows a concentration of electron density around the curved area, as expected. This concentration intensifies as the angle of the kink gets sharper and sharper.

11

Future Works

The Y-junction Carbon nanotubes that was briefly studies in our results section show very promising electronic properties that could be a benchmark for new generation of logic bases that can takeover the binary systems. Our first priority for the continuation of our studies is to get more in-depth of these structures and explore their electronic properties in various situations. More specifically, we would like to study the possibility of quantifying the transmission ratio of the branch that was depicted in the results section.

Moreover, recently, cup-stacked carbon nanotubes (CSCNTs) have attracted increasing attention as a special and functional nano-sized material in heterogeneous catalysis, solar cells, etc. From the morphological viewpoint, CSCNTs consist of many truncated conical graphene layers, different from conventional CNTs made up of multi-seamless cylinders of hexagonal carbon networks [51]. As one of the future works along with this thesis, we would like to study the electronic properties of this type of nano-structures in the presence of defects.

Finally, we would like to note that even though the techniques developed for applying non-reflection and absorbing boundary conditions are based on Schrodinger

equation, one can extend these formulations to similar problems, including phonon and heat transport. The only limitation for applying the non-reflecting boundary condition is the case where the potential corresponding to the defect is not decaying fast enough. In that case the integral of $\boldsymbol{y}$ may not be truncated to a bounded domain, Ω_c, as it is done in equation (7.20).

Bibliography

[1] A. Acharya, "A Model of Crystal Plasticity Based on the Theory of Continuously Distributed Dislocations," *Journal of the Mechanics and Physics of Solids*, vol. 49, no. 4, pp. 761 – 784, 2001. [Online]. Available: http://www.sciencedirect.com/science/article/pii/S0022509600000600.

[2] ——, "New Inroads in an Old Subject: Plasticity, from Around the Atomic to the Macroscopic Scale," *Journal of the Mechanics and Physics of Solids*, vol. 58, no. 5, pp. 766 – 778, 2010. [Online]. Available: http://www.sciencedirect.com/science/article/pii/S0022509610000190.

[3] A. Acharya, K. Matthies, and J. Zimmer, "Travelling Wave Solutions for a Quasilinear Model of Field Dislocation Mechanics," *Journal of the Mechanics and Physics of Solids*, vol. 58, no. 12, pp. 2043–2053, December 2010. [Online]. Available: http://opus.bath.ac.uk/22134/.

[4] A. Acharya and L. Tartar, "On an Equation from the Theory of Field Dislocation Mechanics." *Bulletin of the Italian Mathematical Union*, vol. 9, no. IV, pp. 409–444, 2011.

[5] A. Acharya and K. Dayal, "Continuum mechanics of line defects in liquid crystals and liquid crystal elastomers," *Quarterly of Applied Mathematics*, vol. 72, no. 1, pp. 33–64, 2014.

[6] A. Aghaei, K. Dayal, and R. S. Elliott, "Symmetry-adapted phonon analysis of nanotubes," *Journal of the Mechanics and Physics of Solids*, vol. 61, pp. 557–578, 2013.

[7] G. Allaire, "Two-scale convergence and homogenization of periodic structures," *School on homogenization, ICTP, Trieste*, 1993.

[8] X. Antoine, C. Besse, and P. Klein, "Absorbing boundary conditions for the one-dimensional schrödinger equation with an exterior repulsive potential," *J. Comput. Phys.*, vol. 228, no. 2, pp. 312–335, Feb. 2009. [Online]. Available: http://dx.doi.org/10.1016/j.jcp.2008.09.013.

[9] D. Baffet, J. Bielak, D. Givoli, T. Hagstrom, and D. Rabinovich, "Long-time stable high-order absorbing boundary conditions for elastodynamics," *Computer Methods in Applied Mechanics and Engineering*, vol. 241–244, no. 0, pp. 20 – 37, 2012. [Online]. Available: http://www.sciencedirect.com/science/article/pii/S0045782512001557.

[10] J. M. Ball and A. Zarnescu, "Orientable and Non-Orientable Director Fields for Liquid Crystals," *PAMM*, vol. 7, no. 1, pp. 1 050 701–1 050 704, 2007. [Online]. Available: http://dx.doi.org/10.1002/pamm.200700489.

[11] P. R. Bandaru, C. Daraio, S. Jin, and A. M. Rao, "Novel electrical switching behaviour and logic in carbon nanotube y-junctions," *Nat Mater*, vol. 4, no. 9, pp. 663–666, 09 2005. [Online]. Available: http://dx.doi.org/10.1038/nmat1450.

[12] G. Bastard, *Wave mechanics applied to semiconductor heterostructures*, ser. Monographies de physique. Les Éditions de Physique, 1988. [Online]. Available: http://books.google.com/books?id=5rrvAAAAMAAJ.

[13] U. Basu and A. K. Chopra, "Perfectly matched layers for time-harmonic elastodynamics of unbounded domains: theory and finite-element implementation," *Computer Methods in Applied Mechanics and Engineering*, vol. 192, no. 11–12, pp. 1337 – 1375, 2003. [Online]. Available: http://www.sciencedirect.com/science/article/pii/S0045782502006424.

[14] J.-P. Berenger, "A perfectly matched layer for the absorption of electromagnetic waves," *Journal of Computational Physics*, vol. 114, no. 2, pp. 185 – 200, 1994. [Online]. Available: http://www.sciencedirect.com/science/article/pii/S0021999184711594.

[15] J. Bernholc and S. T. Pantelides, "Scattering-theoretic method for defects in semiconductors. i. tight-binding description of vacancies in si, ge, and gaas," *Phys. Rev. B*, vol. 18, pp. 1780–1789, Aug 1978. [Online]. Available: http://link.aps.org/doi/10.1103/PhysRevB.18.1780.

[16] J. H. Bramble and J. E. Pasciak, "Analysis of a finite pml approximation for the three dimensional time-harmonic maxwell and acoustic scattering problems," *MATH. COMP*, pp. 597–614, 2006.

[17] J. Callaway and S. P. Singhal, "Scattering theory of defects in solids: Theory and application to the atomic vacancy," *International Journal of Quantum Chemistry*, vol. 18, no. S14, pp. 651–663, 1980. [Online]. Available: http://dx.doi.org/10.1002/qua.560180866.

92

[18] J. Carr and R. Pego, "Metastable patterns in solutions of $u_t = \epsilon^2 u_{xx} - f(u)$," *Communications on pure and applied mathematics*, vol. 42, no. 5, pp. 523–576, 1989.

[19] P. Cermelli and E. Fried, "The Evolution Equation for a Disclination in a Nematic Liquid Crystal," *Proceedings of the Royal Society of London. Series A: Mathematical, Physical and Engineering Sciences*, vol. 458, no. 2017, pp. 1–20, 2002.

[20] B. G. Chen, G. P. Alexander, and R. D. Kamien, "Symmetry Breaking in Smectics and Surface Models of Their Singularities," *Proceedings of the National Academy of Sciences*, vol. 106, no. 37, pp. 15 577–15 582, 2009. [Online]. Available: http://www.pnas.org/content/106/37/15577.abstract.

[21] W. C. Chew and W. H. Weedon, "A 3d perfectly matched medium from modified maxwell's equations with stretched coordinates," *Microwave and Optical Technology Letters*, vol. 7, no. 13, pp. 599–604, 1994. [Online]. Available: http://dx.doi.org/10.1002/mop.4650071304.

[22] P. Cladis and M. Kléman, "Non-Singular Disclinations of Strength S = + 1 in Nematics," *Journal de Physique*, vol. 33, no. 5-6, pp. 591–598, 1972. [Online]. Available: http://hal.archives-ouvertes.fr/jpa-00207284.

[23] R. DeWit, "Theory of Disclinations: IV. Straight Disclinations," *Journal of Research of the National Bureau of Standards - A. Physics and Chemistry*, vol. 477A, no. 5, pp. 607–658, 1973.

[24] M. Ehrhardt and C. Zheng, "Exact artificial boundary conditions for problems with periodic structures," *Journal of Computational Physics*, vol. 227, no. 14, pp. 6877 – 6894, 2008. [Online]. Available: http://www.sciencedirect.com/science/article/pii/S0021999108002015.

[25] B. Engquist and A. Majda, "Absorbing boundary conditions for numerical simulation of waves," *Proceedings of the National Academy of Sciences*, vol. 74, no. 5, pp. 1765–1766, 1977. [Online]. Available: http://www.pnas.org/content/74/5/1765.abstract.

[26] J. L. Ericksen, "Liquid Crystals with Variable Degree of Orientation," *Archive for Rational Mechanics and Analysis*, vol. 113, pp. 97–120, 1991, 10.1007/BF00380413. [Online]. Available: http://dx.doi.org/10.1007/BF00380413.

[27] ——, "Remarks Concerning Forces on Line Defects," *ZAMP-Zeitschrift fur Angewandte Mathematik und Physik*, vol. 46, p. 247, 1995.

[28] H. Eschrig, *Optimized LCAO method and the electronic structure of extended systems.* Springer-Verlag, 1988.

[29] J. D. Eshelby, "The Force on a Disclination in a Liquid Crystal," *Philosophical Magazine A*, vol. 42, no. 3, pp. 359–367, 1980.

[30] F. C. Frank, "I. Liquid Crystals. On the Theory of Liquid Crystals," *Discuss. Faraday Soc.*, vol. 25, pp. 19–28, 1958. [Online]. Available: http://dx.doi.org/10.1039/DF9582500019.

[31] D. Givoli, "Non-reflecting boundary conditions," *J. Comput. Phys.*, vol. 94, no. 1, pp. 1–29, May 1991. [Online]. Available: http://dx.doi.org/10.1016/0021-9991(91)90135-8.

[32] ——, "High-order local non-reflecting boundary conditions: a review," *Wave Motion*, vol. 39, no. 4, pp. 319 – 326, 2004, ¡ce:title¿New computational methods for wave propagation¡/ce:title¿. [Online]. Available: http://www.sciencedirect.com/science/article/pii/S0165212503001203.

[33] P. D. Gr Goire Allaire, Anton Arnold, *Quantum Transport 1st edition. Modelling Analysis and Asymptotics*, G. F. Naoufel Ben Abdallah, Ed. Springer, 2006.

[34] M. Hancock, "Method of Greens Functions," 2006, lecture notes.

[35] D. Harley Klein, L. Gary Leal, C. J. García-Cervera, and H. D. Ceniceros, "Three-Dimensional Shear-Driven Dynamics of Polydomain Textures and Disclination Loops in Liquid Crystalline Polymers," *Journal of Rheology*, vol. 52, no. 3, pp. 837–863, 2008. [Online]. Available: http://link.aip.org/link/?JOR/52/837/1.

[36] L. G. Hawke, G. Kalosakas, and C. Simserides, "Electronic parameters for charge transfer along dna," *The European Physical Journal E: Soft Matter and Biological Physics*, vol. 32, no. 3, pp. 291–305, 2010.

[37] Y. Huang, S. S. Iyengar, D. J. Kouri, and D. K. Hoffman, "Further analysis of solutions to the time-independent wave packet equations of quantum dynamics. ii. scattering as a continuous function of energy using finite, discrete approximate hamiltonians," *Environmental and Ecological Statistics*, vol. 105, no. 3, pp. 927–939, 1996.

[38] D. Huybrechs and S. Olver, "Highly oscillatory quadrature," *Highly oscillatory problems*, no. 366, pp. 25–50, 2009.

[39] D. K. Hwang and A. D. Rey, "Computational studies of optical textures of twist disclination loops in liquid-crystal films by using the finite-difference time-domain method," *J. Opt. Soc. Am. A*, vol. 23, no. 2, pp. 483–496, Feb 2006. [Online]. Available: http://josaa.osa.org/abstract.cfm?URI=josaa-23-2-483.

[40] M. I. Katsnelson, "Graphene: carbon in two dimensions," *Materials Today*, vol. 10, no. 1–2, pp. 20 – 27, 2007. [Online]. Available: http://www.sciencedirect.com/science/article/pii/S1369702106717886.

[41] S. Kim, Joseph, and E. Pasciak, "The computation of resonances in open systems using a perfectly matched layer," *Math. Comp*, 2009.

[42] M. Kleman and J. Friedel, "Disclinations, Dislocations, and Continuous Defects: A Reappraisal," *Rev. Mod. Phys.*, vol. 80, pp. 61–115, Jan 2008. [Online]. Available: http://link.aps.org/doi/10.1103/RevModPhys.80.61.

[43] M. Kléman and O. D. Lavrentovich, *Soft Matter Physics: An Introduction*, ser. Partially Ordered Systems. Springer, 2003. [Online]. Available: http://books.google.com/books?id=78LRUXvBR4MC.

[44] S. Kralj, E. G. Virga, and S. Žumer, "Biaxial Torus Around Nematic Point Defects," *Phys. Rev. E*, vol. 60, pp. 1858–1866, Aug 1999. [Online]. Available: http://link.aps.org/doi/10.1103/PhysRevE.60.1858.

[45] E. Kröner, "Continuum Theory of Defects. In: Physics of Defects," *Les Houches Summer School*, pp. 215–315, 1981.

[46] ——, "Configurational and Material Forces in the Theory of Defects in Ordered Structures," in *Materials Science Forum*, vol. 123. Trans Tech Publ, 1993, pp. 447–454.

[47] F. M. Leslie, "Continuum Theory for Nematic Liquid Crystals," *Continuum Mechanics and Thermodynamics*, vol. 4, pp. 167–175, 1992, 10.1007/BF01130288. [Online]. Available: http://dx.doi.org/10.1007/BF01130288.

[48] S. Li, X. Liu, A. Agrawal, and A. C. To, "Perfectly matched multiscale simulations for discrete lattice systems: Extension to multiple dimensions," *Phys. Rev. B*, vol. 74, p. 045418, Jul 2006. [Online]. Available: http://link.aps.org/doi/10.1103/PhysRevB.74.045418.

95

[49] F. H. Lin and C. Liu, "Existence of Solutions for the Ericksen-Leslie System," *Archive for rational mechanics and analysis*, vol. 154, no. 2, pp. 135–156, 2000.

[50] C. Liu and N. J. Walkington, "Approximation of Liquid Crystal Flows," *SIAM Journal on Numerical Analysis*, vol. 37, no. 3, pp. pp. 725–741, 2000. [Online]. Available: http://www.jstor.org/stable/2587312.

[51] Q. Liu, W. Ren, Z.-G. Chen, L. Yin, F. Li, H. Cong, and H.-M. Cheng, "Semiconducting properties of cup-stacked carbon nanotubes," *Carbon*, vol. 47, no. 3, pp. 731 – 736, 2009. [Online]. Available: http://www.sciencedirect.com/science/article/pii/S0008622308006003.

[52] A. Majumdar and A. Zarnescu, "Landau–De Gennes Theory of Nematic Liquid Crystals: the Oseen–Frank Limit and Beyond," *Archive for Rational Mechanics and Analysis*, vol. 196, pp. 227–280, 2010, 10.1007/s00205-009-0249-2. [Online]. Available: http://dx.doi.org/10.1007/s00205-009-0249-2.

[53] J. Marshall and K. Dayal, "Atomistic-to-continuum multiscale modeling with long-range electrostatic interactions in ionic solids," *Journal of the Mechanics and Physics of Solids*, vol. 62, no. 0, pp. 137 – 162, 2014, sixtieth anniversary issue in honor of Professor Rodney Hill. [Online]. Available: http://www.sciencedirect.com/science/article/pii/S0022509613002093.

[54] R. M. Martin, *Electronic Structure: Basic Theory and Practical Methods*. Cambridge, 2008.

[55] A. Mayer, "Band structure and transport properties of carbon nanotubes using a local pseudopotential and a transfer-matrix technique," *Carbon*, vol. 42, no. 10, pp. 2057 – 2066, 2004. [Online]. Available: http://www.sciencedirect.com/science/article/pii/S0008622304002738.

[56] P. Monk, F. Collino, F. Collino, and E. P. Monk, "The perfectly matched layer in curvilinear coordinates," *SIAM J. Sci. Comput*, vol. 19, pp. 2061–2090, 1996.

[57] M. Murata and T. Tsuchida, "Asymptotics of green functions and martin boundaries for elliptic operators with periodic coefficients," *Journal of Differential Equations*, vol. 195, no. 1, pp. 82 – 118, 2003. [Online]. Available: http://www.sciencedirect.com/science/article/pii/S002203960300192X.

[58] L. Ó. Náraigh and D. O'Kiely, "Homogenization theory for periodic potentials in the schrödinger equation," *European Journal of Physics*, vol. 34, no. 1, p. 19, 2012.

[59] A. F. Oskooi, L. Zhang, Y. Avniel, and S. G. Johnson, "The failure of perfectly matched layers, and towards their redemptionby adiabatic absorbers," *Opt. Express*, vol. 16, no. 15, pp. 11 376–11 392, Jul 2008. [Online]. Available: http://www.opticsexpress.org/abstract.cfm?URI=oe-16-15-11376.

[60] S. T. Pantelides, J. Bernholc, J. Pollmann, and N. O. Lipari, "Green's function scattering-theoretic methods for point defects, surfaces, and interfaces in solids," *International Journal of Quantum Chemistry*, vol. 14, no. S12, pp. 507–521, 1978. [Online]. Available: http://dx.doi.org/10.1002/qua.560140845.

[61] S. T. Pantelides, "The electronic structure of impurities and other point defects in semiconductors," *Rev. Mod. Phys.*, vol. 50, pp. 797–858, Oct 1978. [Online]. Available: http://link.aps.org/doi/10.1103/RevModPhys.50.797.

[62] K. Sakoda, *Optical Properties of Photonic Crystals*, ser. Springer Series in Optical Sciences. Springer, 2005. [Online]. Available: http://books.google.com/books?id=Yecl3EQpXgYC.

[63] A. Sommerfeld, *Partial Differential Equations in physics*. Elsevier, 1953.

[64] A. Sonnet, A. Kilian, and S. Hess, "Alignment Tensor Versus Director: Description of Defects in Nematic Liquid Crystals," *Phys. Rev. E*, vol. 52, pp. 718–722, Jul 1995. [Online]. Available: http://link.aps.org/doi/10.1103/PhysRevE.52.718.

[65] I. W. Stewart, *The Static and Dynamic Continuum Theory of Liquid Crystals*. Taylor and Francis, 2004. [Online]. Available: http://strathprints.strath.ac.uk/2157/.

[66] E. B. Tadmor and R. E. Miller, *Modeling materials: continuum, atomistic and multiscale techniques*. Cambridge University Press, 2011.

[67] J. A. P. W. J. Hehre, R. F. Stewart, "Self-Consistent Molecular-Orbital Methods. I. Use of Gaussian Expansions of Slater-Type Atomic Orbitals," *Journal of Chemical Physics*, 1969.

[68] A. R. Williams, P. J. Feibelman, and N. D. Lang, "Green's-function methods for electronic-structure calculations," *Phys. Rev. B*, vol. 26, pp. 5433–5444, Nov 1982. [Online]. Available: http://link.aps.org/doi/10.1103/PhysRevB.26.5433.

[69] J. R. Willis, "Second-Order Effects of Dislocations in Anisotropic Crystals," *International Journal of Engineering Science*, vol. 5, no. 2, pp. 171 – 190,

1967. [Online]. Available: http://www.sciencedirect.com/science/article/pii/
0020722567900031.

[70] X. Yang, M. Forest, W. Mullins, and Q. Wang, "Dynamic Defect Morphology
and Hydrodynamics of Sheared Nematic Polymers in Two Space Dimensions,"
Journal of Rheology, vol. 53, no. 3, pp. 589–615, 2009. [Online]. Available:
http://link.aip.org/link/?JOR/53/589/1.

[71] D. Zhang, *Electromechanical Characterization of Quasi-one Dimensional
Nanostructures of Silicon, Carbon, and Molybdenum Disulfide Via Symmetry-
adapted Tight-binding Molecular Dynamics.* University of Minnesota, 2009.
Major: Material Science and Engineering., 2009. [Online]. Available:
http://books.google.com/books?id=sEmyygAACAAJ.

Appendix A

An Explicit solution for θ

An analytic solution for the director field corresponding to $\boldsymbol{\lambda}$ source fields in 3.5 in an infinite domain is developed, to serve as motivation for some of our claims in Section 2.2. The source fields are layer-like but do not have compact support on bounded domains. Consider a δ sequence [34]:

$$\delta_n(x) = \frac{n}{\sqrt{\pi}} e^{-(nx)^2}.$$

So that, $\int_{-\infty}^{\infty} \delta_n(x) = \mathrm{erf}(x) = 1$, for any n. Also, consider a H sequence, which converges to the Heaviside step function

$$H_n(x) = \frac{1}{2} \left(\tan^{-1}(nx) + 1 \right).$$

Now, one can define $\boldsymbol{\lambda}$ as

$$\boldsymbol{\lambda}_n(\boldsymbol{x}) = 2\pi K \delta_n(x_1) H_n(x_2) \boldsymbol{e}_1.$$

Note that, for any given n,

$$\oint \boldsymbol{\lambda}_n . dr = 2\pi K \int_{x_1^+} \delta_n(x_1) dx_1 = 2\pi K$$

In order to solve (3.5), one can use Green's function method for an infinite 2D domain, where the Green's function is

$$G(\boldsymbol{x}, \boldsymbol{x}') = \frac{1}{2\pi} \ln(|\boldsymbol{x} - \boldsymbol{x}'|).$$

Now, the expression for θ_n in terms of the Green's function will be

$$\theta_n = \int_{V'} G(\boldsymbol{x}, \boldsymbol{x}') div \, \boldsymbol{\lambda}_n(\boldsymbol{x}') dV$$

Integrating by part and considering the fact that the $\boldsymbol{\lambda}_n$ field has only the $\boldsymbol{e}_1$ component

$$\theta_n = \int_{\partial V'} G(\boldsymbol{x}, \boldsymbol{x}') \boldsymbol{\lambda}_n(\boldsymbol{x}') \cdot \boldsymbol{\nu} dS - \int_{V'} \frac{\partial}{\partial x'_1} G(\boldsymbol{x}, \boldsymbol{x}') \boldsymbol{\lambda}_n(\boldsymbol{x}') dV$$

$$= -\frac{1}{2\pi} \int_{V'} \frac{x'_1 - x_1}{|\boldsymbol{x}' - \boldsymbol{x}|^2} \boldsymbol{\lambda}_n(\boldsymbol{x}') dV$$

$$= \frac{1}{2\pi} \int_{x'_1} \int_{x'_2} \frac{x_1 - x'_1}{|\mathbf{x}' - \mathbf{x}|^2} 2\pi k \delta_n(x'_1) H_n(x'_2) dx'_2 dx'_1$$

As a result:

$$\theta_n = \frac{Kn}{2\sqrt{\pi}} \int_{x'_1} \int_{x'_2} \frac{x_1 - x'_1}{|\boldsymbol{x}' - \boldsymbol{x}|^2} e^{-(nx'_1)^2} \left(\tan^{-1}(nx'_2) + 1 \right) dx'_2 dx'_1 \qquad (A.1)$$

Note that in case of $n \to \infty$,

$$\theta_\infty = \frac{K}{2} \int_{x'_1} \int_{x'_2} \frac{x_1 - x'_1}{|\boldsymbol{x}' - \boldsymbol{x}|^2} \delta_\infty(x'_1) H(x'_2) dx'_2 dx'_1$$

$$= \frac{K}{2} \int_{x'_2=0}^{\infty} \frac{x_1}{x_1^2 + (x_2 - x'_2)^2} dx'_2$$

$$= \frac{K}{2} \tan^{-1} \left(\frac{x_2 - x'_2}{x_1} \right) \Big|_{x'_2=0}^{\infty}$$

as a result, θ_n will converge to

$$\theta = K \tan^{-1} \left(\frac{x_2}{x_1} \right) + c, \qquad \text{(A.2)}$$

which is exactly Frank's solution for planar director fields for straight disclinations for the 1-constant energy.

Appendix B

Solution for $\boldsymbol{E}_r^\theta$

We provide the following solution from [5] for completeness. Consider $\boldsymbol{\beta}_r^\theta$ given by

$$\boldsymbol{\beta}_r^\theta(x_1, x_2) = \begin{cases} \rho(r)\boldsymbol{e}_3, r < r_c \\ \boldsymbol{0}, r \geq r_c \end{cases} \; ; r = (x_1^2 + x_2^2)^{\frac{1}{2}} \tag{B.1}$$

with the stipulation that

$$2K\pi = \int_0^{2\pi} \int_0^{r_c} \rho(r) \; dr \; rd\psi \Rightarrow K = \int_0^{r_c} \rho(r) \; rdr \tag{B.2}$$

where K is the strength of the disclination and r_c is a core radius. Then following Section 5.2 in [1], we have the solution

$$\text{For } r < r_c : \quad E_{r1}^\theta = \frac{-x_2}{r^2} \int_0^r \rho(s)s \; ds, \quad E_{r2}^\theta = \frac{x_1}{r^2} \int_0^r \rho(s)s \; ds$$

$$\text{For } r \geq r_c : \quad E_{r1}^\theta = K\frac{-x_2}{r^2}, \quad E_{r2}^\theta = K\frac{x_1}{r^2}. \tag{B.3}$$

It can be checked that this solution indeed satisfies the governing equations for $\boldsymbol{E}_r^\theta$ for any ρ satisfying the given conditions. For the choice

$$\rho(r) = \begin{cases} \frac{2K}{r_c}\left(\frac{1}{r} - \frac{1}{r_c}\right), r \leq r_c \\ 0, r > r_c \end{cases}$$

the inside-core solution evaluates to

$$\text{For } r \leq r_c: \quad E_{r1}^\theta = \frac{-x_2}{r^2} \left(\frac{2K}{r_c} \left[r - \frac{r^2}{2r_c} \right] \right), \quad E_{r2}^\theta = \frac{x_1}{r^2} \left(\frac{2K}{r_c} \left[r - \frac{r^2}{2r_c} \right] \right)$$

while the outside-core distribution remains unchanged.

Appendix C

two-scale method

C.1 Homogenization of Schrodinger equation in periodic media

Homogenization theory is a powerful tool for understanding the effects of the small-scale disturbances on the large-scale features in partial differential equations. We use homogenization theory to derive asymptotic solutions of the Schrodinger equation with periodic potentials. Following the foot steps of [7] and [58], and rewriting equation (7.8) as a convergent series according to [33]:

$$-\left(\nabla_x + \epsilon^{-1}\nabla_y\right)^2\psi_\epsilon + \left(\epsilon^{-2}V_p(\boldsymbol{y}) + V_d(\boldsymbol{x},\boldsymbol{y})\right)\psi_\epsilon = i\left(\frac{\partial}{\partial t} + \epsilon^{-2}\frac{\partial}{\partial T}\right)\psi_\epsilon - V_d(\boldsymbol{x},\boldsymbol{y})\phi_k(\boldsymbol{y})$$

(C.1)

Note that, we take $dT/dt = \epsilon^{-2}$. We consider the following ansatz:

$$\psi_\epsilon(\boldsymbol{x},\boldsymbol{y},t,T) = e^{-iTE_k - it\tilde{E}}\sum_{p=0}^{\infty}\epsilon^p\Psi_p(\boldsymbol{x},\boldsymbol{y})$$

(C.2)

Substituting (C.2) into (C.1) and separating the scales of this equation will lead into a series of equations. For the set of terms with order of ϵ^{-2} we have:

$$-\nabla_y^2\Psi_0(\boldsymbol{x},\boldsymbol{y}) + V_p(\boldsymbol{y})\Psi_0(\boldsymbol{x},\boldsymbol{y}) = E_k\Psi_0(\boldsymbol{x},\boldsymbol{y})$$

(C.3)

104

We can immediately separate x and y variables, so that the above equation would follow Bloch's theorem:

$$\Psi_0(\boldsymbol{x}, \boldsymbol{y}) = f(\boldsymbol{x})\phi_k(\boldsymbol{y}) \tag{C.4}$$

the terms with the order of ϵ^{-1} form the following equation:

$$-\nabla_y^2\Psi_1 - 2\nabla_x f \cdot \nabla_y \phi_k + V_p(\boldsymbol{y})\Psi_1(\boldsymbol{x}, \boldsymbol{y}) = E_k\Psi_1(\boldsymbol{x}, \boldsymbol{y}) \tag{C.5}$$

This equation also has a separable solution $\Psi_1(\boldsymbol{x}, \boldsymbol{y}) = \nabla_x f(\boldsymbol{x}) \cdot \boldsymbol{g}(\boldsymbol{y})$. This leads to:

$$\nabla_x f \cdot \left\{ -\nabla_y^2 \boldsymbol{g} - 2\nabla_y \phi_k + \left(V_p(\boldsymbol{y}) - E_k\right)\boldsymbol{g}(\boldsymbol{y}) \right\} = 0 \tag{C.6}$$

Using the Green's function for Schrodinger's equation in periodic media, one can find $\boldsymbol{g}(\boldsymbol{y})$:

$$\boldsymbol{g}(\boldsymbol{y}) = -2 \int_{Y'} \int_{k'} \frac{\tilde{\phi}_{k'}(\boldsymbol{y})\phi_{k'}(\boldsymbol{y}')}{E_k - E_{k'}} d^3k \nabla \phi_k(\boldsymbol{y}') dV_y \tag{C.7}$$

Finally, the terms in macro-scale, i.e. the order of ϵ^0, leads to:

$$-\phi_k(\boldsymbol{y})\nabla_x^2 f - 2\nabla_x^2 f\nabla_y \cdot \boldsymbol{g} - \nabla_y^2\Psi_2(\boldsymbol{x}, \boldsymbol{y}) + \left(V_p(\boldsymbol{y}) - E_k\right)\Psi_2(\boldsymbol{x}, \boldsymbol{y}) \tag{C.8}$$
$$+ V_d(\boldsymbol{x}, \boldsymbol{y})f(\boldsymbol{x})\phi_k(\boldsymbol{y}) = -V_d(\boldsymbol{x})\phi_k(\boldsymbol{y})$$

Following [58], we consider $\Psi_2(\boldsymbol{x}, \boldsymbol{y}) = \nabla_x^2 f(\boldsymbol{x})h(\boldsymbol{y})$ to separate the values:

$$-\left\{\phi_k(\boldsymbol{y}) + 2\nabla_y \cdot \boldsymbol{g} + \nabla_y^2 h - \left(V_p(\boldsymbol{y}) - E_k\right)h(\boldsymbol{y})\right\}\nabla_x^2 f + V_d(\boldsymbol{x}, \boldsymbol{y})\phi_k(\boldsymbol{y})f(\boldsymbol{x}) = \tilde{E}\phi_k(\boldsymbol{y})f(\boldsymbol{x}) \tag{C.9}$$

C.2 An attempt to understand the scaling of the potential functions

In order to better understand and justify the scaling of the potential functions in the previous section, we attempt to study the nonlocal contribution of an energy term, defined in the following way:

$$W[\phi(\boldsymbol{x}, \boldsymbol{y})] = \int_{\boldsymbol{x} \in \Omega} \int_{\boldsymbol{y} \in \mathcal{B}} \phi^*(\boldsymbol{x}, \boldsymbol{y})V(\boldsymbol{x}, \boldsymbol{y})\phi(\boldsymbol{x}, \boldsymbol{y})dydx \tag{C.10}$$

where $\mathcal{B}$ is the unit cell. Note that although W may not have a physical significance, it is mathematically, similar to electrostatic energy [53]. Now, using the integral representation of ϕ that we shown in equation (7.11), W is given by

$$W\big[\phi(\boldsymbol{x},\boldsymbol{y})\big] = \int_{\boldsymbol{x},\boldsymbol{x}'\in\Omega;\boldsymbol{x}\neq\boldsymbol{x}'} \int_{\boldsymbol{y},\boldsymbol{y}'\in\mathcal{B}} \phi^*(\boldsymbol{x},\boldsymbol{y})V(\boldsymbol{x},\boldsymbol{y})G(\boldsymbol{x},\boldsymbol{y},\boldsymbol{x}',\boldsymbol{y}')V(\boldsymbol{x}',\boldsymbol{y}')\phi(\boldsymbol{x}',\boldsymbol{y}')dy'dx'dydx$$

Considering a three-dimensional case, where $G(\boldsymbol{x},\boldsymbol{y},\boldsymbol{x}',\boldsymbol{y}') = \dfrac{e^{\imath\left(k|\boldsymbol{x}+\epsilon\boldsymbol{y}-\boldsymbol{x}'-\epsilon\boldsymbol{y}'|\right)}}{|\boldsymbol{x}+\epsilon\boldsymbol{y}-\boldsymbol{x}'-\epsilon\boldsymbol{y}'|}$, one can rewrite W as

$$W\big[\phi(\boldsymbol{x},\boldsymbol{y})\big] = \int_{\boldsymbol{x},\boldsymbol{x}'\in\Omega;\boldsymbol{x}\neq\boldsymbol{x}'} \int_{\boldsymbol{y},\boldsymbol{y}'\in\mathcal{B}} \frac{\rho^*(\boldsymbol{x}',\boldsymbol{y}')\rho(\boldsymbol{x},\boldsymbol{y})}{|\boldsymbol{x}+\epsilon\boldsymbol{y}-\boldsymbol{x}'-\epsilon\boldsymbol{y}'|} dy'dydx'dx \qquad (\text{C.11})$$

where,

$$\rho(\boldsymbol{x},\boldsymbol{y}) = e^{\imath(k|\boldsymbol{x}+\epsilon\boldsymbol{y}-\boldsymbol{x}'-\epsilon\boldsymbol{y}'|)}V(\boldsymbol{x},bfy)\phi(\boldsymbol{x},\boldsymbol{y})$$

Now, consider the Taylor expansion of the denominator in (C.11) around $\boldsymbol{x}-\boldsymbol{x}'$

$$\frac{1}{|\boldsymbol{x}+\epsilon\boldsymbol{y}-\boldsymbol{x}'-\epsilon\boldsymbol{y}'|} = \frac{1}{|\boldsymbol{x}-\boldsymbol{x}'|} + \frac{\partial}{\partial|\boldsymbol{x}-\boldsymbol{x}'|}\left(\frac{1}{|\boldsymbol{x}-\boldsymbol{x}'|}\right)\cdot\epsilon(\boldsymbol{y}-\boldsymbol{y}') \qquad (\text{C.12})$$

$$+ 1/2\frac{\partial^2}{\partial|\boldsymbol{x}-\boldsymbol{x}'|^2}\left(\frac{1}{|\boldsymbol{x}-\boldsymbol{x}'|}\right)\epsilon^2 : (\boldsymbol{y}-\boldsymbol{y}')\otimes(\boldsymbol{y}-\boldsymbol{y}')$$

$$+ 1/6\frac{\partial^3}{\partial|\boldsymbol{x}-\boldsymbol{x}'|^3}\left(\frac{1}{|\boldsymbol{x}-\boldsymbol{x}'|}\right)\epsilon^3 : (\boldsymbol{y}-\boldsymbol{y}')\otimes(\boldsymbol{y}-\boldsymbol{y}')\otimes(\boldsymbol{y}-\boldsymbol{y}')+$$

$$1/24\frac{\partial^4}{\partial|\boldsymbol{x}-\boldsymbol{x}'|^4}\left(\frac{1}{|\boldsymbol{x}-\boldsymbol{x}'|}\right)\epsilon^4 : (\boldsymbol{y}-\boldsymbol{y}')\otimes(\boldsymbol{y}-\boldsymbol{y}')\otimes(\boldsymbol{y}-\boldsymbol{y}')\otimes(\boldsymbol{y}-\boldsymbol{y}')$$

$$+ \mathcal{O}(\epsilon^5)$$

Now, since according to (C.1) the periodic potential function scales as $V_p = \tilde{V}/\epsilon^2$, which means that $\rho^*\rho$ scales as ϵ^{-4}. As a result, in order for the integral in (C.11) to be well-behaved, after substituting (C.12) in (C.11), the the first four terms of the integration must vanish. However, that does is not necessarily true. So, this attempt to justify the scaling of the periodic potential fails.

106

Even though the attempt for understanding the scaling of the potential functions by expanding the Green's function did not work, *Allaire et. al.* notes that having both periodic and local potentials of the same order of magnitude implies a strong mixing of different Bloch band components, while in our case the macroscopic potential vanishes fast enough, as ϵ tends to 0, so that it does not affect the phase function but only the amplitude [7].